SWITCHABLE WIDEBAND RECEIVER FRONTEND FOR 5G AND SATELLITE APPLICATIONS

Mfonobong Uko
2021

SWITCHABLE WIDEBAND RECEIVER FRONTEND FOR 5G AND SATELLITE APPLICATIONS

Mfonobong Uko

A THESIS SUBMITTED IN PARTIAL FULFILMENT
OF THE REQUIREMENT OF
MASTER OF SCIENCE BY RESEARCH
IN THE
MANCHESTER METROPOLITAN UNIVERSITY

Department of Engineering
Faculty of Science and Engineering
Manchester Metropolitan University
Chester St, Manchester, U.K.

2021

Declaration

I hereby declare that this thesis has been genuinely carried out by me and has not been used in any previous application for a degree. The invaluable participation of others has been duly acknowledged where appropriate.

Mfonobong Uko

Abstract

Modern day communication architectures provides the requirement for interconnected devices offering very high data rate (more than 10 Gbps), low latency, and support for multiple service integration across existing communication generations with wideband spectrum coverage. An integrated satellite and 5G architecture switchable receiver frontend is presented in this thesis, consisting of a single pole double throw (SPDT) switch and two low noise amplifiers (LNAs) spanning X-band and K/Ka-band frequencies. The independent X-band LNA (8-12 GHz) has a gain of 38 dB at a centre design frequency of 9.8 GHz, while the K/Ka-band (23-28 GHz) has a gain of 29 GHz at a centre design frequency of 25.4 GHz. Both LNAs are a three-stage cascaded design with separated gate and drain lines for each transistor stage.

The broadband high isolation single pole double throw (SPDT) switch based on a 0.15 µm gate length Indium Gallium Arsenide (InGaAs) pseudomorphic high electron transistor (pHEMT) is designed to operate at the frequency range of DC-50 GHz with less than 3 dB insertion loss and more than 40 dB isolation. The switch is designed to improve the overall stability of the system and the gain. A gain of about 25 dB is achieved at 9.8 GHz when the X-band arm is turned on and the K/Ka-band is turned off. A gain of about 23 dB is achieved at 25.4 GHz when the K/Ka-band arm is turned on and the X-band arm is off. This presented switchable receiver frontend is suitable for radar applications, 5G mobile applications, and future broadband receivers in the millimetre wave frequency range.

Key words: 5G communication, Wideband, Low Noise Amplifier(LNA), Satellite

Email: mfonobong.uko@stu.mmu.ac.uk

Acknowledgements

This research project is dedicated to the Almighty God for His great grace and unfailing love in my life. I am thankful Lord for the strength and capacity you gave me each day during this research journey.

I am thankful to my supervisors Dr. Sunday Ekpo, Prof Andy Gibson, Dr. Helen Ji, Dr. Ciaron Murphy, and Dr. Peter Aaen for their phenomenal encouragement and support during this research period. I owe big thanks to them and would really like to express my deepest appreciations here. I believe the skills, enthusiasm and earnest working attitude that I have learnt from them has helped propelled me throughout this research journey.

I would like to thank my parents, Prof & Mrs Charles Uko, brothers (Charlo and Uty), sisters (Ima and Pat) and Christina Adeyemi for their constant love, support, patience, and encouragement. They have been a pillar of strength. Special thanks goes to Daddy & Mummy Opute and the family for their love and parental care over here in the Uk. Thank you Daddy & Mummy Emeruwa for your constant spiritual support and prayers.

I am thankful to the entire Communication and Space Systems Engineering Research Team (CaSSE) members for their support and research collaboration.

I wish to thank my friends Anku & Kemi, Mayen D'Banga, Omle, Daniel, Esther, Gbemi, Mijana & Alexa, Mama Udee, Lotanna Ernest, Utibe & Mfonabasi Udofia, Mimi Grace, Bible Study friends for their moral support and for always being there. I am eternally grateful to members of the Deeper Life Bible Church for their love and care.

I would also like to thank Dr Sunday & Katie Ekpo specially for playing pivotal roles in my career path and showing me the right direction.

The list is endless. I appreciate everyone who has contributed in making this research journey a meaningful one.

Finally, I want to thank my sponsor the Niger Delta Development Commission (NDDC) for their sponsorship of my programme.

Contents

List of Figures

List of Tables

Acronyms

1G	First Generation
2G	Second Generation
3G	Third Generation
4G	Fourth Generation
5G	Fifth Generation
ADC	Analog-to-Digital Converter
ADS	Advanced Design System
BDMA	Beam Division Multiple Access
BER	Bit Error Ratio
CDMA	Code Division Multiple Access
DSP	Digital Signal Processing
FPGA	Field Programmable Gate Array
GPS	Global Positioning System
HARRF	Highly Adaptive Reconfigurable Receiver Frontend
HEMT	High Electron Mobility Transistor
InGaAs	Indium Gallium Arsenide
IoT	Internet of Things
LNA	Low Noise Amplifier
LO	Local Oscillator
LTE	Long Term Evolution
MMIC	Monolithic Microwave Integrated Circuit
NF	Noise Figure
PA	Power Amplifier
pHEMT	Pseudomorphic High Electron Mobility Transistor

RF	Radio Frequency
SPDT	Single Pole, Double Throw
SDR	Software Defined Radio
TDMA	Time Division Multiple Access
WCDMA	Wideband Code Division Multiple Access

Chapter 1

Introduction

1.1 Motivation

The rapid deployment of the fifth-generation (5G) wireless networks due to the increasing demand for high data has led to the development of high-performance communication systems to cater for wideband mm-wave frequency applications [1], [2], [3]. This development raises the need for multi-band/multi-standard communication network architectures/sub-systems for easy migration between existing mobile communication standards (1G, 2G, 3G and 4G) and current communication standards (5G and beyond) without changing their unique performance [4], [5], [6], [7], [8]. This thesis focuses on the development of a switchable wideband receiver frontend to achieve multi-band/multi-standard hardware sharing for 5G and satellite applications, offering the ability to change frequency band/hardware architecture without affecting the linearity of the circuit.

As 5G technology expand steadily towards the futuristic 6G technology era, network reuse becomes vital for the connectivity of over 30 billion anticipated devices [9], through the use of frequency adjustable networks and architectures utilising adaptable advanced RF circuits [10]. These architectures are mostly based on

tuning RF devices to create the switchable properties of the circuitry. These RF devices consist of multiple radios and antennas operating across various frequency bands for data transmission and reception. Furthermore, the requirement for wideband capabilities places a significant demand on the wireless spectrum for 5G coverage, and hence the need to exploit the higher frequencies of the millimetre-wave band as the microwave band below 10 GHz becomes saturated for wireless and mobile communication [11].

For a successful wideband, switchable receiver front-end design, key design parameters must be known. The frequency of operation must be specified according to the standards set by the spectrum overseeing authority. The size, cost of design and fabrication and overall power consumption of the receiver must be considered. These considerations are vital for the overall communication system sensitivity for signal detection and device applications. For this work, we explore the use of a single-pole, double throw RF switch to switch between two designed wideband low noise amplifier over 8-12 GHz range and 23-28 GHz frequency range.

1.2 Problem Statement

Designing a switchable receiver frontend design for 5G applications poses a variety of research challenges to radio system designers which includes:

- Component complexity: Building a 5G network is expensive and challenging as a result of the device-level changes required in terms of component design. A typical 5G communication device operating in millimetre wave frequency band must respond to the higher packing densities associated with wideband design.
- Coverage and transmission distance: 5G applications are designed using the millimetre-wave frequency band for its deployment to increase the com-

munication channel capacity and bandwidth. However, due to the short transmission range at this frequency range, novel infrastructures design and architectures are required to cater adequately to customers' coverage needs.

- Coexistence issues between existing communication network: This presents a design issue in mitigating interference, EM radiation and spectrum reuse.
- Security issues: Every data-driven technology is faced with the threat to the security and privacy of customers. Designed architectures will need to be secure in terms of signal integrity and customers personal details.
- Test and verification issues.

1.3 Research Aim and Objectives

This thesis presents a switchable wideband receiver frontend with reconfigurable capabilities between the X- (8-12 GHz) and K/Ka- (23-28 GHz) bands frequencies using the integration of an SPDT switch. This thesis addresses the following research questions:

- What RF/microwave communication performance metrics (including noise figure, amplifier gain, linearity, power consumption, noise floor, input and output reflections and isolation) are required for developing a switchable low noise amplifier for 5G applications operating in the X- (8-12 GHz) and K/Ka- (23-28 GHz) frequency bands?
- What circuit architecture and topology would be most appropriate for meeting the stringent requirements of a switchable wideband X- and K/Ka-bands receiver for satellite-cellular convergence applications?

1.3.1 Research Aim

This research aim is to design an integrated satellite and 5G switchable receiver frontend, consisting of a single pole double throw (SPDT) switch and two-low noise amplifiers (LNAs) spanning X-band (8-12 GHz) and K/Ka-band (23-28 GHz) frequencies respectively.

1.3.2 Research Objectives

To effectively accomplish this aim, the research objectives are:

- To investigate the existing circuit architectures and active device-level technologies for a receiver front-end subsystems development.
- To design, model, simulate and validate X- (8-12 GHz) and K/Ka- (23-28 GHz) bands MMIC LNAs for satellite-5G convergence applications.
- To design, model, simulate and validate a SPDT switch for a two-state dual-band MMIC LNA module application.
- To recommend the techniques for extending the design scope and achieving a reliable and robust reconfigurable RF transceiver.

This research is carried out in two parts:

- The first part is to design and implement two Low Noise Amplifiers (LNAs) for X and K/Ka-band applications and an SPDT switch using the WIN semiconductor process foundry.
- The second part is to integrate the SPDT switch with the designed LNAs for reconfigurable adaptation between the two frequency bands.

1.4 Design Specifications

Based on the above listed aim and objectives, the design goals for the switchable receiver is specified in Table 1.1 for the two low noise amplifiers.

Table 1.1: Transceiver Design Specifications for LNA

Parameter	Symbol	Unit	Min.	Typical	Max.	Condition
Frequency (X-Band)	f	GHz	8	.....	12	.....
Frequency (K-Band)	f	GHz	23	.....	28	.....
Transistors	.....	.....	.....	.....	.....	InGaAs pHEMT
Device Test Temperature	T^O	C^O	.....	16.85^O	.....	IEEE Standard
Simulation Temperature	T^O	C^O	.....	25^O	.....	IEEE Standard
Gain	S_{21}	dB	25	.....	35	.....
Gain Flatness	.....	dB	1	.....	2	.....
Noise Figure	NF	dB	0.5	.....	3	NFmin $<$ 2 dB
Input/output Impedance	Zin	Ohm	.....	50	.....	.....
Stability Factor	K	.....	2	$>$ 2	Infinity	Unconditionally Stable across all transistor range
Stability Factor	B1	.....	0	$>$ 0	Infinity	Unconditionally Stable across all transistor range
Power Consumption	P	W	.....	$<$ 0.14	.....	.....
Reflection Coefficient (Input and Output)	(S_{11}, S_{22})	dB	.....	$<$ -10	.....	Across the desired frequency range
Return Loss	S_{12}	dB	.....	$>$ 50	.....	Across the desired frequency range

These design goals are derived from industry-related standards in the communication industry.

1.5 Thesis Structure

This thesis is divided into five chapters. After the introduction, the chapters are focused on answering the research questions. The thesis is organised as follows:

Chapter 2 presents the design considerations for a wideband switchable low noise amplifier for 5G and Satellite application. It gives an overview of existing (state-of-the-art) LNAs operating at the target frequency bands (X and K/Ka). These considerations are compared to establish the research gaps for the requirements for satellite-integrated 5G networks consisting of various transistor technologies for switchable LNAs and SPDT switch.

Chapter 3 presents the design methodology for a highly adaptive reconfigurable receiver front-end (HARRF) LNAs to switch between X and K/Ka-band frequencies.

Chapter 4 presents the design results and analysis of the highly adaptive reconfigurable receiver front-end (HARRF) LNAs with the SPDT switch.

Chapter 5 summarises the theme and contribution of this thesis as well as the future work required for this design.

1.6 List of Journal Publications and Conferences

Peer-Reviewed Journal Papers

1. Muazzam Zafar, Sunday Ekpo, Jeena George, Paul Sheedy, **Mfonobong Uko**, and Andy Gibson, "Hybrid Power Divider and Combiner for Passive RFID Tag Wireless Energy Harvesting" *IEEE Access*, Vol 10, pp. 502-515, 2022.

2. **Mfonobong Uko** and Sunday Ekpo, "A 23-28 GHz pHEMT MMIC Low-Noise Amplifier for Satellite-Cellular Convergence Applications", *International Review of Aerospace Engineering (IREASE)*, Vol. 14, No. 5, 240—248, 2021.

3. **Mfonobong Uko** and Sunday Ekpo, "8-12 GHz pHEMT MMIC Low-Noise Amplifier for 5G and Fiber-Integrated Satellite Applications", *International Review of Aerospace Engineering (IREASE)*, Vol. 13, No. 3, 99—107, 2020.

Peer-Reviewed Conference Papers

1. Umm-E-Haya Ansari, Sunday Ekpo, **Mfonobong Charles Uko**, Arslan Altaf, Muazzam Zafar, Sunday Enahoro and Osmond Okpalugo, "5G enabled Mobile Operating Hospital and Emergency Care Service" *in Proc. 11th IEEE Wireless & Microwave Conference, Clearwater, Florida, USA*, pages 1–4, April 2021.

2. Jeena George, **Mfonobong Uko**, Sunday Ekpo, Muhammad Ijaz, Rupak Kharel, Qiuyu Wang and Helen Ji, "Design of a Multiband RF Slotted-Antenna for Biosensing Applications," *in Proc., 12th IEEE/IET International Symposium on Communication Systems, Networks and Digital Signal Processing Conference, Online (due to Covid-19)*, 20–22 July 2020.

3. Solomon Udeshi, **Mfonobong Uko**, Muazzam Zafar, Arslan Altaf, Bamidele Adebisi, Sunday Ekpo, "Integrated Space-enabled hybrid 5G-V2X Communications Link Modelling," *in Proc. International Communications Satellite Systems Conference, Okinawa, Japan*, 29 Oct.–01 Nov. 2019.

4. **Mfonobong Uko**, Muazzam Zafar, Arslan Altaf, Solomon Udeshi, Sunday Ekpo, Bamidele Adebisi, "K/Ka-Band Transceiver Sensitivity Modelling and Link Characterisation for Integrated 5G-LEO Communication

Applications," *in Proc. International Communications Satellite Systems Conference, Okinawa, Japan*, 29 Oct.–01 Nov. 2019.

5. **Mfonobong Uko**, Muazzam Zafar, Arslan Altaf, Solomon Udeshi, Sunday Ekpo, Bamidele Adebisi, "Link Budget Design for Integrated 5G-LEO Communication Applications," *in Proc. International Communications Satellite Systems Conference, Okinawa, Japan*, 29 Oct.–01 Nov. 2019.

6. Arslan Altaf, **Mfonobong Uko**, Sunday Enahoro, Muazzam Zafar and Sunday Ekpo, "Ka-Band Low-Noise Amplifier Design for Multiband 5G and Satellite Communications Applications," *IET Seminar on Active and Passive RF Devices, University of Cardiff, UK*, 22 May 2019.

7. Muazzam Zafar, Sunday Enahoro, **Mfonobong Uko**, Arslan Altaf and Sunday Ekpo, "Hybrid Power Divider-Combiner for Internet of Things Sensor Energy Harvesting Applications," *IET Seminar on Active and Passive RF Devices, University of Cardiff, UK*, 22 May 2019.

8. Sunday Ekpo, Rupak Kharel and **Mfonobong Uko**, "A Broadband LNA Design in Common-Source Configuration for Reconfigurable Multi-standards Multi-bands Communications," *in Proc., ARMMS RF & Microwave Society Conference, Double Tree by Hilton Oxford Belfry, Thame, UK*, 1–2 April 2018.

Chapters in the Books

1. **Mfonobong Uko**, Muazzam Zafar, Arslan Altaf, Solomon Udeshi, Sunday Ekpo, Bamidele Adebisi, "K/Ka-Band Transceiver Sensitivity Modelling and Link Characterisation for Integrated 5G-LEO Communication Applications," *in Proc. International Communications Satellite Systems Conference, Okinawa, Japan*, 29 Oct.–01 Nov. 2019.

2. **Mfonobong Uko**, Muazzam Zafar, Arslan Altaf, Solomon Udeshi, Sunday Ekpo, Bamidele Adebisi, "Link Budget Design for Integrated 5G-LEO Communication Applications," *in Proc. International Communications Satellite Systems Conference, Okinawa, Japan*, 29 Oct.–01 Nov. 2019.

Chapter 2

Design requirements and review of state-of-the-art wideband switchable LNAs topologies for 5G and satellite applications

5G Communication networks and standards are continually expanding with the millimetre-wave frequency band accommodating the deployment of the fifth-generation (5G), and beyond-5G wireless architectures [12]. These mm-wave 5G architectures make use of massive multiple-input multiple-output (Massive MIMO) and phased array to improve signal quality of the communication link by strengthening the desired signal and enhancing the interference rejection [13]. This has created a design challenge for RF frontend designers [3], [14] in terms of size, cost and power consumption [15]. To mitigate these challenges, intelligent radio architectures have become a vital requirement for multi-band/ multi-mode device designs for efficient utilization of the limited communication resources. These devices are designed with multiple communication standards to form the

RF transceiver system. The key receiver subsystem component of the transceiver is the low noise amplifier (LNA) [3], [16] while the key transmitter subsystem component is the power amplifier (PA). Other components include filters, duplexers, and RF switches found in both the receiver and transmitter. Figure 2.1 shows an illustration of a typical RF transceiver system.

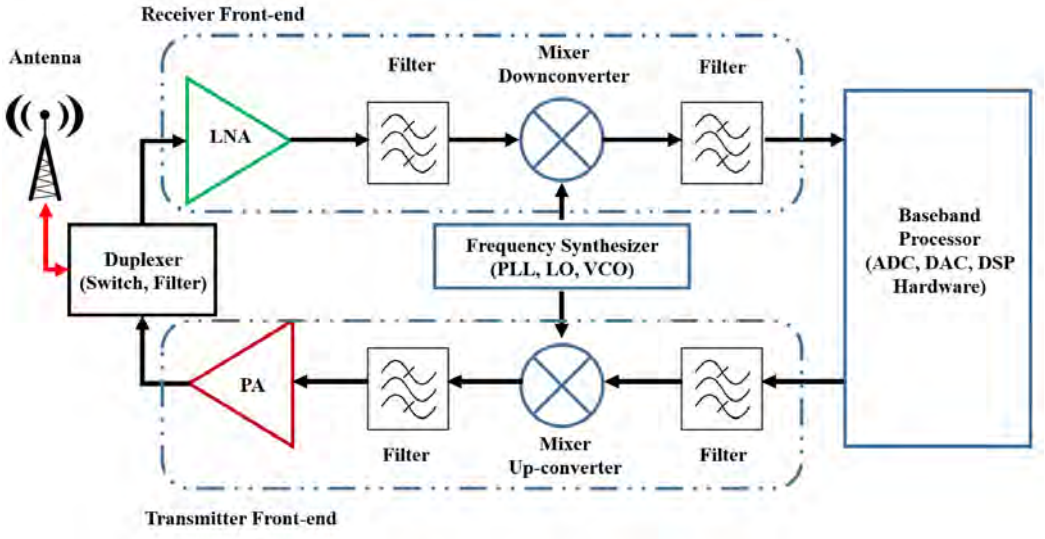

Figure 2.1: Simplified RF Transceiver

2.1 5G Communication Evolution

As customers demand for higher data rate/performance, more device functionality, secure transmission, longer battery life, and smaller size devices [10], [18] keeps growing exponentially, mobile data traffic is projected to exceed 70 exabytes per month in 2023 [9] (over 100x increase since 2010), leading to the need for spectrum efficient and reliable communication systems to be designed [19]. The overall communication system design must be efficient in addressing growing/extending worldwide media transmission and growth in data traffic through the deployment of hybrid 5G networks to support higher spectral and energy efficiencies for the growing global usage of 5G smartphones and internet-of-things

(IoT) devices [2]. These growing media services include a wide range of vertical industries such as automotive, health, energy and other industries [20] leading to the multimode requirements of integrating the lower generations (1G, 2G, 3G and 4G) with 5G communication systems for the receiver and transmitter RF front end design [21]. This means the RF front ends have to handle multiple standards and multi modes in one device, with functionality specific to particular services or customers over a shared network infrastructure. Figure 2.2 shows the growth of mobile communication network and the increasing complexity across various communication generations, service provide and their limitations.

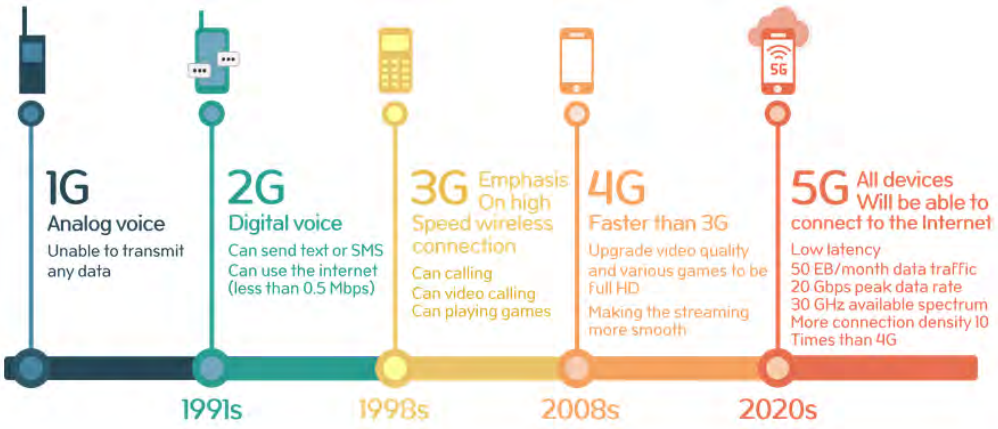

Figure 2.2: Growth of Mobile Generations. (Source: 5glearning.org)

Table 2.1 shows a comparison between the various generations of communication standards.

2.2 Multi-band/Multimode Requirement

The multimode requirements of integrating the existing communication systems with 5G communication systems forms the research gap this thesis addresses for the challenges faced in the receiver frontend design. This provides the RF receiver frontend the capability to handle multiple standards and multi modes in

Table 2.1: Comparison of the various Mobile Generations

Generation	Deployment	Speed	Technology	Services	Core Network	Limitations
2G	1991	64 kbps	CDMA, TDMA	GSM, Digital Voice	PSTN	lower transfer rate, low efficiency for packet switched services
3G	2004	2 Mbps	CDMA, WCDMA	Internet-enabled Mobile services, High Quality Video	PSTN	limited data rate
4G	2010	1 Gbps	CDMA, OFDM	All-IP Wearable devices	Internet	Power consumption
5G	2020 and beyond	100 Gbps	CDMA, BDMA	IoT-enabled devices	Internet	Coverage

one device. A simple approach to realise the multi-band/multimode integration is to implement several radio circuits in parallel, but this leads to a bulky device in terms of size; hence a switchable architecture with multiple radio circuits must be designed to implement the multi-band/multimode requirements [2], [22], [23]. Many communication devices have been developed to function in multi-mode and multi-band [24], [25], [26], [22]. These devices will need circuitries adapted to suit the evolving communication standards without much increase in the circuitry size. Implementing these circuits will be difficult as the number of supported wireless systems and frequency bands increases. Therefore the realisation of switchable wideband circuits, which can optimally support current and emerging wireless communication standards with a small adaptive circuitry, is inevitable.

2.3 Software-Defined Radio

The invention of software defined radios (SDR) [27],[28], brought about changes in the hardware circuitry of devices, through incorporating programmable software stage implemented in a field programmable gate array (FPGA) [29], [30]. It offers

the advantage of switching between frequencies through software-programmable hardware, where functional changes are automatically made by updating the software algorithm to suit the network environment. This offers a wide range of frequency functionalities, accommodating existing communication standards with new and emerging standard.

As communication standards evolve, integration of multi communication networks on the receiver frontend requires adaptive architectures and constituent circuits to suit distinctive operation frequencies, signal bandwidth, and power prerequisites, which must be satisfied by innovative programming characterised by advanced software-defined radio techniques [31], [30]. Gonzalez-Rodriguez et al[32] proposed the integration of a broadband signal processor with high-performance tunable RF components to satisfy the requirements for switchable low noise frontend for different environments and user needs. This brought a considerable reduction in the size and hardware complexity of the device with low energy consumption. Gielen and Goris [33] showed that reconfigurable software-defined radios were needed to cope with the power requirements of the fourth generation systems, a digital solution for high data rates and seamless RF transmission.

2.4 Active Semi-Conductor Materials

Specific RF design approaches require a manufacturer's semiconductor foundry (transistor technology process) for implementation. Several transistor technologies like the Silicon-Germanium hetero-junction bipolar transistors (SiGe HBT), Indium phosphide pseudomorphic High Electron Mobility Transistor (InP pHEMT), Gallium Arsenide Pseudomorphic High Electron Mobility Transistor (GaAs pHEMT), Gallium Nitride High Electron Mobility Transistor (GaN HEMT) and complementary metal-oxide-semiconductor (CMOS) have been extensively investigated

and characterised around the world. CMOS transistor show greater scalability and higher cut-off frequency up to and over 200 GHz than the rest, but HEMTs have attracted attention due to their high-power performance. Popular 5G foundry processes currently include the GaAs pHEMT process and the GaN HEMT process. GaN has emerged as the leading semiconductor material for high-power microwave switches and amplifiers, although GaAs are still the material choice for low noise. GaAs amplifiers tend to be more linear, with less distortion, than GaN amplifiers, although GaN devices have been used with digital predistortion (DPD) to achieve enhanced linearity at higher frequencies [34].

Active semiconductor devices for 5G applications must positively withstand the heat generation due to multiple-input and multiple-output data processing. In 4G cell phones, the 2.61 GHz frequencies are well handled in complementary metal-oxide-semiconductor (CMOS). For 5G devices, frequencies span above 3.8 GHz up to 100 GHz. These frequencies require semi-conductor materials for their components fabrication as switching devices must be able to optimally switch from one radio access technology to another without compromising the integrity of the transmitted data, at minimal heat consumption. GaN and GaAs semiconductor materials are best for switchable devices microwave and mm-wave frequencies due to their high mobility, high current density, high operating temperature, and current density [35], [36], [37]. Considering the significant requirements for 5G systems (smaller size and lower power consumption), high electron mobility transistors (HEMT) using GaN (GaN HEMT) offers wide bandgap properties [34].

Figure 2.3 shows the functionalities of various active semiconductor materials.

Table 2.2 shows the cut-off frequency (f_t) versus the frequency of oscillation (f_{max}) for various transistor technologies.

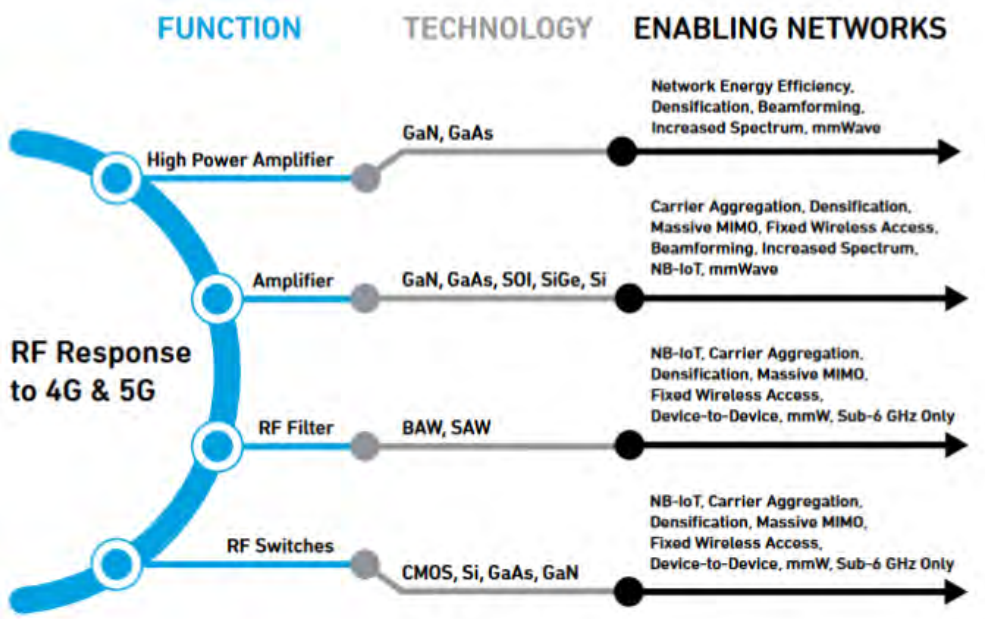

Figure 2.3: Active Semiconductor and their Enabling Networks (Source: Qorvo.com)

Table 2.2: (f_t) vs (f_{max}) for various transistor technologies

Process Technology	Minimum size (µm)	(f_t) GHz	(f_{max}) GHz
SiGe HBT	0.5	130	160
GaAs HBT	0.8	180	280
InP HBT	1.0	228	270
GaAs MESFET	0.2	80	120
GaAs pHEMT	0.12	120	200
InP HEMT	0.12	250	350
GaAs mHEMT	0.12	225	250

2.5 Frequency Band Specification

For 5G frequency bands, the mm-wave frequency band is chosen to satisfy the unquenchable demand for high data rate, speed and bandwidth by consumers. As a result, millimetre-wave satellite hardware development for space and terrestrial 5G communications is inevitable for seamless transmission of data and complementing existing terrestrial networks to deliver coverage to hard-to-reach areas.

The third-generation partnership project (3GPP) specifies two basic frequency ranges (FR) for 5G communication applications. Since cm-/mm-wave spectrum exhibit different behaviours in nature, the radio frequency (RF) specifications requirements for FR1 and FR2 are defined separately in many cases (Table 2.3).

Table 2.3: 5G SPECIFICATIONS FREQUENCY

Frequency Range	Range covered in Rel. 15 (MHz)
FR1	450 - 6000
FR2	24250 - 52600

The millimetre-wave frequency band is the focused band for 5G and beyond-5G communication network offering the required wideband spectrum for high data rates, device density, and network capacity for fifth-generation (5G) and beyond-5G wireless networks [38]. 5G mm-wave deployment in the millimetre-wave region is very fractal due to its unpredictable behaviour above 20 GHz. The deployment is easier given a line-of-sight scenario but highly unstable for non-line of sight. Deployment of phased arrays partially deals with this limitation, hence the need for a robust wideband and efficient low noise amplifier design, sensitive enough to detect and amplify the attenuated signal received to reduce the path loss in the propagation path.

For the purpose of analysing the 5G receiver sensitivity in this thesis, the NR channel bandwidth for FR2 (Table 2.4) will be utilised. The key advanced radio access technology (RAT) implementation considerations for the 5G NR FR2 are higher complexity in device development, measurement challenges, and new testing approaches. The mm-wave considerations include high bandwidth for high data rate, minimal high contiguous bandwidth at lower frequencies; high free-space path loss at high frequencies; and line-of-sight requirements.

The sub-carriers spacings (SCSs) are 60 kHz and 120 kHz for all the channel bandwidths except the 400 MHz channel (which supports only the 120 SCS).

Table 2.4: NR Channel Bandwidth for FR2

NR Band	SCS (KHz)	Channel Bandwidth (MHz)			
		50	100	200	400
n257	60	Yes	Yes	Yes	
	120	Yes	Yes	Yes	Yes
n258	60	Yes	Yes	Yes	
	120	Yes	Yes	Yes	Yes
n260	60	Yes	Yes	Yes	
	120	Yes	Yes	Yes	Yes
n261	60	Yes	Yes	Yes	
	120	Yes	Yes	Yes	Yes

The reported MMIC LNA is designed to cover the proposed new NR bands in FR2 (Table 2.5).

Table 2.5: New NR Bands in FR2

Band Number	Uplink (GHz)	Downlink (GHz)	Bandwidth (MHz)	Duplex Mode
n257	26.5 - 29.5	26.5 - 29.5	3000	TDD
n258	24.25 - 27.58	24.25 - 27.58	3250	TDD
n260	37 - 40	37 - 40	3000	TDD
n261	27.5 - 28.35	27.5 - 28.35	850	TDD

Three key frequency bands are used for 5G in Europe: Lower frequency band at 700MHz, 3.4-3.8 GHz for wider bandwidth application and 24.25-27.5 GHz, known as the "Pioneer" Band for high capacity networks. Table 2.6 shows the three important 5G frequency classification and their applications in radio access technology advancement.

Table 2.6: 5G frequency classification and applications

Frequency Band	Band Classification	Application Deployment
450 MHz - 6 GHz	Sub-6 GHz	64 kbps
28/37/39 GHz	mmWave	2 Mbps
57-71 GHz	mmWave	1 Gbps

The 5G standards cover a variety of applications, including Enhancement of Ultra-Reliable (UR) Low Latency Communications (URLLC), Multimedia Priority Service, Vehicle-to-everything (V2X) application layer services, 5G satellite access, Local Area Network support in 5G, wireless and wireline convergence for 5G.

2.6 Multi-standards Compatibility

5G communication system integration with previous generations (1G, 2G, 3G, and 4G) is vital in a wideband receiver RF frontend design. The authors in [18] have suggested that 5G systems exploit architectures that enables device-to-device (D2D) connectivity at the mobile end as compared to the 2G-4G networks, which functions at the infrastructure end [19].

The authors in [39] proposed a reconfigurable architecture that dynamically changes mission-specific hardware accelerators to provide onboard processing for in-flight adaptation during space exploration missions. This allows for the adjustment of the system to meet mission-specific objectives of space exploration. For multi-standard capabilities of the system antenna, [40] demonstrated that by maximising each of the frequency reconfiguration, spatial and polarisation diversity, there is a performance gain to the communication system capacity.

2.7 Data Rate and Seamless Connectivity

More than 70% of the worldwide populace will have a portable network by 2023. The absolute number of worldwide versatile endorsers will grow from 5.1 billion (66 per cent of the populace) in 2018 to 5.7 billion (71 per cent of the populace) by 2023 [9]. 5G gadgets will be more than 10% of worldwide cell phones by 2023.

By 2023, worldwide cell phones will develop from 8.8 billion out of 2018 to 13.1 billion by 2023 (1.4 billion of those will be 5G enabled) [9]. 5G mobile networks provides higher than 10 Gb/s peak data rate in uplink and downlink alongside sub-1ms latency which caters for the required data rate and connectivity.

Table 2.7 shows the download, upload rate and device connection density of different technology generations.

Table 2.7: Download, Upload and Connection density for 2G, 3G, 4G, 5G and 6G devices

Description	2G	3G	4G	5G	6G
Average download speed	50 kbps	8 Mbps	100 Mbps	300 Mbps	1 Gbps
Average upload speed	50 kbps	2 Mbps	50 Mbps	100 Mbps	1 Gbps
Connection density $/km^2$	N/a	N/a	10^5	10^6	10^7
Latency	600 ms	120 ms	30 ms	10 ms	1 ms

For seamless connectivity, 5G incorporates multiple antenna elements design and digital/hybrid beamforming techniques to boost receiver sensitivity and overall data transmission connectivity especially for those in remote and rural areas[41],[17], when deployed alongside satellite [19], [42]. Table 2.8 shows the distance of satellites from the earth ground station. The satellite network extends coverage for both space and terrestrial applications [43]. The satellite network integration with 5G services is established as a non-standalone system for throughput increase, large coverage area, and service reliability. The LEO network provides a faster transmission rate because of its short distance, while the GEO network provides wider coverage.

Table 2.8: Satellite Distance from Earth Ground Station

Satellite Network	Distance from Ground Station
LEO	500 km - 2,000 km
MEO	19,000 km - 24,000 km
GEO	35,786 km

2.8 Power Consumption

Power consumption is one of the design challenges 5G frontend device developers face. The authors in [44] estimates the power consumption of a 10 Gb/s 5G receiver to be above 3W, with the baseband processor consuming more than 2W. This high power consumption (a vital performance matrix for 5G) severely affects the battery life of 5G mobile applications. The authors in [44] have proposed reducing the high power consumption through minimising the Forward Error Correction coding complexity of the system architecture of the 5G applications alongside the provision of Carrier Aggregation for increased bandwidth. Rostami et.al. [45] have proposed a pre-grant message (PGM) signalling approach to reduce the energy consumption of the cellular subsystem in the downlink.

2.9 Size and Robustness

The designed switchable wideband receiver must be robust and smaller in size when compared with the traditional single-ended receivers.

2.10 Modulation Scheme

Designing the switchable wideband receiver requires an understanding of modulation methods and radio techniques. Gaussian Minimum Shift Keying (GMSK),

Phase-shift keying (PSK) were popular 2G and 3G modulation schemes, while Amplitude Phase Shift Keying (APSK) and Orthogonal frequency division multiplexing (OFDM) has been adopted in fourth-generation (4G) networks. For 5G devices, new modulation schemes with high spectral efficient hybrid schemes like frequency shift keying quadrature amplitude modulation (FSK-QAM) [46], [47] are needed for efficient spectral modulations in millimetre-wave bands for high capacity transmissions [48], [49], [50].

2.11 Broadband MMIC Low Noise Amplifier Design

This thesis presents two LNAs designed based on an inductive source-degenerated cascade architecture biased for low power consumption. The active device makes use of a scalable PL15-10 0.15 µm low noise InGaAs pseudomorphic high electron mobility transistor process technology provided by WIN Semiconductors. The most critical part of the amplifier design is the input matching network, where the 50 Ω input termination is converted into a complex impedance close as possible to the optimum noise match of the transistors. A cascaded system is employed to achieve an appreciably high gain, very low noise performance, and negligible reflections at the input and output. This requires system tuning and optimisation to achieve the design goals for the LNA.

2.11.1 Transistor Selection

Transistor selection is a vital step in designing an MMIC LNA as it determines the performance metrics of the LNA, such as its noise property. The process technology used for this research work is the WIN PL15-12 0.15 µm InGaAs pHEMT from WIN Semiconductors owing to its low noise and low power 4performance.

The active device models available from the process includes co-planar waveguide (CPW) pHEMTS from 2x10 µm to 8x150 µm as well as two transistors types, namely Mesa and Thin-Film Resistor (TFR). A schematic cross-section of the pHEMT is shown below:

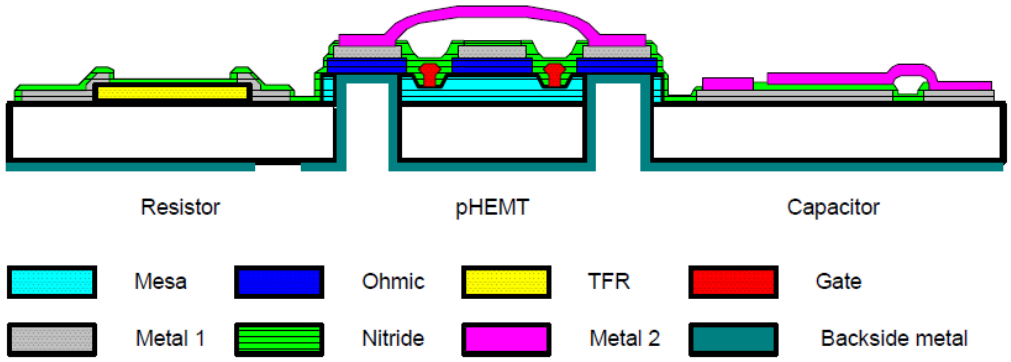

Figure 2.4: Cross section of 0.15 µm InGaAs pHEMT (Source: www.winfoundry.com)

2.11.2 Two-Port Network

High-frequency designs (including LNAs) are best described through the use of a two-port network design. A two-port network illustrates the interrelationship between the input port voltage, V_1 and current, i_1 with the output port voltage, V_2 and current, i_2. At low frequencies, this two-port network (Fig. 2.5) is easily

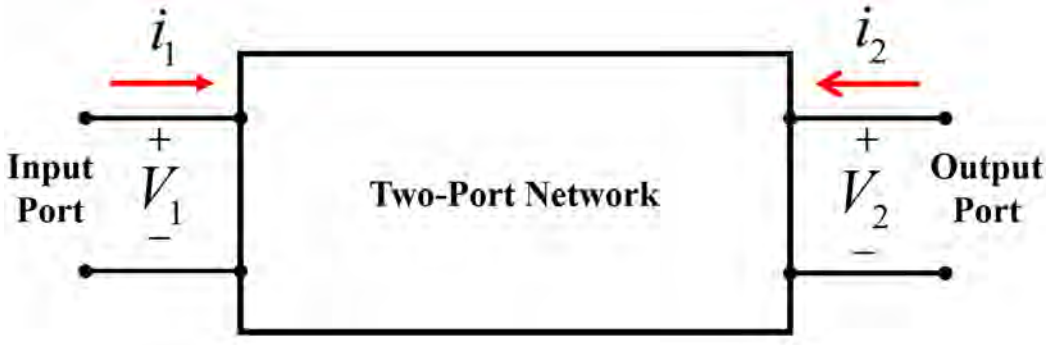

Figure 2.5: Two-Port Network Design

characterised through its admittance (Y-parameters), impedance (Z-parameters), and hybrid (H-parameters) by applying a test voltage or current at the input port while maintaining the output port as an open or short circuit.

At high frequencies (RF and Microwave), the use of voltage and current in the network becomes increasingly difficult to implement for the AC signals [3]. Hence another characterisation design network called the Scattering Parameters (S-Parameters) is used. This design is defined based on power transmitted and reflected in the network, usually measured with the device inserted between a 50 Ω load and source (Fig. 2.6). For simulation purpose, the maximum power handling capability of a two-port network is at 30 Ω while the lowest attenuation is at 77 Ω making the ideal characteristic impedance of 50 Ω a compromise between these values.

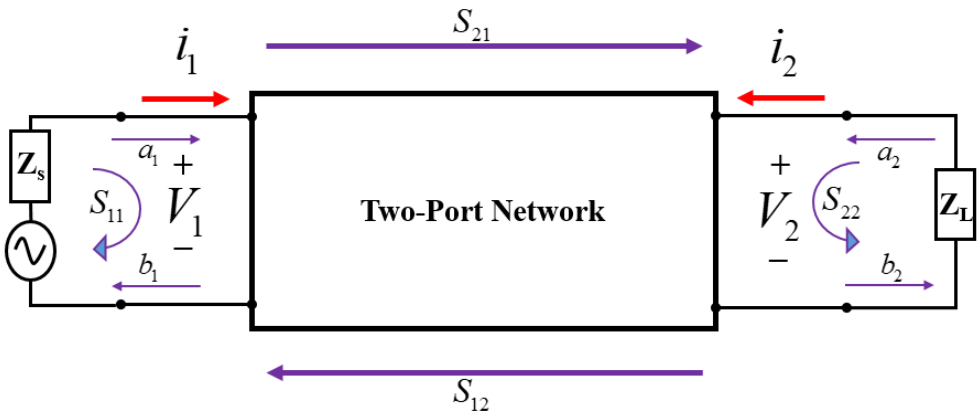

Figure 2.6: S-Parameter representation of Two-Port Network Design

The S-Parameter matrix is given as:

$$\begin{bmatrix} b_1 \\ b_2 \end{bmatrix} = \begin{bmatrix} S_{11} & S_{12} \\ S_{21} & S_{22} \end{bmatrix} \begin{bmatrix} a_1 \\ a_2 \end{bmatrix} \tag{2.1}$$

where:

S_{11} = Input reflection coefficient

S_{22} = Output reflection coefficient

S_{12} = Reverse transmission coefficient

S_{21} = Forward transmission coefficient

These scattering parameters can be resolved into admittance (Y-parameters), impedance (Z-parameters) and hybrid (H-parameters).

2.11.3 LNA Topologies

The choice of a process technology alongside transistor geometry is vital for wide-band switchable receiver frontend characterisation in terms of the noise figure performance. Three distinct LNA topologies are popular in terms of design and performance optimisation [51]. These include: Common-source(CS), common-gate (CG), and cascode LNA topologies. The table below (Table 2.9) shows a comparison of the three topologies [51]. The CS topology gives high gain and

Table 2.9: Comparison of Three LNA Topologies

Characteristic	Common-Source (CS)	Common-Gate (CG)	Cascode
Noise Figure	Lowest	Rises rapidly with frequency	Slightly higher than CS
Gain	Moderate	Lowest	Highest
Linearity	Moderate	High	Potentially Highest
Bandwidth	Narrow	Fairly broad	Broad
Stability	Often requires compensation	Higher	Higher
Reverse Isolation	Low	High	High
Sensitivity to Process Variation	Greater	Lesser	Lesser

good noise performance while the CG topology gives a lower power consumption rate. At high frequency, the common-source topology improves the stability and linearity of the amplifier, giving an excellent input impedance match with the lowest possible noise figure at the expense of the gain. The common-gate

topology also improves the stability of the amplifier and its linearity at the expense of gain. The cascode topology improves stability, linearity and gain flatness [52]. However the Cascode topology degrades noise and gain performance due to increased substrate parasitics at higher frequencies. The CS topology with an inductive feedback is adopted in the design for this thesis.

2.11.4 Noise Characterization

Noise is an essential figure-of-merit in microwave design defined as an undesired signal added by system components that degrades the performance of transmitted signals. Three primary sources of noise in a semiconductor device are thermal noise, shot noise and flicker noise. Noise is best characterised using its noise factor, F, which is defined as the ratio of the signal-to-noise power ratio at the input to the signal-to-noise power ratio at the output, when the input is a standard noise source ($T_o = 290K$). The noise power at the input is defined as $N_i = kT_oB$, where k is the boltzmann's constant = -198.6dBm/K/Hz and B= bandwidth in Hz.

$$F = \frac{S_i/N_i}{S_o/N_o} = \frac{SNR_i}{SNR_o} \tag{2.2}$$

For satellite systems (5G inclusive), the noise factor is determined using the performance matrices of the low noise amplifier, mixers, and oscillators at the receiver's front-end. For a linear system, the noise factor can further be expressed as:

$$F = \frac{P_{N_o}}{P_{N_i}G_A} \tag{2.3}$$

Where P_{N_o} is the total available noise power at the output of the amplifier, P_{N_i} is the total available noise power at the input of the amplifier and G_A is the available power gain. Considering the noise temperature in the satellite, the author in [43] defined the noise temperature in relation to the standard noise source as:

$$T_e = T_o(F - 1) = 290(F - 1) \tag{2.4}$$

For the multistage amplifier system, the overall noise factor is expressed in terms of the noise factors (F_1, F_2, F_3, F_n) and gains ($G_{A1}, G_{A2}, G_{A(n-1)}$) of the individual "n" stages respectively as:

$$F = F_1 + \frac{F_2 - 1}{G_{A1}} + \frac{F_3 - 1}{G_{A1}G_{A2}} + ... + \frac{F_n - 1}{G_{A1}G_{A2}...G_{A(n-1)}} \tag{2.5}$$

Mathematically, the noise figure NF in dB is expressed as:

$$NF = 10log(F) \tag{2.6}$$

For K/Ka-band satellite applications, the noise figure is critical in determining the overall system sensitivity; hence the LNA should offer the low-noise capability for effective performance. The noise equation in (2.5) shows that the noise performance of the first stage dominates the overall noise performance of the LNA. Therefore, the best noise matching is applied at the input.

2.11.5 LNA Stability

The stability of the LNA is a critical design consideration needed to prevent amplifier oscillation due to the gain fluctuations within the LNA. Rollete's stability equations are used to determine the stability of the LNA:

$$K = \frac{[1 - |S_{11}|^2 - |S_{22}|^2 + |\Delta|]}{2|S_{12}S_{21}|} > 1 \tag{2.7}$$

$$\Delta = S_{11}S_{22} - S_{12}S_{21} \tag{2.8}$$

When these two conditions are simultaneously satisfied, the LNA will be unconditionally stable.

The designed LNAs (X-Band and K/Ka-Band) are both three-stage LNAs using the common-source topology. This topology is chosen to minimise the noise figures of the LNAs. Each stage is designed separately in a systematic approach taking into consideration industry-based standards and procedures. The designs are both developed using Advance Design Software (ADS).

2.12 Switchable Receiver Frontend Architectures

Switchable receiver frontend architectures are needed to meet different operational and emergent communication standards and specifications for the receiver. The switchable frontend network provides matching at different frequencies, and the output network forms a tunable bandpass filter (BPF) for band selection. However, the input tuning network used to match the source impedance does not provide adequate filtering of the unwanted out-of-band signals. To address this unwanted signals in the receiver front-end, [53] presented a single-ended to differential conversion (S2DC) architecture (Fig. 2.7b) to attenuate out-of-band blockers at the input stage. This topology also improved the linearity of the LNA without degrading its noise performance. For simple and cost-effective production of a large number of LNAs, the use of monolithic microwave integrated circuits (MMIC) is best adopted.

f_1 and f_2 are the frequencies of two out-of-band blockers interfering with the wanted signal while f_0 is the load resonant frequency in Fig. 2.7a and the centre frequency of the input BPF in Fig. 2.7b. As shown in Fig. 2.7, the interferer signal generated due to the third-order inter-modulation of the out-of-band blockers is smaller in the single-ended to differential conversion (S2DC) architecture compared to the conventional architecture [53].

The use of switches has been the popular design approach by RF engineers to achieve multiple frequency outputs. A key disadvantage to this approach is the bulky nature of the designed chip, which becomes unacceptable for mm-wave phased arrays that require a tiny element spacing [17]. The alternative approach is to design a single RF front-end employing tunable elements and switches inside matching networks to change the frequency band of operation [11]. This method has been extensively investigated and implemented at sub-6-GHz frequencies. Ulusoy et al [54][55] showed a successful integration of shunt capacitive RF-MEMS

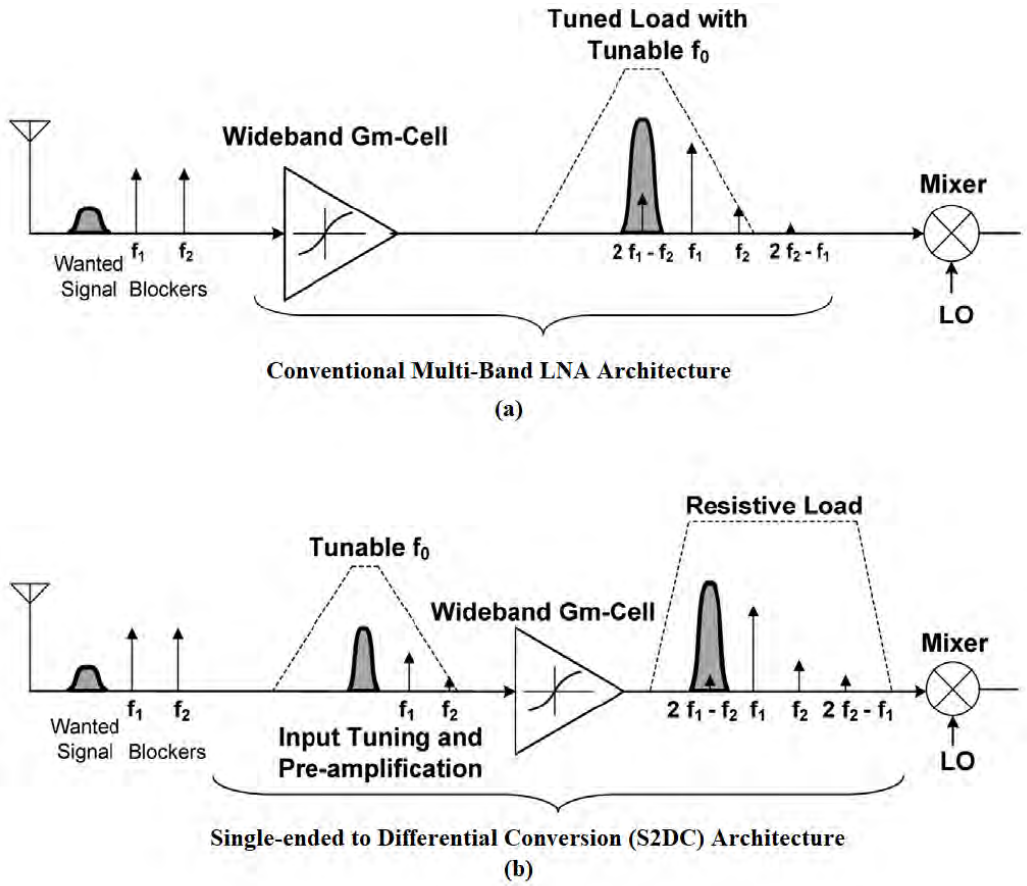

Figure 2.7: (a) Conventional Multi-band Receiver Architecture, (b) Single-ended to Differential Conversion (S2DC) Architecture.

switches with the SiGe BiCMOS process for reconfiguration in the millimetre-wave range (24 to 74 GHz frequency band). In [56], an inductorless, wideband, digitally reconfigurable LNA for multi-standard radio receivers is presented. The LNA employs a current-reuse technique to achieve both high gain and low power consumption.

Table 2.10 shows some switchable low noise amplifiers with their design architectures.

Table 2.10: Switchable Low Noise Amplifiers and their design architectures

Reference	Frequency	Technology	Switchable Topology
[57]	2 - 5 GHz	0.18um CMOS	Component sharing, Q-aware IM
[58]	28/60 GHz	0.13um SiGe BiCMOS	Switch, LC Tank IMN, Tunable stubs
[59]	125 - 143 GHz	0.13um SiGe BiCMOS	Single RF-MEMS Switch
[60]	1.6 - 2.2 GHz	CMOS	Tunable duplexer
[61]	3 - 5 GHz	0.13um CMOS	RF Switch
[55]	24 - 79 GHz	0.25um SiGe BiCMOS	Shunt Capacitive RF-MEMS switches

2.13 Satellite-5G Cellular Convergence Network

The role communication satellites play today, from 'connecting the unconnected' to providing secure and seamless device-to-device communications, cannot be overemphasised. Space communication architectures play a vital role in the 5G ecosystem [62], taking advantage of 5G wider coverage, higher throughput, and lower latency [63] [64] while incorporating existing 3G and 4G technologies to provide faster connections [8] [65]. 5G communication networks are designed for anybody, any-place, whenever and this is the aspect use of satellite [66] complements the terrestrial infrastructure for a satellite-5G cellular convergence network.

With the evolution of 5G standard(s), satellite networks incorporation into the emerging 5G ecosystem offers the ability to meet the needs of horizontal and vertical applications (Fig. 2.8) and deliver high mobile broadband and reliable transmission of high-speed data. This integration requires a critical analysis of the satellite link performance [67], taking into consideration large-capacity communication, the noise level, power level and sensitivity of the overall satellite system, in order to cope with various communication demands of space and ter-

restrial applications [68] [69] [70].

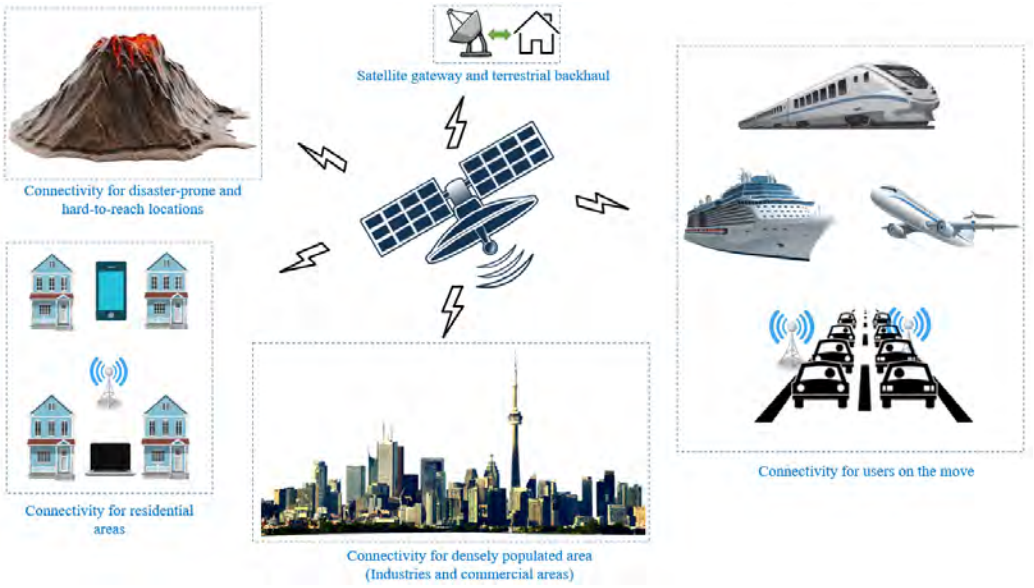

Figure 2.8: Satellite-5G Cellular Convergence Network

The Satellite-5G Cellular Convergence Network also involves real-time and non-real-time data transmission, ensuring ubiquitous seamless continuity for telecommunication operations. Furthermore, integrating satellite with 5G involves multi-protocol communication and pan-cloud computing (including industrial IoTs, big data, artificial intelligence and 5G) integration for advanced radio connectivity through switchable multi-band low noise performance, long-haul remote coverage; system security; and critical and non-critical remote manufacturing plant resources monitoring. Satellite-5G Cellular Convergence Network back-haul for big data analytics, ultra-reliable low-latency connectivity and massive scale computing nodes creates a safer, intelligent and more efficient communication system for the edge, gateway and enterprise nodes within the industry 4.0 hierarchy [67].

For this research, a study of literatures give some state-of-the-art low noise amplifiers designed for X-band (Table 2.11) and K/Ka-band (Table 2.12) to capture satellite-5G cellular integration.

Table 2.11: State-of-the-art LNAs operating at the target X frequency band

Ref.	Process	Application	Freq.(GHz)	Gain (dB)	Noise (dB)	Power (mW)
[71]	0.7 µm GaAs mHEMT	SATCOM	7-11	30	1	62.2
[72]	0.65 µm CMOS	SATCOM	9.35-10.65	27.8	1.8	4.68
[73]	0.13 µm SiGe BiCMOS	SATCOM	6-12	21	1.7	100
[74]	0.65 µm CMOS	SATCOM	8-12	15	8.4	110
[75]	0.18 µm CMOS	SATCOM	6.4-7.4	12.5	3	19
[76]	0.1 µm GaAs mHEMT	SATCOM	4-12	31.5	1.31	8
[77]	0.1 µm InP HEMT	SATCOM	0.3-14	40	2.73	12

2.14 Link Budget analysis for Satellite-5G Cellular Convergence Network

Satellite-5G Cellular Convergence Network requires a critical analysis of the application link performance [13], [67]. A Link Budget design and analysis determines component (system and subsystem) parameters and the signal power at the receiver front-end needed to recover the information transmitted. This analysis takes into consideration the uplink and downlink frequencies (Table 2.13), for seamless transmission of information with less interference (Fig. 2.9). A radio

Table 2.12: State-of-the-art LNAs operating at the target K/Ka frequency band

Ref.	Process	Application	Freq.(GHz)	Gain (dB)	Noise (dB)	Power (mW)
[78]	0.4 µm CMOS SOI	SATCOM	20-22	3-17	8	2.82
[79]	0.25 µm SiGe	SATCOM	19.7-21	0	5	0.24
[80]	0.4 µm CMOS	5G	26.5-29.5	0	4.2	0.9
[81]	0.28 µm CMOS	5G	25.8-28	30-69	6.7	0.4
[82]	0.13 µm SiGe	5G	27.5-29	30	3.7	3.3
[83]	0.65 µm CMOS	SATCOM	17-21	-16-34	5.4	0.93
[84]	0.15 µm AlGaAs-InGaAs pHEMT	5G	26-33	22.8	1.6	-
[76]	0.1 µm GaAs mHEMT	5G	25-34	24.2	3.04	2.8
[77]	0.1 µm InP HEMT	SATCOM/5G	16-28	32.3	4.11	3.5
[52]	GaAs pHEMT	SATCOM	18-21.6	30.3	1	60
[85]	0.1 µm GaAs pHEMT	SATCOM/5G	18-43	21.6	1.8-2.7	140
[86]	0.25 µm SiGe	5G	24-34	26.4	3.1-3.5	134
[87]	0.4 µm CMOS	5G	26-33	27.1	3.3-4.3	31.4

Table 2.13: K/Ka-Band Satellite Link Budget Allocation

Transmit Parameter	Frequency	Bandwidth
Uplink	27.5 - 31 GHz	3.5 GHz
Downlink	17.7 - 21.2 GHz	3.5 GHz

link budget based on theoretical assumption is presented in Table 2.14 showing system design parameters and requirement for the 5G-LEO K/Ka-band Satellite link.

Table 2.14: 5G-LEO LINK BUDGET ANALYSIS

Parameter	Value	Unit	Reference
Bandwidth B	3.5	GHz	[88]
SNR_{min}	10	dB	[88]
Transmit EIRP	40 to 63	dBm	[88]
Thermal Noise Power	-125	dBm	[88]
Receiver (Rx) Noise Figure	6	dB	[88]
Transmitted Power P_t	17 to 40	dBm	[88]
Transmitter (Tx) Gain G_t	20	dBi	[88]
Receiver (Rx) Gain G_r	20	dBi	[88]
Path Loss (L_p)	4		[88]

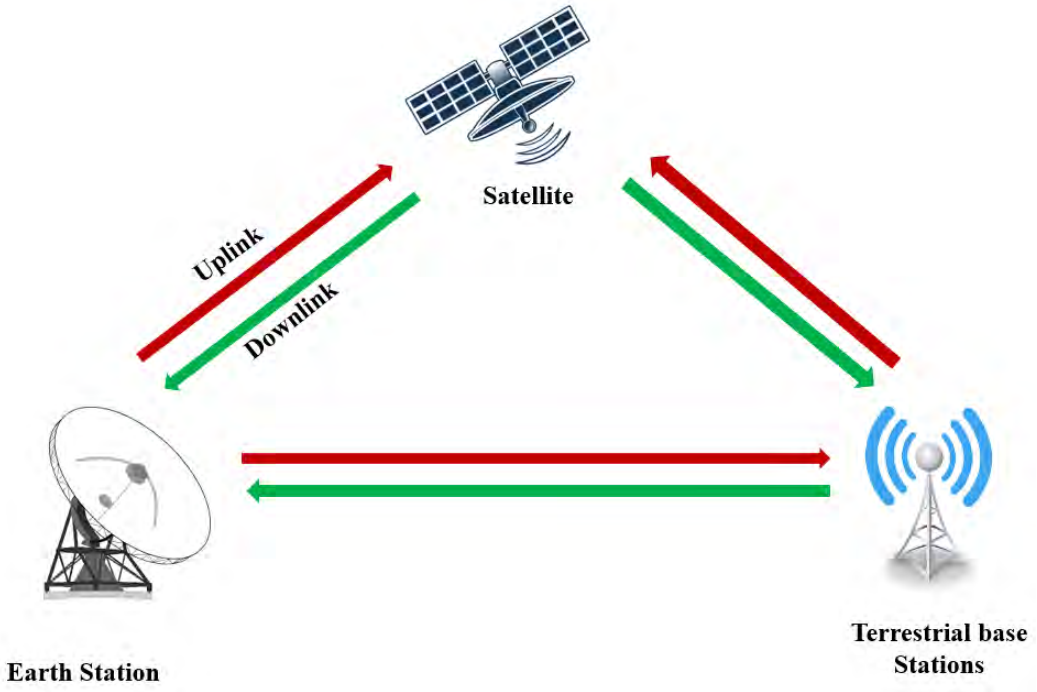

Figure 2.9: An Integrated 5G-LEO Satellite Link Description for K/Ka Band

2.14.1 Received Power Determination

Theoretically, the RF link budget equation for receiver power is given by:

$$P_r = (\frac{P_t G_t G_r c^2}{(4\pi)^2 R^2 f^2} \tag{2.9}$$

where P_r is the power received by the receiving antenna; P_t is the power applied to the transmitting antenna; G_t is the transmitter antenna gain; G_r is the receiver antenna gain; c is the speed of light ($3\times10^8 m/s$); R is the distance in Km between transmitter and receiver; f is the frequency in Hz.

In terms of decibel,

$$P_r(dBW) = P_t + G_t + G_r - 20log(f \times R) + 147.6 \tag{2.10}$$

Considering a fixed-link line-of-sight, the received signal power, P_r taking into consideration the attenuation in the atmosphere and losses in the antenna, is defined according to [43] as:

$$P_r(dBW) = EIRP - L_p - L_{atm} + G_r - L_r \tag{2.11}$$

where $EIRP$ is the effective isotropically radiated power; L_p is the path loss (free space); G_r is the receiving antenna gain; L_{atm} is the attenuation in the atmosphere; L_r is the antenna loss. $G_r - L_r$ is the net gain, G, of the receive antenna. From [43], the noise power, P_n, of the satellite at this point taking into consideration the overall system noise temperature, T_{sys} is given by:

$$P_n(dBW) = kT_{sys}B = -228.6 + 10log_{10}(T_{sys}) + 10log_{10}(B) \tag{2.12}$$

subtracting Eq. (2.12) from (2.11) gives the overall SNR of the receiver frontend up to the demodulator input. This further gives the carrier-to-noise ratio, (C/N).

$$C/N = EIRP - L_p - L_{atm} + 228.6 + 10log_{10}\frac{G}{T_{sys}} - 10log_{10}(B) \tag{2.13}$$

$$C/N_0 = EIRP - L_p - L_{atm} + 228.6 + 10log_{10}\frac{G}{T_{sys}} \tag{2.14}$$

(C/N_0) is the ratio between received signal power and noise power per unit bandwidth.

2.14.2 Path Loss Modelling

Path loss L_p describes signal attenuation between transmitter and receiver antenna as a function of the propagation distance, d. It is one mechanism causing attenuation between the transmitter power amplifier (PA) and receiver front-end system low noise amplifier. The modelling of L_p, therefore, becomes an essential tool in predicting some essential performance criterion. The calculation of L_p is given by:

$$L_p = (\frac{4\pi d}{\lambda})^2 \tag{2.15}$$

d is the distance between the satellite and the ground station and λ the propagation wavelength.

2.15 5G-LEO Satellite Link Simulation Analysis

A theoretical analysis considering the performance of the 5G-LEO Satellite link integration is carried out. Fig. 2.10 indicates the Signal-to-Noise ratio according to 5G-LEO satellite link elevation angle at different bandwidth. At 90°, the SNR of the 50 MHz frequency band is 90 dB while SNR at 400 MHz is 80 dB. Hence it is concluded that the SNR according to elevation angle decreases as the frequency increases. Similarly, as the elevation angle increases, the free space path loss faced by the transmitted signal from 5G-LEO satellite towards base station decreases as shown in Fig. 2.11. The minimum path loss is obtained at an angle of 90°.

Fig. 2.12 indicates the path loss according to the distance of 5G-LEO satellite from the ground base station. The path loss increases as the distance of the satellite from the ground base station increases. Furthermore, as the distance of the 5G-LEO satellite increases from the ground base station, the power received by the receiving antenna also decreases, which is shown in Fig. 2.13.

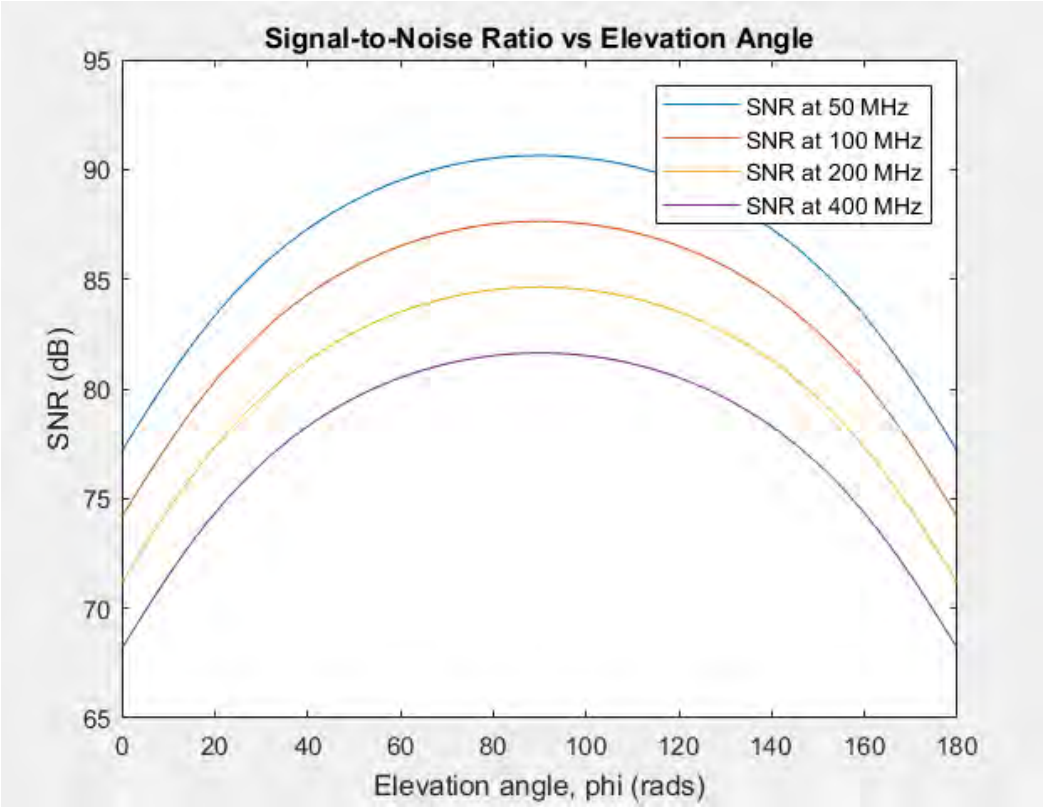

Figure 2.10: SNR Vs 5G-LEO Satellite Link Elevation Angle

2.15.1 5G-LEO Satellite Link Characterisation

In designing reliable communication links, an understanding of the optimal link resource availability and link-quality-performance such as earth-space and space-earth uplink and downlink, line-of-sight (LOS) and Non-line-of-sight (NLOS) are important. The path loss determines the large-scale fading behaviour of the communication channel with reference to the transmit power. The LOS path loss is close to free space path loss, whereas the NLOS path loss is significantly deviated owing to the difference in frequency and path terrain.

The satellite provides a transceiver path for uplink and downlink data transmission to the ground station for LEO communication at the K/Ka-band frequency. The challenge using this frequency includes the absorption of atmospheric gases, cloud attenuation, rain attenuation and group delay due to the different travel

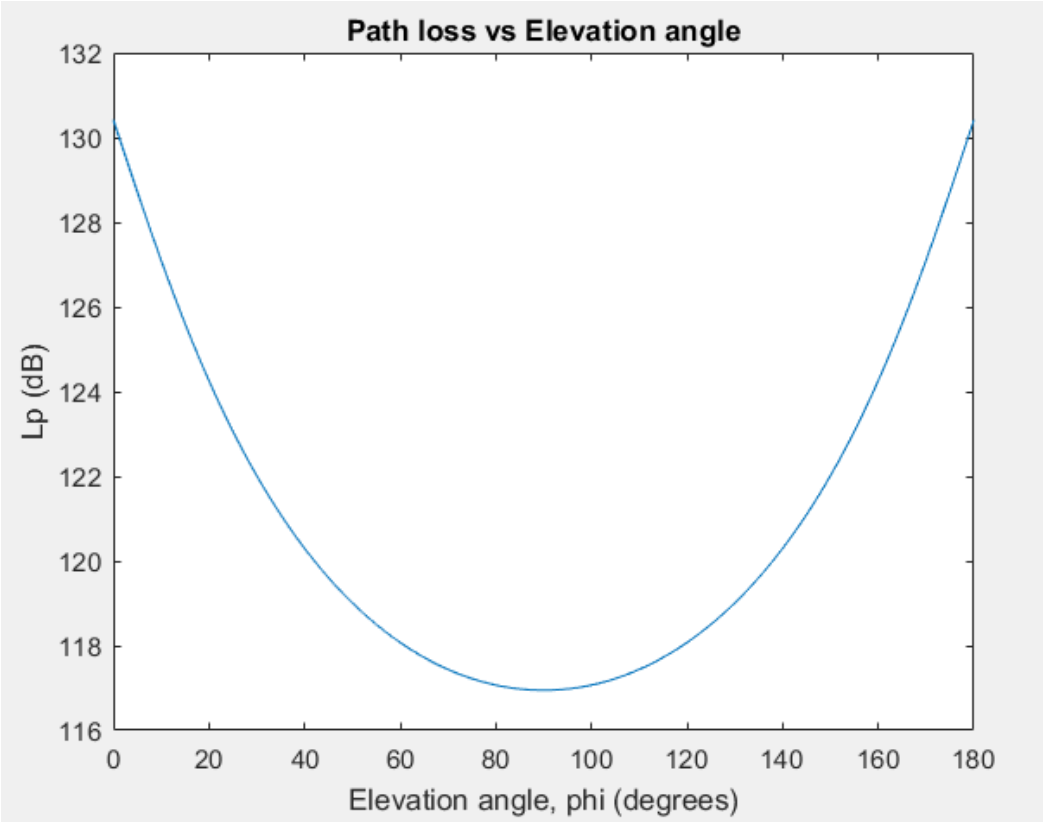

Figure 2.11: Path Loss Vs 5G-LEO Satellite Link Elevation Angle

times of different frequency components. Therefore a link characterisation to meet performance in terms of high data rate, MIMO transmission, and adaptive beam-forming for 5G application is essential.

For integrated 5G-LEO communication application, this link characterisation is enhanced by employing large antenna arrays for improved coverage, high-order modulation for required data rate, beam adaptation and wide-band availability.

Theoretically,considering the 23-28 GHz bandwidth for 5G communication at a design frequency of 26 GHz, the overall path loss is given by:

$$L_p = (\frac{4\pi d}{\lambda})^2 \tag{2.16}$$

Where d is the distance of propagation and λ the propagation wavelength.

The path loss design of any given communication application varies at any given

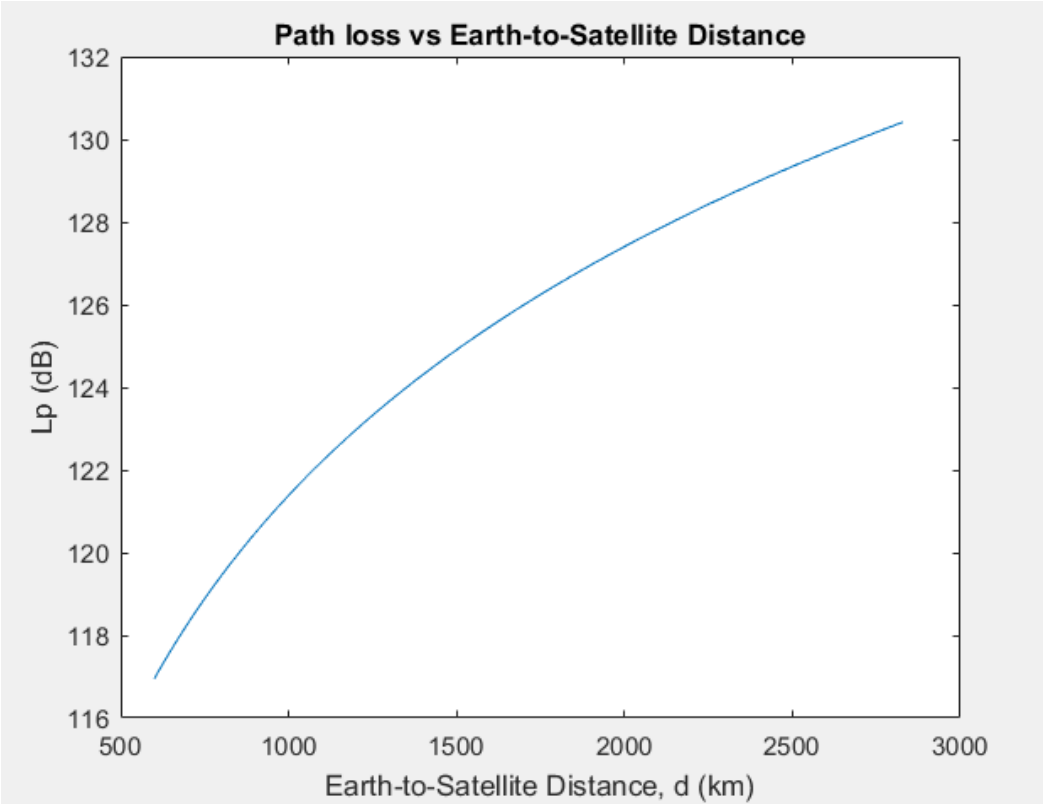

Figure 2.12: Path Loss Vs 5G-LEO Satellite Distance

distance with respect to the carrier frequency. A common path-loss model based on channel impulse responses (CIRs)is defined as:

$$L_p(f,d)[dB] = L_p(f,d_0) + 10nlog_{10}(d/d_0) + X_\sigma \tag{2.17}$$

where $L_p(f,d)$ is the path loss at different frequencies with various Tx-Rx separation distance, L_p is the path loss in dB at a close-in (CI) distance, d_0, n is the path-loss exponent and X_σ is a zero-mean Gaussian-distributed random variable with standard deviation σ.

For a small distance of 10-300 meters, the path loss at the design frequency of 26 GHz is shown in Fig. 2.14

For the link characterization simulation, the parameters in Table 2.15 are used.

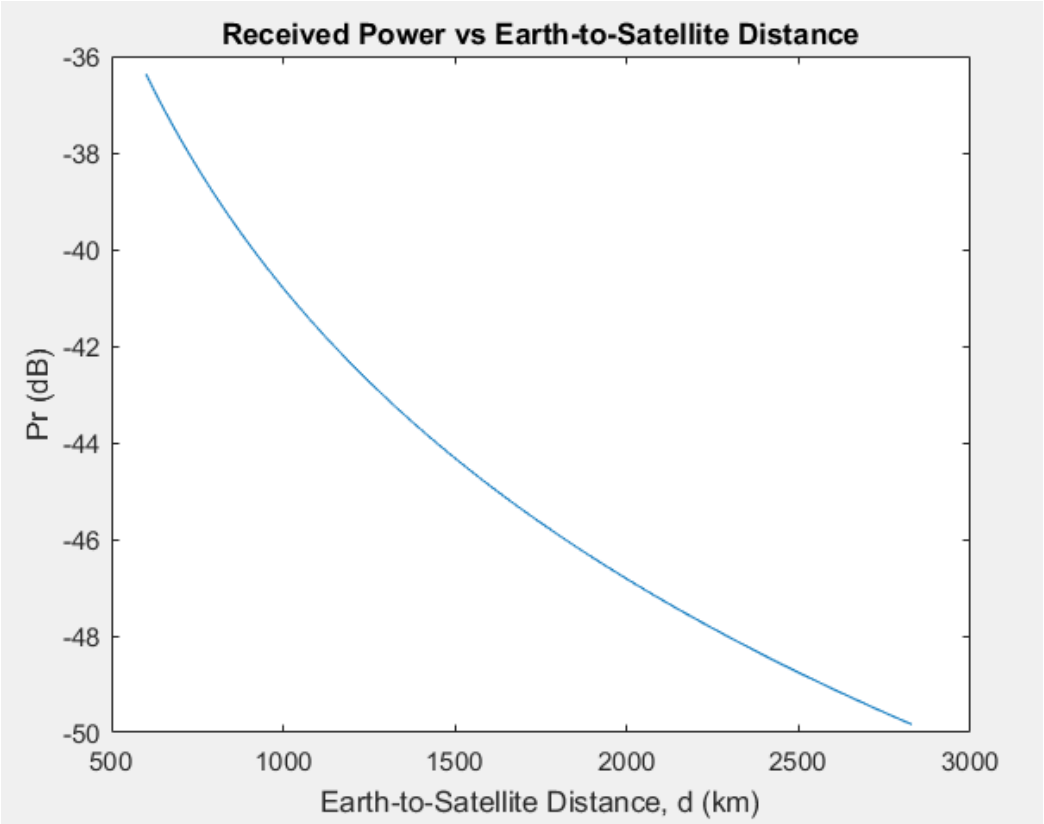

Figure 2.13: Received Power Vs 5G-LEO Satellite Distance

2.15.2 Transmitter Front-end Modelling

The transmitter is made up of two double stage up-conversion mixers as shown in Fig. 2.15. The transmitter consists of local oscillators, up-converters (mixers), filters and a power amplifier.

The transmitter is modelled at an Intermediate Frequency (IF) of 350 MHz which is double up-converted to 26 GHz with a transmission bandwidth of 550 MHz. Input power of 0 dBm is supplied to the transmitter. The power amplifier is used to increase the output power for transmission. For the transmitter, very low spur emission and intermodulation distortion (IMD) products are required. To satisfy the spur emission requirement, the unwanted level of the signals should be at least 74 dB below the required signal.

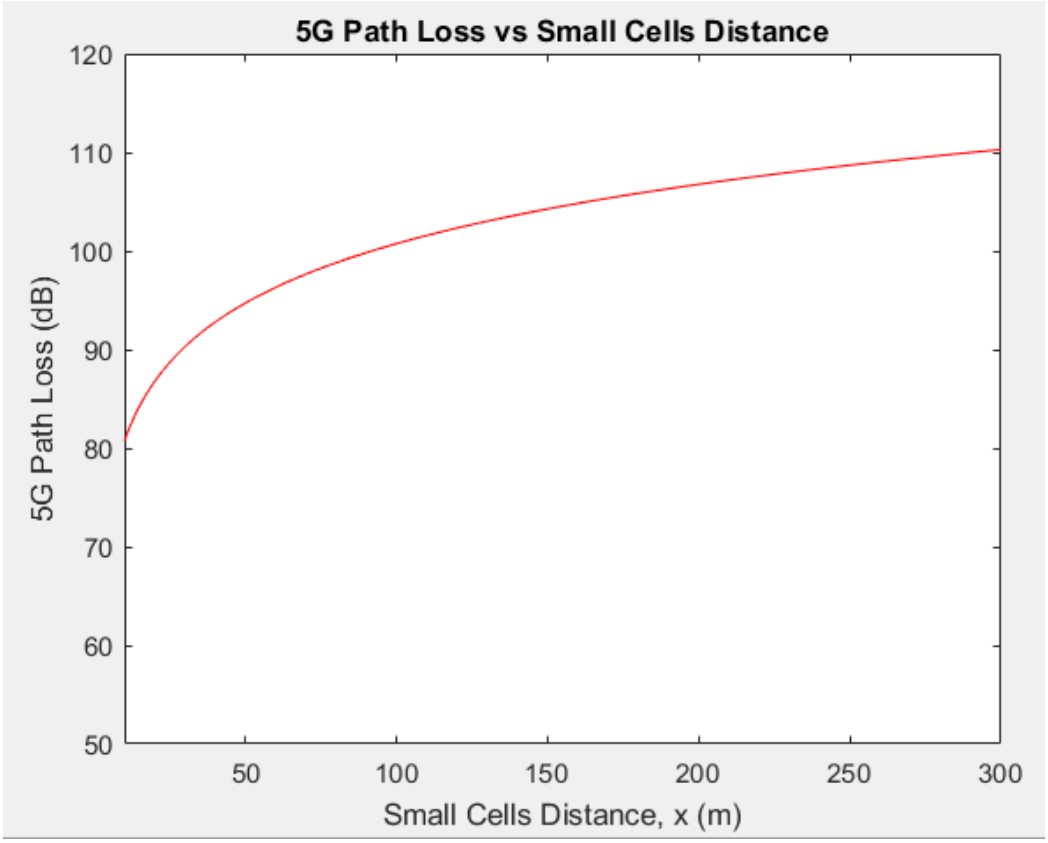

Figure 2.14: Simulated 5G NR Path Loss at 26 GHz

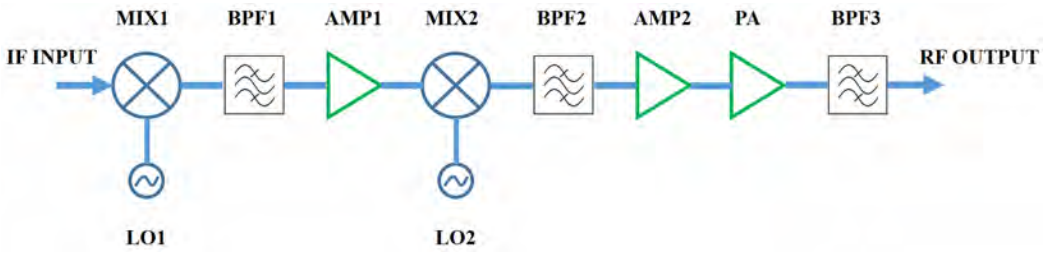

Figure 2.15: 26 GHz Transmitter Subsystems

The power output spectrum of the transmitter is shown in Fig. 2.16. The output power of 24.623 dBm after the second bandpass filter is measured from the simulation (Fig. 2.17). The cascaded voltage gain response of the transmitter subsystem components is shown in Fig. 2.18. An output gain of 26.6 dB is achieved from the design. The transmitter path noise figure is shown in Fig. 2.19. The bandpass filter at the transmitter input (BPF1) contributes signifi-

Table 2.15: Integrated 5G-LEO Frequency Planning

S/N	Parameter	Value	Unit
1	Pass-band Frequency	23 to 28	GHz
2	Intermediate Frequency (IF)	350	MHz
3	RF Carrier Frequency	26	GHz

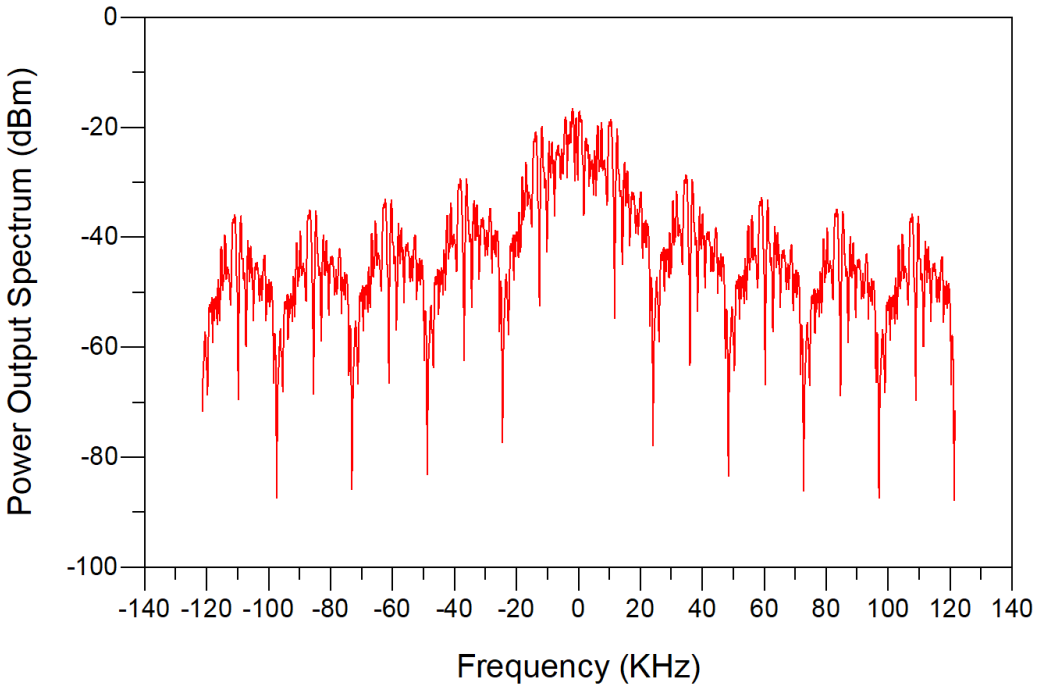

Figure 2.16: Transmitter Output Spectrum for a DQPSK signal

cantly to the noise level. However, this effect of noise is subsequently reduced at the output bandpass filter (BPF2).

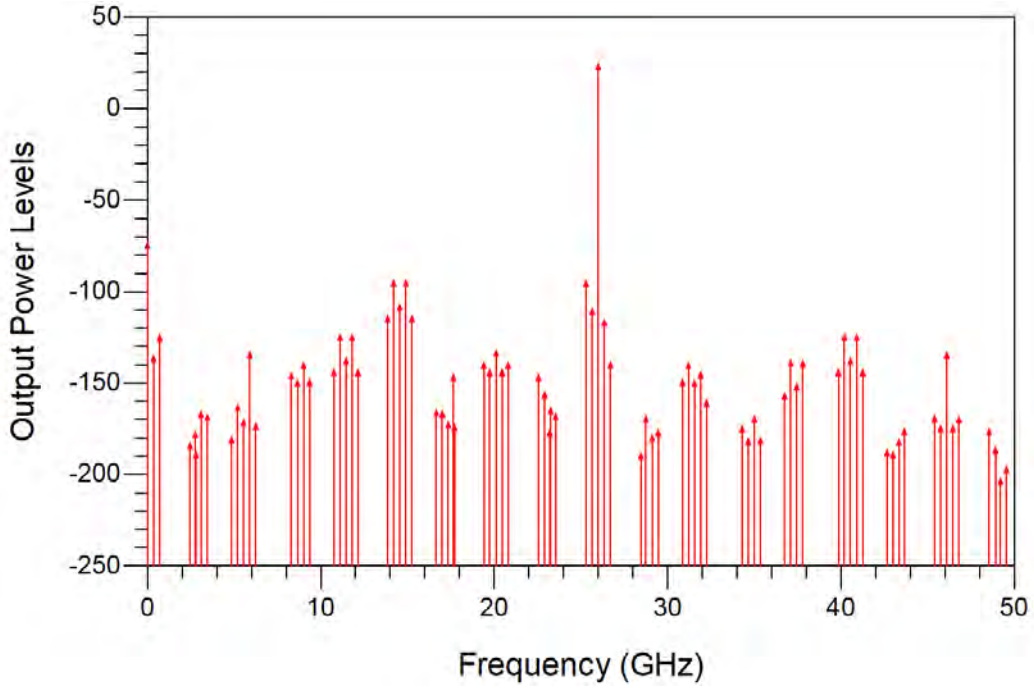

Figure 2.17: Spectral Response of the output power of the Transmitter at 26 GHz

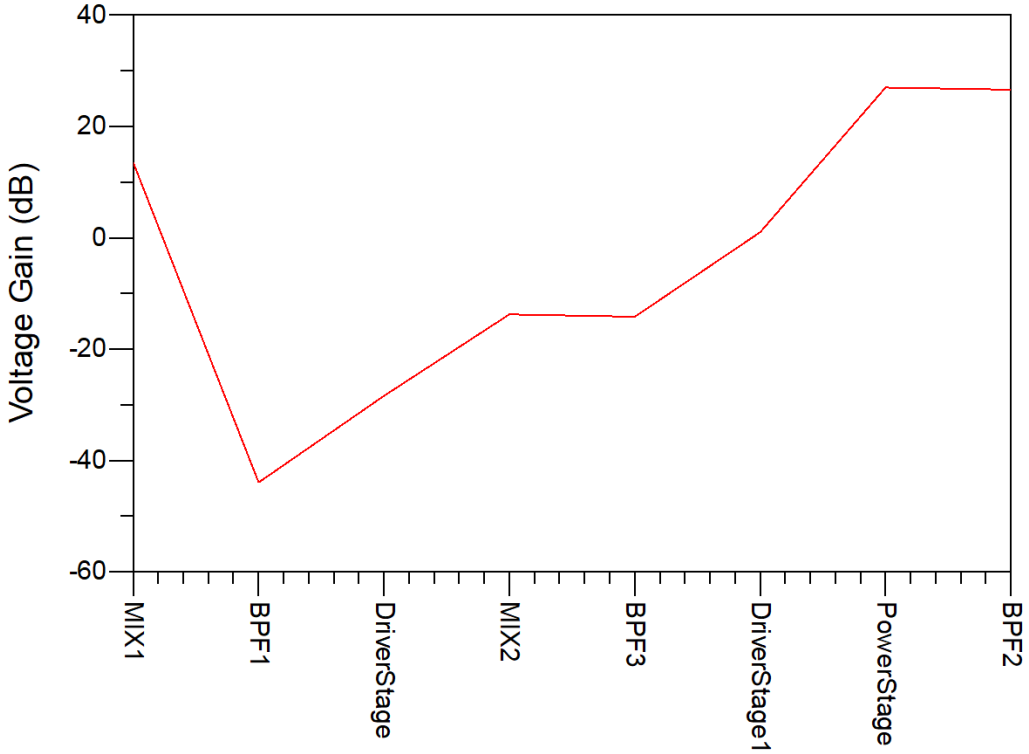

Figure 2.18: Simulated Cascaded Voltage Gain in dB of the Transmitter Subsystems

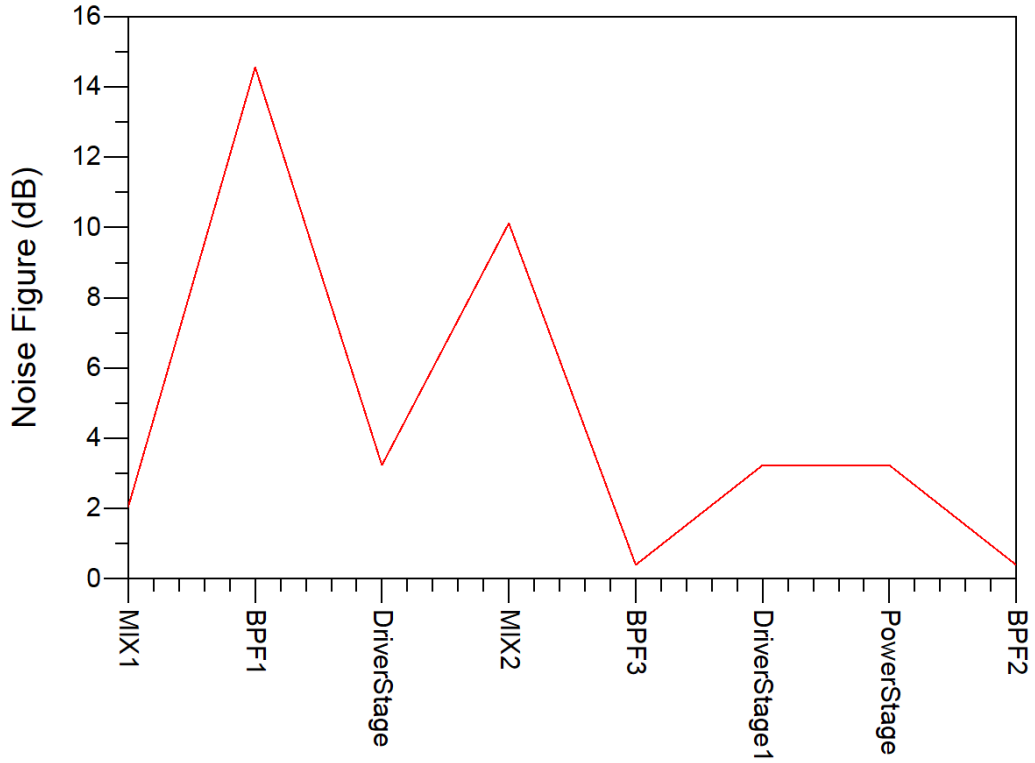

Figure 2.19: Simulated Noise figure from system input to component output of the Transmitter Subsystems

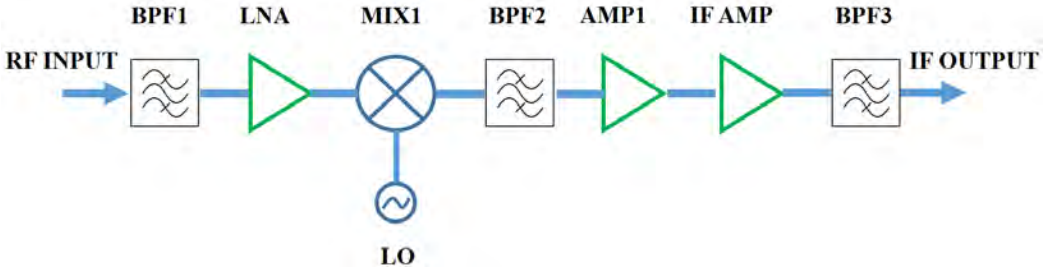

Figure 2.20: 26 GHz Receiver Subsystems

2.15.3 Receiver Front-end Modelling

The receiver is made up of a single stage down-conversion mixer as shown in Fig. 2.20. It consists of a local oscillator, down-converter (mixer), filters and a low noise amplifier.

The bandpass filter filters the out-band signals, and the required signal is then

amplified by the Low noise amplifier followed by the mixer for RF to IF conversion. An IF amplifier is added to the back-end of the receiver chain to guarantee the noise figure and gain of the receiver.

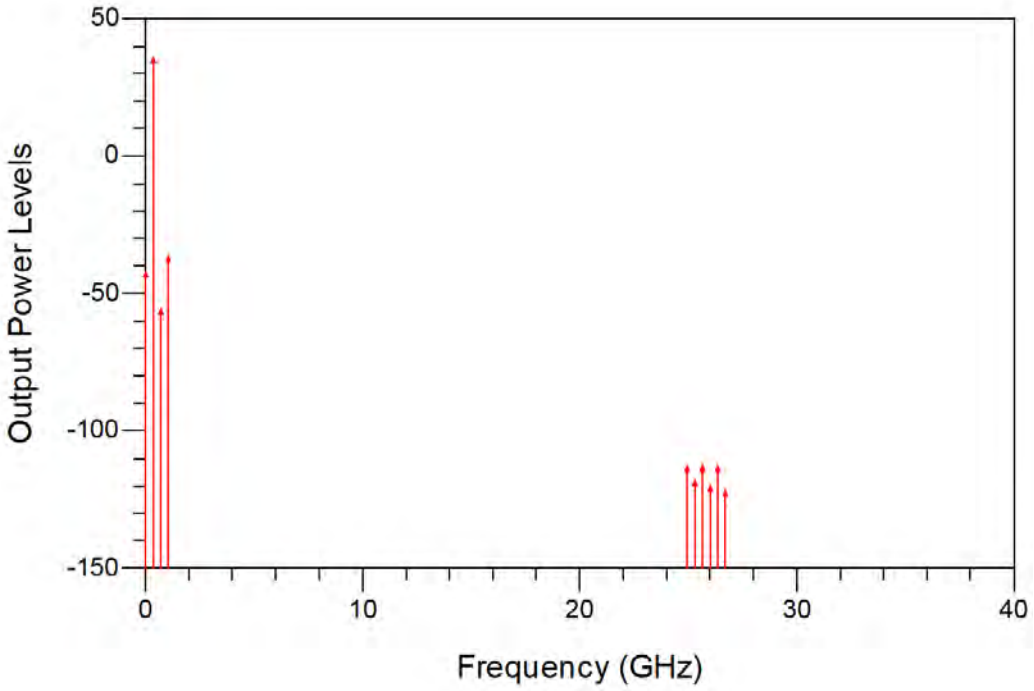

Figure 2.21: Spectral Response of the output power of the Receiver at 350 MHz IF frequency

The output power of 35.8 dBm is measured at the IF frequency (350 MHz) receiver output end from the simulation (Fig. 2.21). The simulated Cascaded Voltage Gain in dB of each of the receiver Subsystems is deduced from Fig. 2.22. From Fig. 2.23, the variation of the noise at each component is simulated. The mixer introduces significant noise into the receiver chain, which is reduced by the second bandpass filter.

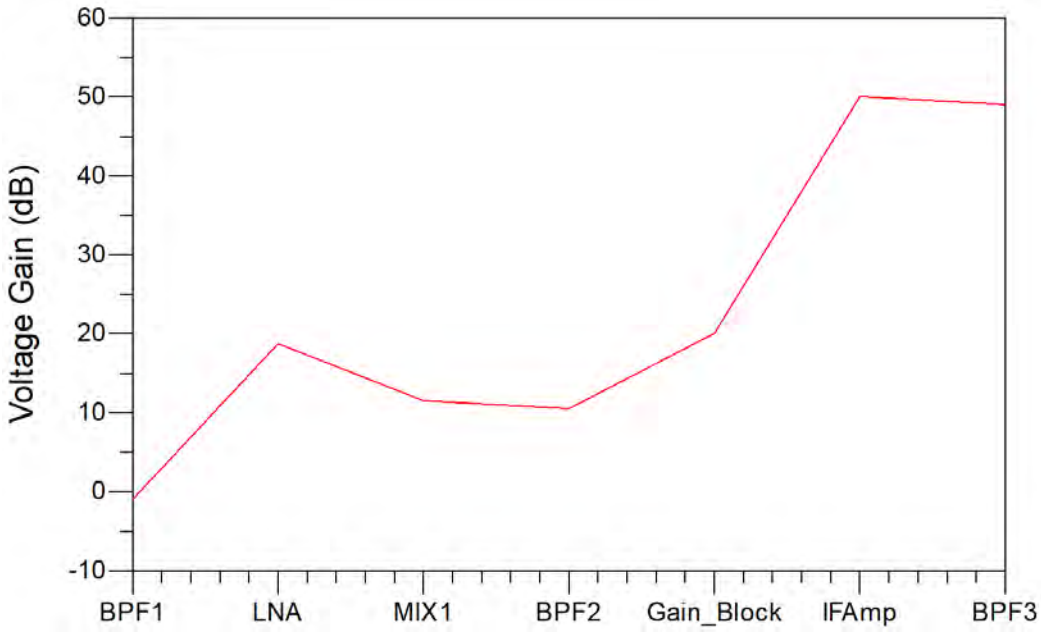

Figure 2.22: Simulated Cascaded Voltage Gain in dB of the Receiver Subsystems

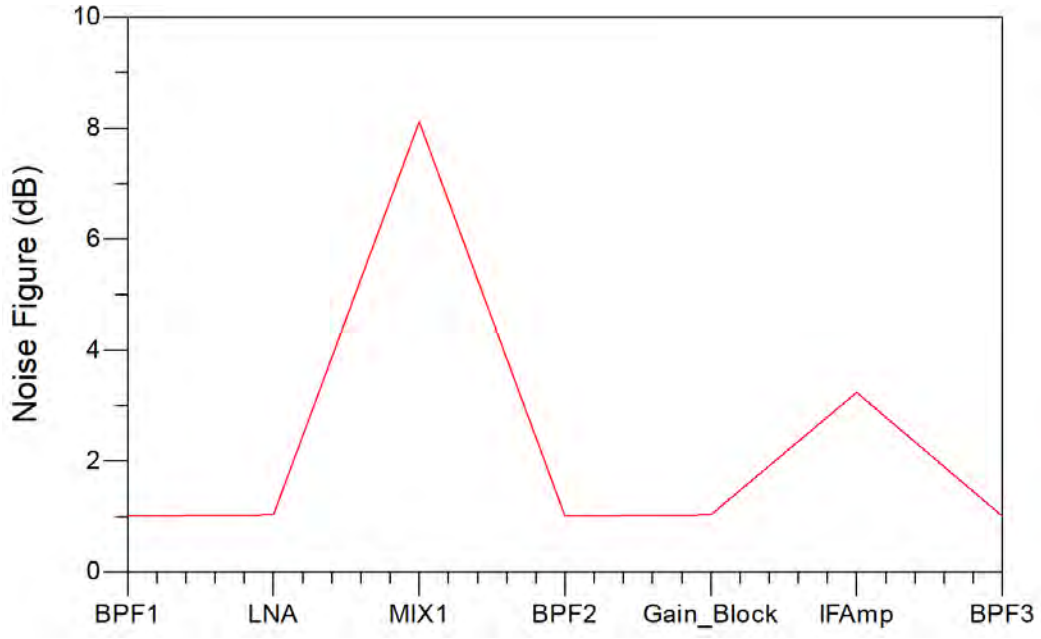

Figure 2.23: Simulated Noise figure from system input to component output of the Receiver Subsystems

2.16 Chapter Summary

This chapter discussed the design requirements for a switchable wideband receiver frontend. A review of the existing state-of-the-art LNAs with wideband capabilities for X and K/Ka-band frequencies were outlined. It began with a look at 5G communication evolution, the requirements for multi-band/ multimode architecture, software defined radio technologies, active semiconductor materials available for implementing a wideband, low-noise performance for seamless connectivity. Furthermore, this chapter discusses the design procedure and requirements for two broadband low noise amplifiers based on an inductive source-degenerated cascade architecture that would be integrated with a SPDT switch for the wideband switchable architecture in Chapter 3. In addition, the three types of LNA topologies were reviewed and classified based on noise figure, gain, stability, linearity and sensitivity to process variation. Link budget analysis and simulation of a satellite-5G cellular convergence network was also covered. Chapter 3 discusses the design methodology for the proposed highly adaptive reconfigurable receiver frontend.

Chapter 3

Design Methodology for Highly Adaptive Reconfigurable Receiver Front-end (HARRF)

A highly adaptive reconfigurable receiver front-end (HARRF), using an SPDT switch for 5G and Satellite applications, is proposed to adapt its functionality between X-band (for radar and X-band satellite applications) and K/Ka-band frequencies for wideband switchable applications. The K/Ka-Band frequency caters for the millimetre wave frequency range (FR2) 5G communication applications. First, conceptual design objectives for a switchable receiver frontend between X and K/Ka-band frequencies are defined, followed by design parameter specifications. Performance metrics such as linearity, noise figure, and gain are investigated and compared with existing and emerging standards. The design process flow is shown in Fig. 3.1.

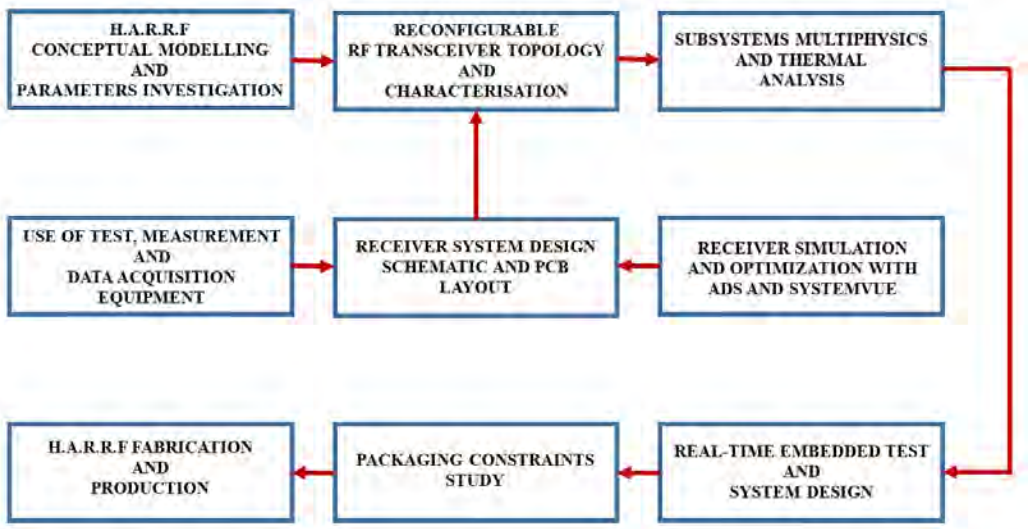

Figure 3.1: The HARRF methodology

3.1 Switchable Receiver Front-end Architecture: HARRF LNA and SPDT Integration

The switchable wideband receiver frontend design (including LNA and SPDT Switch) for 5G and satellite applications is carried out in advanced design software (ADS), creating several scenarios to optimise communication system performance. Cascade topology is chosen for the LNA because of its comparative advantage over the common-source and common-gate topology in terms of high gain and better impedance matching to achieve the low noise performance requirement of various wireless standards from diverse frequency bands [89].

Figure 3.2 shows the proposed receiver frontend module architecture for the HARRF 5G and Satellite receiver system. Two LNAs, capturing the X-band frequencies and K/Ka-band frequencies, are incorporated into the system with an SPDT switch carrying out the frequency selection responsibility. Transmission lines are used to integrate the SPDT with the LNAs to achieve a compact chip area. This proposed switchable receiver frontend architecture is adapted to two modes: the X-band mode and the K/Ka-band mode using voltage controlled

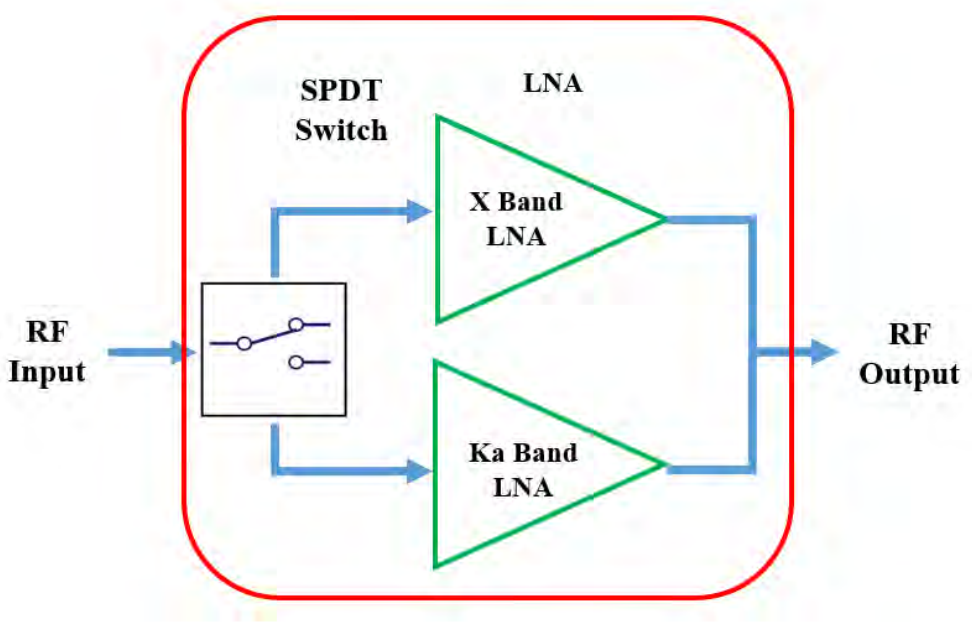

Figure 3.2: Proposed SPDT switch-based Reconfigurable Low Noise Amplifier Architecture

SPDT switch. The SPDT switch acts as a drive stage where the input RF signal is received. The transmission lines linking the LNAs forms part of the input matching network for each of the frequency arms.

3.2 Active Device Technology S-Parameter Extraction using ADS

The choice of active and passive elements are essential in the device technology selection due to the high losses at mmWave frequencies. At low frequencies, characterisation of the active device components are done using the impedance and admittance parameters, which provides a linear relationship between the input and output voltages and currents. However, at microwave frequencies, power measurements parameter such as the S-parameter are used to consider how a signal is distributed across the various ports of the microwave network. This

parameter captures the substrate losses and quality factor of matching networks, as transmission line insertion loss decreases with higher resistivity substrates.

To understand the non-linear characteristics of the pHEMT active device using S-Parameter extraction, DC and RF test simulation over different bias conditions are carried out to determine the operating point of the transistor. The I-V characteristics at various biasing points of the Indium Gallium Arsenide (InGaAs) pseudomorphic high electron transistors are shown for a 2 x 50 µm InGaAs pHEMT in Fig. 3.3 and for a 4 x 50 µm InGaAs pHEMT Fig. 3.4. The drain current (I_{ds}) is plotted against the drain-source voltage (V_{ds}).

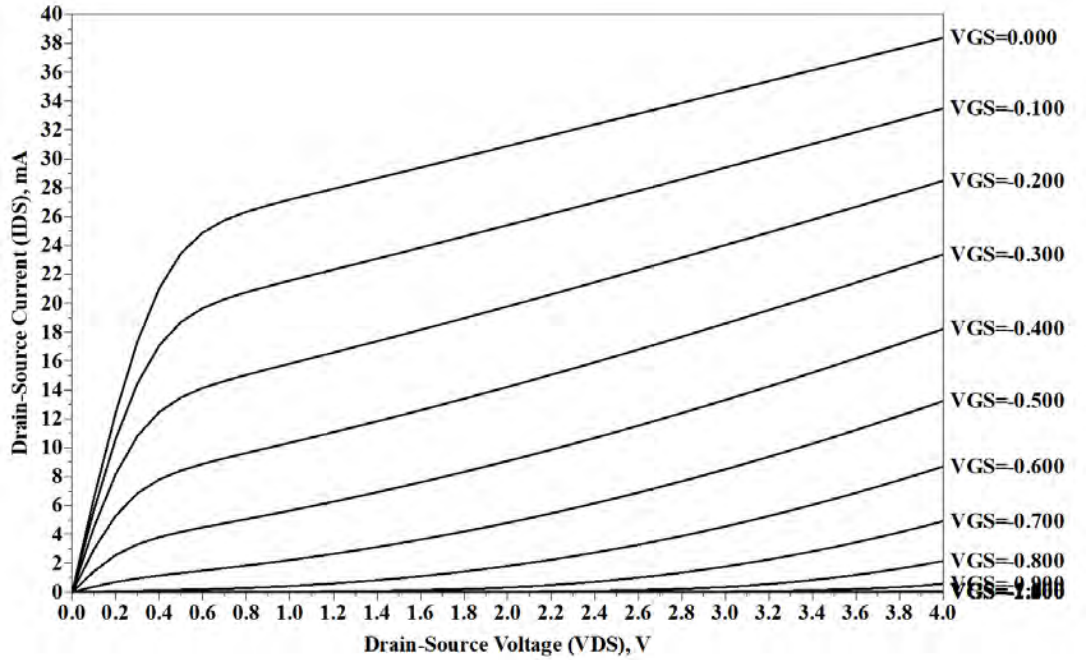

Figure 3.3: I-V characteristics for a 2 x 50 µm InGaAs pHEMT

This test is performed to determine an appropriate operating-point for the required LNAs, taking into consideration design requirements (especially the dissipated power). The operating point was chosen to be at a drain-source voltage (V_{ds}) = 2 V, gate-source voltage (V_{gs}) = -0.3 V and drain-source current (I_{ds}) = 0.021 A taking into consideration the power consumption, which is chosen to

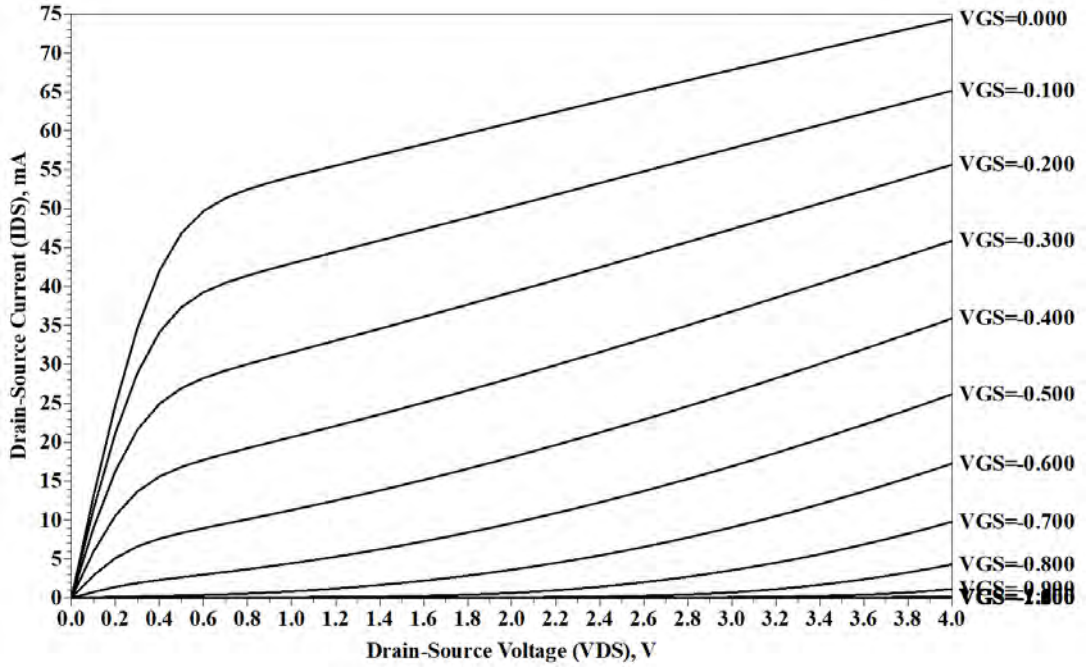

Figure 3.4: I-V characteristics for a 4 x 50 µm InGaAs pHEMT

be less than 0.14 W for a three-stage LNA design. The pHEMT transistor was modelled at the optimum low-noise bias for each of the designed LNAs.

Fig. 3.5 and Fig. 3.6 show the characteristics curves for the transconductance of a 2 x 50 µm and 4 x 50 µm Indium Gallium Arsenide (InGaAs) pHEMTs respectively. The transconductance is plotted as the reciprocal of resistance to the transistor's drain current and it shows the relationship between current through the output (drain) of the transistor and voltage across the input (gate) of the transistor. Mathematically,

$$g_m = \frac{\Delta I_{ds}}{\Delta V_{gs}} \tag{3.1}$$

From Fig. 3.5, the transconductance value obtained is 81mS at (V_{ds}) = 2 V, (V_{gs}) = -0.3 V and (I_{ds}) = 0.021 A.

For a pHEMT device, the load reflection coefficient, Γ_{opt}, brings about a mismatch for a maximum power transfer condition which is much different from the conjugate reflection coefficient of the input return loss, S_{11}. However, with the

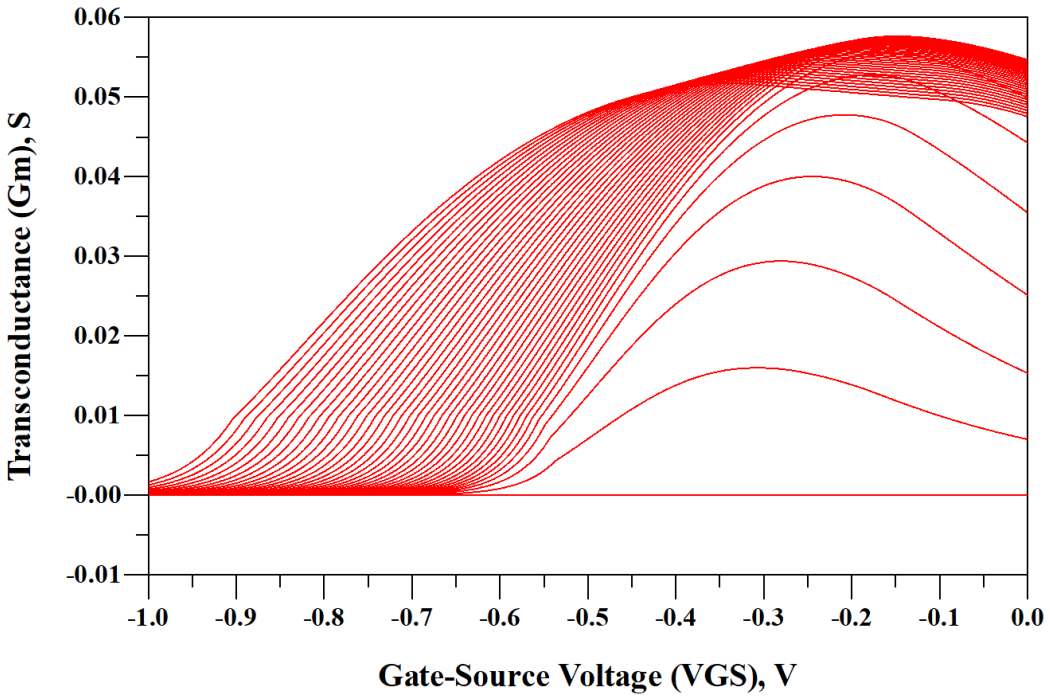

Figure 3.5: Curves of the transconductance for a 2 x 50 µm InGaAs pHEMT.

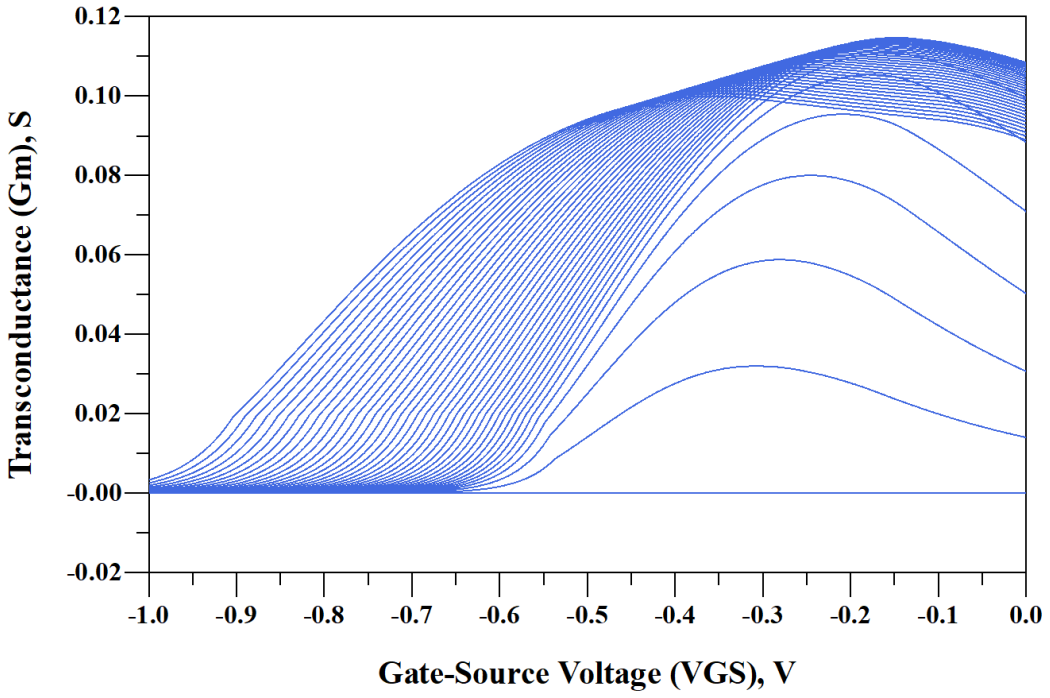

Figure 3.6: Curves of the transconductance for a 4 x 50 µm InGaAs pHEMT.

right active device (transistor) selection, the Γ_{opt} and input return loss, S_{11} can be made much closer in value, resulting in a better output-power while still achieving low noise.

3.3 HARRF LNA Design

Two LNAs are designed using a 0.15 µm gate length Indium Gallium Arsenide (InGaAs) pseudomorphic high electron transistor (pHEMT) technology. The X-band LNA spans 8-12 GHz with an absolute bandwidth limit of 4 GHz. Its geometric centre-design frequency, f_c is 9.8 GHz, allowing for a fractional bandwidth of 0.408 GHz. The K/Ka-band LNA spans 23-28 GHz with an absolute bandwidth of 5 GHz. Its geometric centre-design frequency, f_c is 25.4 GHz, allowing for a fractional bandwidth of 0.197 GHz. Both LNAs are a three-stage cascaded design with separated gate and drain lines for each transistor stage. The first stage design of both LNAs has been optimised for better noise figure and input match whereas the second and third stages for high gain flatness, and high output power, respectively. The LNAs are designed to meet the unconditional stability criteria [3].

3.3.1 X-Band LNA Design Procedure

The X-Band LNA design spans 8-12 GHz of the electromagnetic spectrum. A three-stage X-Band low noise amplifier was designed using a 0.15 µm low noise InGaAs pseudomorphic high electron mobility transistor process technology. The various design parameters (forward transmission gain, minimum noise figure, S-Parameter extraction, noise resistance, input and output isolations) were obtained at a bias gate-source voltage, V_{gs} = -0.3 V and drain-source voltage, V_{ds} = 2 V. This bias point was chosen to reduce the current dissipation and maintain an

acceptable performance level of the LNA. Also, this common bias network is used to ensure equal distribution of current to all stages. The resonant frequency for this design was $f_d = 10$ GHz. The three-stage LNA structure is shown in Fig. 3.7.

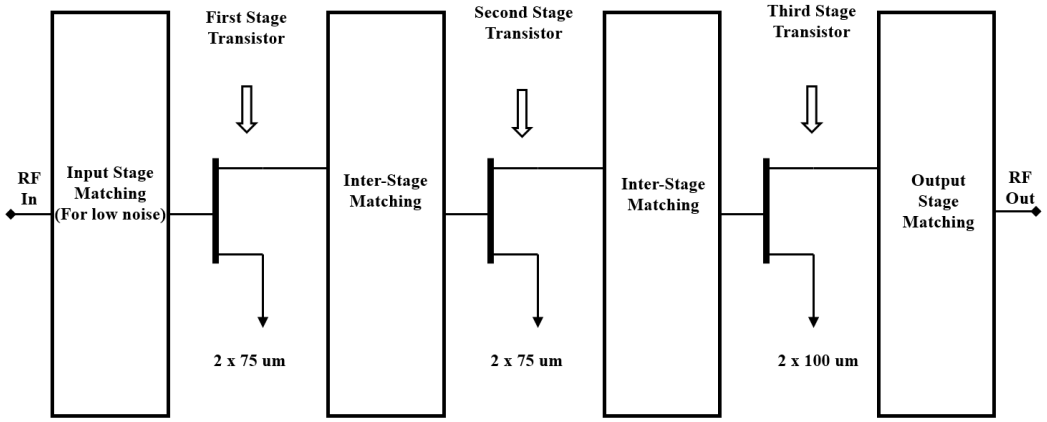

Figure 3.7: Three-stage LNA structure

- Stage one: The first stage is made up of a 2 x 75 µm transistor with source inductive feedback for stabilization. The inductive series feedback in the first stage drives the optimum noise match closer to the optimum gain match, presenting the optimum match, Γ_{opt} over the operating frequency to the gate of the first stage transistor with a 50 Ω input source. A series LC network was utilized for the input match.

- Stage two: The second stage is made up of a 2 x 75 µm transistor. An inter-stage matching network was designed to transform the output impedance of the stage one transistor to the input impedance of the second stage transistor for maximum stable gain and adequate linearity.

- Stage three: The third stage is made up of a 2 x 100 µm transistor. An inter-stage matching network was designed to transform the output impedance of the stage two-transistor to the input impedance of the third stage transistor

for maximum stable gain. Parallel feedback between the input and output of the third stage is introduced for gain flatness.

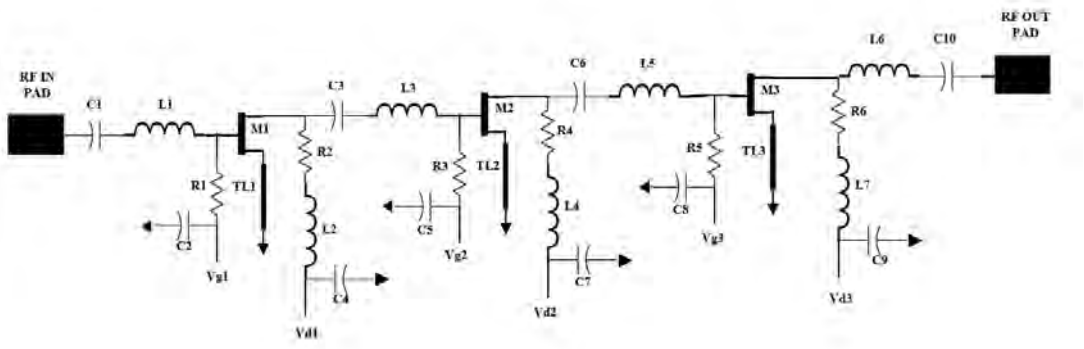

Figure 3.8: A Three-Stage 8-12 GHz MMIC LNA Design Schematic

Figure 3.8 shows the schematic of the X-Band LNA, designed to achieve a low noise figure. C1 and C10 act as dc blocks, preventing dc voltage from passing through the RF path. C2, C4, C5, C7, C8 and C9 are decoupling capacitors in parallel to the supply voltage. They prevent any RF signal from leaking into the voltage supply path. R1, R3, R5 are high resistive loads that prevent RF leakage into the voltage supply path. C1 and L1 combine for the first stage optimum noise input matching network. The optimisation of the first stage for a minimum noise figure with sufficient gain is required. Inductor L6 and capacitor C10 constitute the output matching network for the single-ended MMIC LNA topology design.

The pHEMTs devices are M1, M2 and M3 (Fig. 3.8). For the first stage, second stage and third stage active devices of the LNA, a DC blocking capacitor and inter-stage matching inductor is incorporated for maximum power transfer. The input matching network consisting of C1 and L1 presents an optimum noise match terminated at 50 Ω was maintaining sufficient gain and low input reflection.

Figure 3.9 shows the layout of the designed X-Band MMIC LNA.

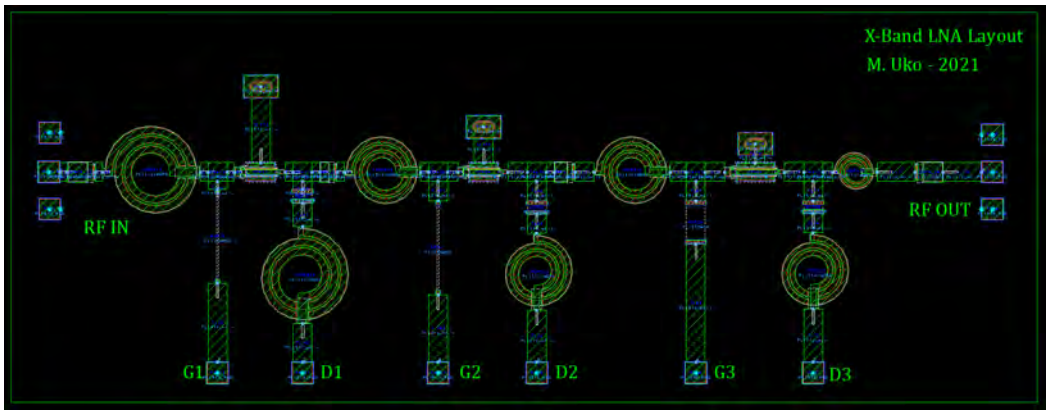

Figure 3.9: Layout of the Three-Stage 8-12 GHz MMIC LNA

3.3.2 K/Ka-Band LNA Design Procedure

The K/Ka-Band LNA design spans 23-28 GHz of the electromagnetic spectrum covering the 24.25-27.5 GHz band earmarked for 5G. A three-stage K-Band low noise amplifier was designed using a scalable PL15-10 0.15 µm low noise InGaAs pseudomorphic high electron mobility transistor process technology provided by WIN Semiconductors. At millimetre-wave frequencies, the conventional single-stage amplifier exhibits relatively low gain. Also, the effects of parasitic and passive losses are higher at these frequencies. Increasing the number of stages to three (3), enhances the overall gain, though this leads to an increase in the power consumption of the designed LNA.

The various design parameters (forward transmission gain, minimum noise figure, S-Parameter extraction, noise resistance, input and output isolations) were obtained at a bias gate-source voltage, V_{gs} = -0.3 V and drain-source voltage, V_{ds} = 2 V. The resonant frequency for this design was f_d = 25 GHz. Spiral inductors and MIM capacitors are used for the matching networks. Fig.3.10 shows the design topology of the three-stage K/Ka Band LNA.

- Stage one: The first stage is made up of a 2 x 50 µm transistor with source inductive feedback for stabilisation. It is designed for low noise, present-

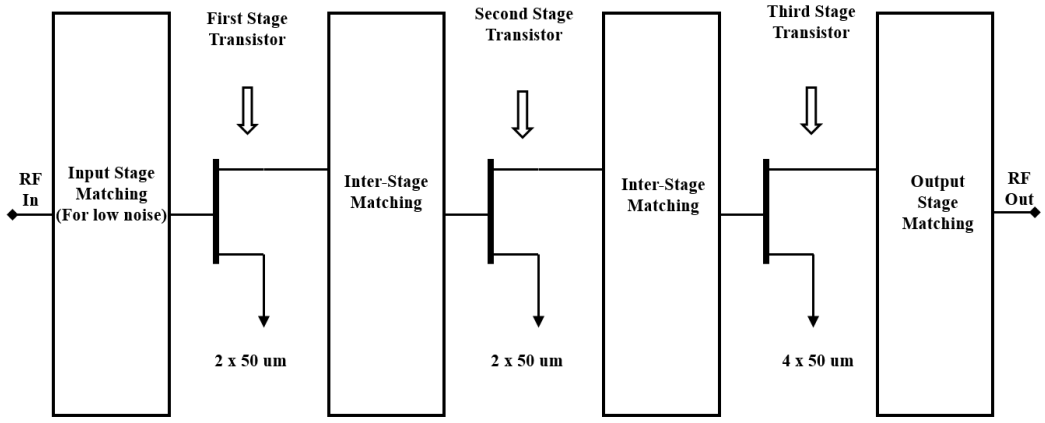

Figure 3.10: Three-Stage K/Ka Band LNA Topology

ing the optimum match, Γ_{opt} over the operating frequency to the gate of the first stage transistor with a 50 Ω input source. The inter-stage matching networks are adjusted to help transform the source impedance to the optimum noise impedance.

- Stage two: The second stage is made up of a 2 x 50 µm transistor. Inter-stage matching network was designed to transform the output impedance of stage one transistor to the input impedance of the second stage transistor for maximum stable gain.

- Stage three: The third stage is made up of a 4 x 50 µm transistor. An inter-stage matching network was designed to transform the output impedance of stage two-transistor to the input impedance of the third stage transistor for maximum stable gain. Parallel feedback between the input and output of the third stage is introduced for gain flatness.

Fig. 3.11 shows the schematic of the K/Ka-Band LNA, designed to achieve a low noise figure. C1 and C11 act as dc blocks, preventing dc voltage from passing through the RF path. C2, C4, C5, C7, C8 and C10 are decoupling capacitors in parallel to the supply voltage. They prevent any RF signal from leaking into the voltage supply path. R1, R3, R5 are high resistive loads that prevent RF leakage

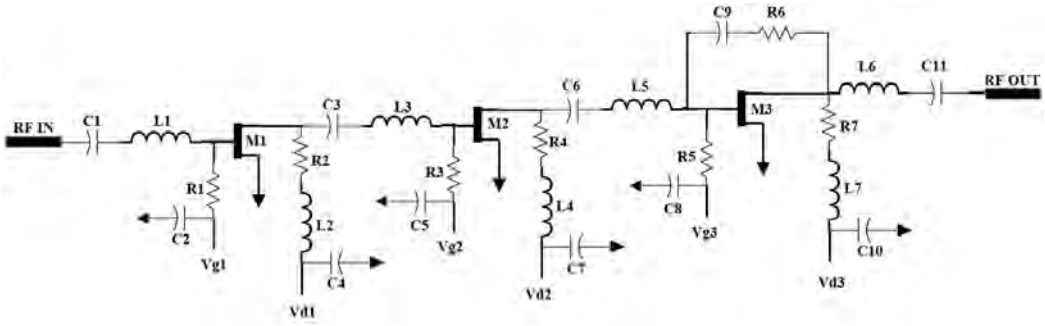

Figure 3.11: Schematic of K/Ka-Band LNA

into the voltage supply path. The series RC network made of C9 and R6 is used in the third stage as series feedback for gain flatness. C1 and L1 combine for the first stage optimum noise input matching network. The optimisation of the first stage for a minimum noise figure with sufficient gain is required. L6 and C11 combine for the output matching network. The active transistor devices are M1, M2 and M3 for the first stage, second stage and third stage respectively.

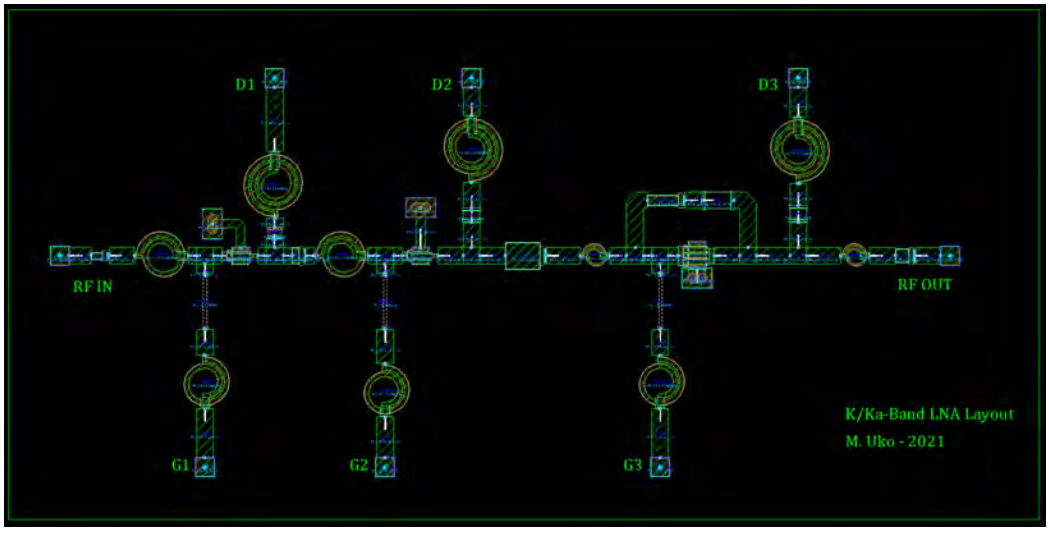

Figure 3.12: Layout of the Three-Stage 23-28 GHz MMIC LNA

Figure 3.12 shows the layout of the designed K/Ka-Band MMIC LNA.

3.4 HARRF SPDT Design

The broadband SPDT switch is designed over the frequency range from DC-50 GHz for 5G communication applications. The series and shunt FET switching elements make use of a depletion mode scalable PL15-10 0.15 µm InGaAs pseudomorphic high electron mobility transistor (pHEMT) process technology. When used as a switch, the pHEMT can be modelled as a small value resistor in the "ON" state or as a parallel resistor-capacitor in the "OFF" state. In the "ON" state, the control voltage for the gate is biased at 0V, while in the "OFF" state, the control voltage for the gate is biased beyond pinch-off voltage (-1.5 V for this work). At 0 V on the gate, there is a low resistance signal path, and the transistor is on. As the gate voltage reduces, the resistance increases and the transistor is off. The RF signal path is the drain to the source, and the gate is the control terminal where the gate voltages are applied through large resistors. The drain-source voltage is swept around 0 V for different gate voltages. In order to achieve high linearity, a stacked transistors configuration is adopted to divide the voltage swing across the transistors.

A distributed topology is adopted for the SPDT switch design, as shown in Fig. 3.13. The distributed topology made up of two series FETs and four cascaded-stacks of shunt FETs in each arm with equal gate bias voltage and bias resistors is used to extend the operating frequency of the switch by absorbing the off-state capacitance of the shunt FETs into a low pass filter.

The shunt FETs (M3-M10, M13-M20) in the "ON" state arm are at pinched-off voltage when the series FET is switched on while the FETs in the "OFF" state arm are switched on when the series FETs (M1, M2, M11 and M12) are at pinched-off voltage. In Fig. 3.13, the control voltages V1 and V2 are complimentary (V1 being "low" when V2 is "high" and vice versa). The shunt FETs are incorporated in the distributed SPDT design to improve the switch isolation

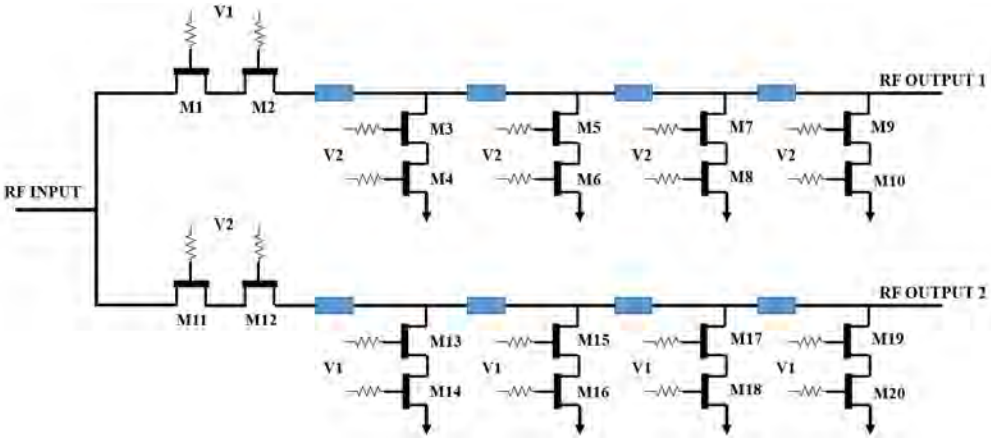

Figure 3.13: Schematic of the designed distributed SPDT Switch

without causing an excessive increase in insertion loss. The series FETs are incorporated to improve the power handling capability of the switch by increasing the size of the FETs used, which increases the drain-source current, I_{DS}. The series FETs are made up of a 3 x 275 µm size device.

3.5 Chapter Summary

This chapter outlined the design methodology for a highly adaptive reconfigurable receiver frontend (HARRF). The proposed frontend architecture is designed using the 3D software: Advance Design Software. Two LNAs, each capturing the frequency range for X and K/Ka-Band applications, are integrated with an SPDT switch to form the proposed architecture. An I-V characteristics for a 2 X 50 µm and 4 X 50 µm transistor size was analysed, to find an optimum operating point for the LNAs designs. Each of the LNAs are designed using a three-stage cascaded topology for maximum gain and low noise performance. The SPDT switch is designed using series and shunt FET transistors for switching capabilities. In addition, a distributed topology made up of two series FETs and four cascaded-stacks of shunts FETs are used for switching between ON and OFF states. The LNAs and SPDT are integrated using transmission lines. Chapter 4 captures the

simulation results and analysis of the proposed HARRF architecture.

Chapter 4

Results and Discussion

The simulated performance of the designed LNAs using ADS is presented below. The results from this simulation show a good correlation with required communication standards.

4.1 X-Band LNA Responses and Discussion

4.1.1 X-Band LNA Analysis

The LNA S-parameters are shown in Fig. 4.1. It can be observed that the output and input return losses are less than 10 dB for the entire band. The output return loss was designed to be less than 22 dB. The gain shown in Fig. 4.2 is 40 dB at the centre design frequency, with an in-band ripple factor of 1dB across the required band. The isolation loss is shown to be below 50 dB in Fig. 4.3

The minimum noise at the resonant frequency of 10 GHz was 0.9 dB (Fig. 4.4). Considering the Rollete stability factor, K, the LNA is stable across the entire band up to cut-off frequency, as shown in Fig. 4.5. A summary of the designed LNA performances is given in Table 4.1.

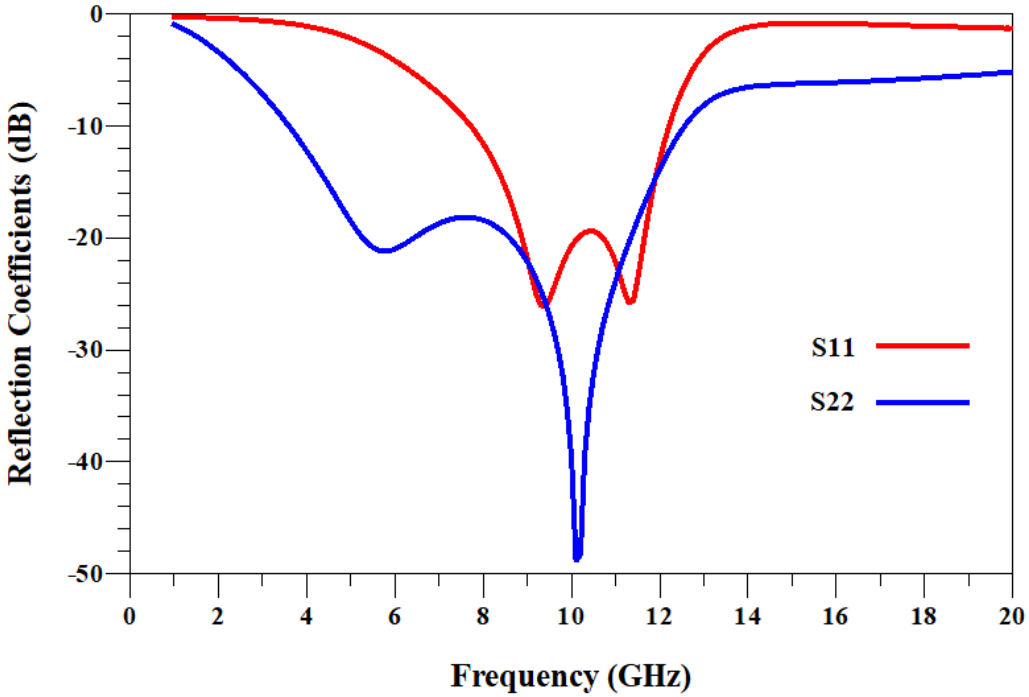

Figure 4.1: Input and Output reflection coefficient of the X-band MMIC LNA circuit

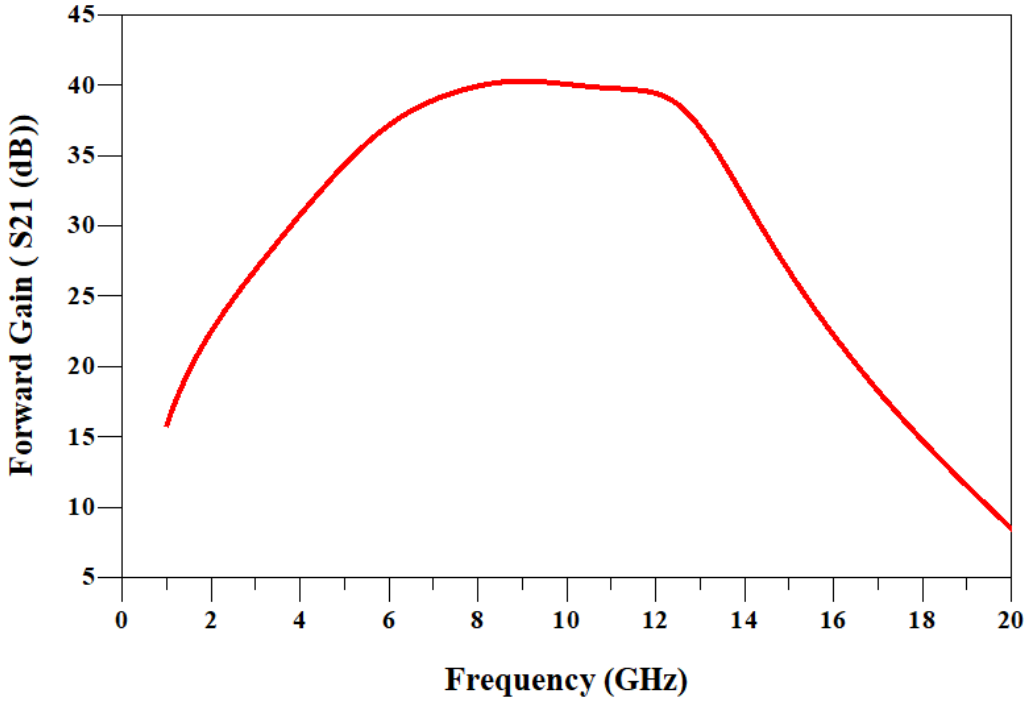

Figure 4.2: Gain of the X-band MMIC LNA circuit

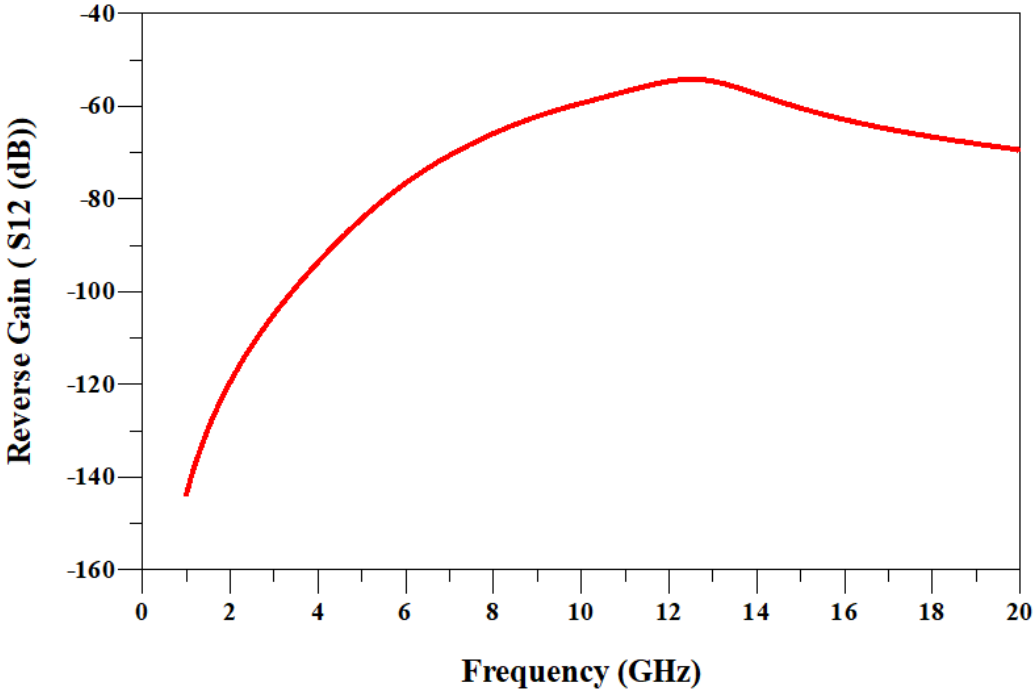

Figure 4.3: Isolation of the X-band MMIC LNA circuit

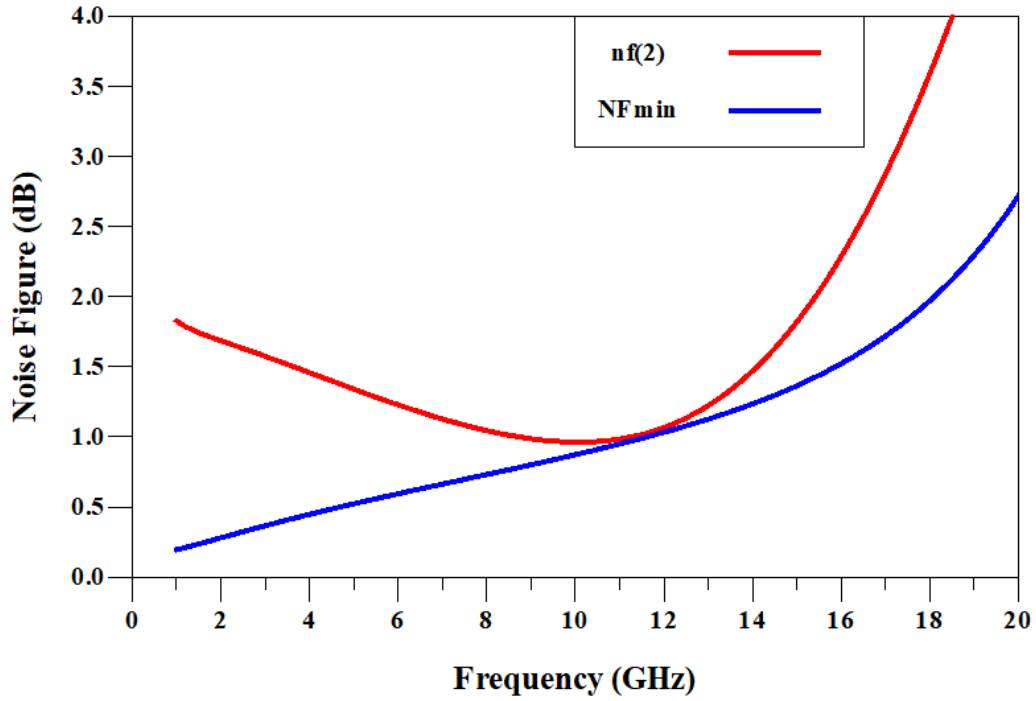

Figure 4.4: Noise Figure of the X-band MMIC LNA circuit

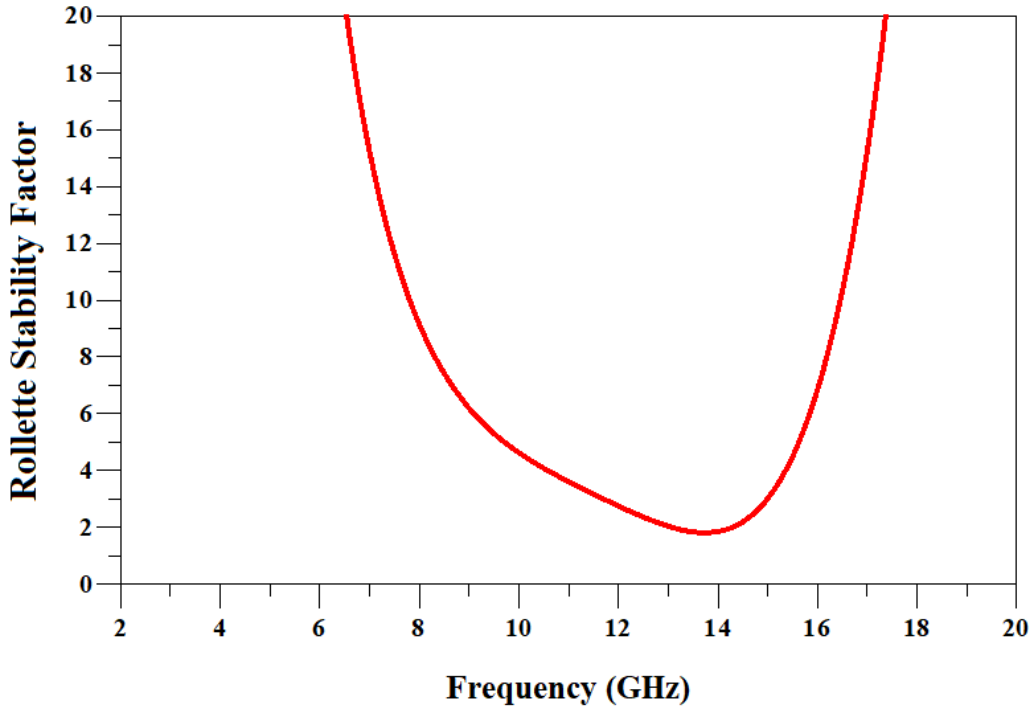

Figure 4.5: Rollette Stability Factor of the X-band MMIC LNA circuit

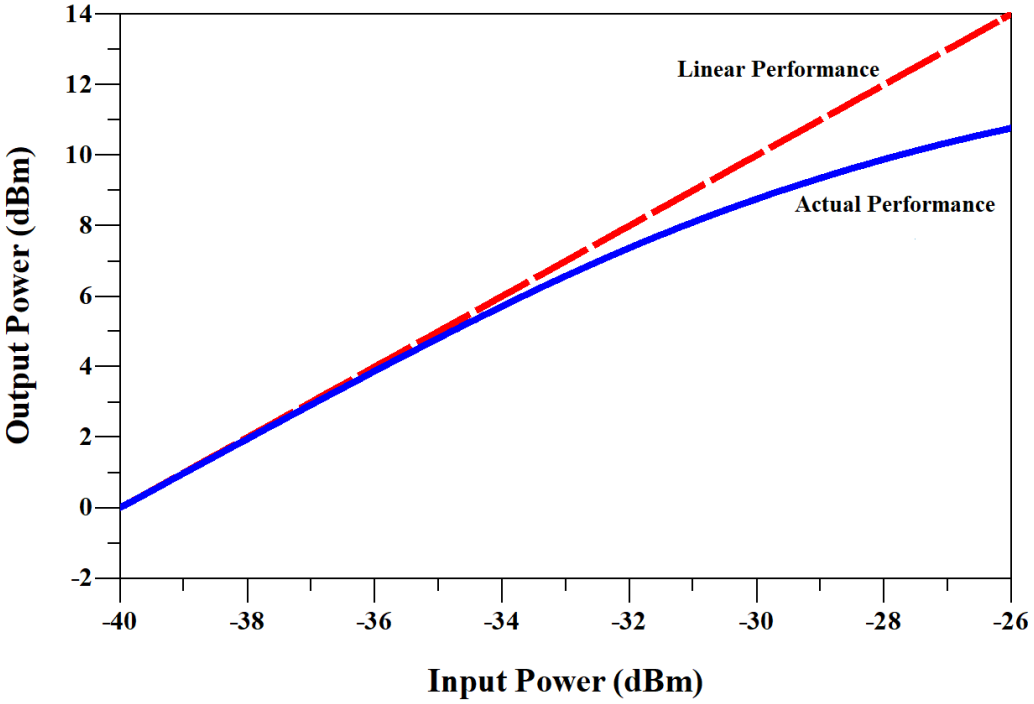

Figure 4.6: Transfer characteristics of designed X-Band LNA at 10GHz

Figure 4.6 shows the transfer characteristics of the designed X-band LNA considering the 1-dB compression point of the LNA. The input and output powers at 1-dB compression points are -30 dBm and 9 dBm at 10 GHz. Beyond these points, the amplifier becomes saturated. Any further increase in the input power leads to no further output power increase. The amplifier response becomes non-linear and produces signal distortion, harmonics, and potentially inter-modulation products beyond this compression point.

Table 4.1: X-Band LNA Requirements and Performance at 10 GHz Design Frequency

Design Parameter	Requirement	Performance
$S_{11}(dB)$	$\leq$ - 10	- 21
$S_{12}(dB)$	$\leq$ - 40	- 60
$S_{21}(dB)$	$\geq$ 25	40
$S_{22}(dB)$	$\leq$ - 10	- 40
NF (dB)	$<$ 2	0.9
K	$>$ 2	5
In-band Ripple (dB)	$\leq$ 3	1

Table 4.2 shows comparison of the designed X-Band LNA with recently reported X-Band LNAs. The rollette stability factor is represented as K, showing that the LNA is stable across the design frequency.

4.1.2 FIS X-Band Receiver Sensitivity Simulation

In order to characterize and analyse the sensitivity response of the reported designed broadband 8-12 GHz pHEMT InGaAs MMIC LNA for FIS LNB, a simulation of the performance metrics for a typical X-band receiver was carried out. The simulation parameters that were applied are thus: CNR (measured) = 17 dB; NF = 0.9 dB (from the presented designed 8-12 GHz MMIC LNA); f_c =

Table 4.2: Comparison of Simulated LNA at X-Band Frequencies

Ref.	Process	No. of MMIC Stages	Freq.(GHz)	Gain (dB)	Noise Figure (dB)	Power (mW)
[71]	0.7 µm GaAs mHEMT	3	7-11	30	1	62.2
[72]	0.65 µm CMOS	2	9.35-10.65	27.8	1.8	4.68
[73]	0.13 µm SiGe BiCMOS	3	6-12	21	1.7	100
[74]	0.65 µm CMOS	2	8-12	15	8.4	110
[75]	0.18 µm CMOS	2	6.4-7.4	12.5	3	19
[76]	0.1 µm GaAs mHEMT	3	4-12	31.5	1.31	8
[77]	0.1 µm InP HEMT	3	0.3-14	40	2.73	12
This Work	0.15 µm InGaAs pHEMT	3	8-12	40	0.9	43

9.8 GHz; satellite channel bandwidth, B = 50 MHz (typical); measured received power, P_r= -33dBm.

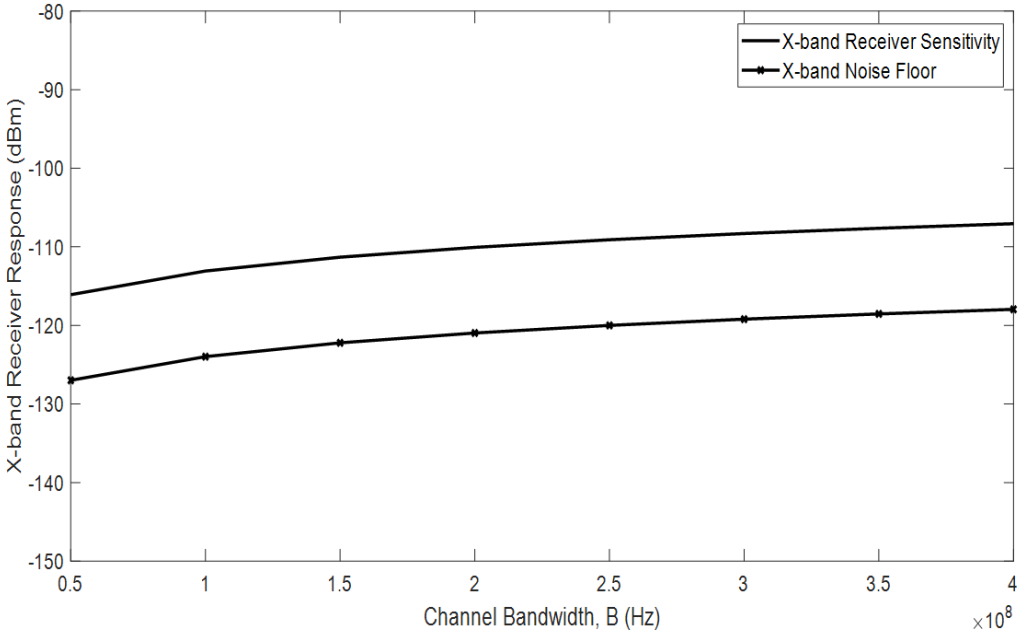

Figure 4.7: Fibre-Integrated Receiver Sensitivity Response

Figure 4.7 illustrates the X-band receiver sensitivity and noise floor responses over the variable channel bandwidths of the fibre LNB. A wideband switchable 5G receiver can adapt the channel bandwidth to the on-demand duplex signal transmission and reception constraints to support an optimal real-time receiver sensitivity threshold.

For a constant channel bandwidth (Fig.4.8), the 50 MHz margin yields the best receiver sensitivity threshold [67] over the X-band operating frequency. This appears to justify the choice of the 50 MHz bandwidth for satellite video signals transmission [3], [90].

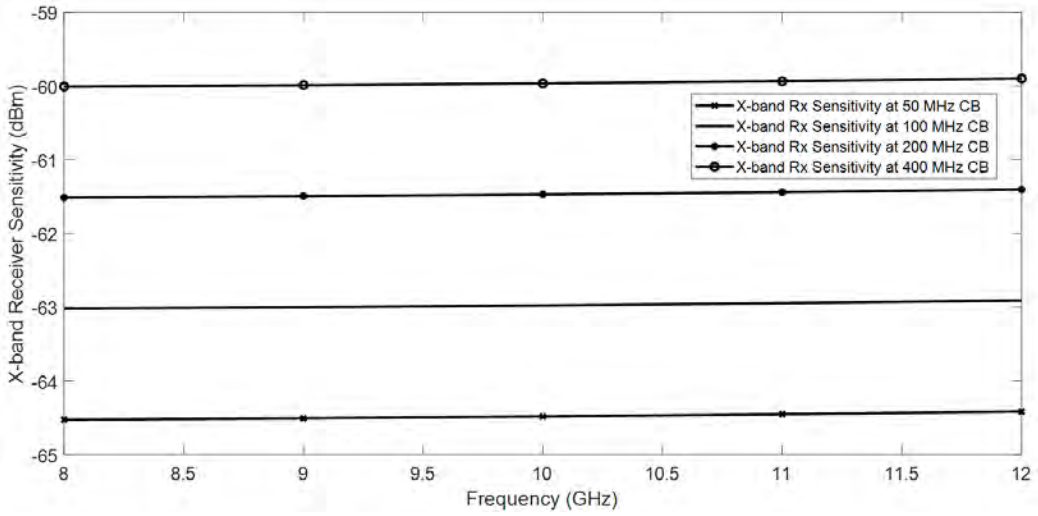

Figure 4.8: X-band Receiver Sensitivity at a Constant Channel Bandwidth

During an MMIC LNA characterisation, the allowable temperature drift is 23±1 °C; some equipment allows for up to 3 °C drift about the ambient temperature. For any given fabricated MMIC LNA that is characterised, 0.1 to 0.2 dB is the allowable loss margin for linear (S-parameters) measurements. A loss of above 1dB is unacceptable. The finding implies a need to enhance the receiver sensitivity by performing a component- to subsystem-levels reconfiguration in near real-time.

Our reported three-stage single-ended X-band MMIC LNA design uses the common-source configuration (CSC) for low-noise performance and moderate bandwidth.

The series LC impedance matching network and circuit design technique enhance the gain, stability.

Parallel feedback in stage three improves the gain flatness of the forward transmission response. This finding further strengthens the need for a switchable wideband receiver to cater for the massive 5G user equipment (UE) and base station operational requirements.

4.2 K/Ka-Band LNA Responses and Discussion

4.2.1 K/Ka-Band LNA analysis

The LNA input and output return losses are shown in Fig. 4.9. It can be observed that the output and input return losses are greater than 10 dB for the entire band, showing the effectiveness of the amplifier's input and output matching networks. The gain (Fig.4.10) is 30 dB with a ripple of 1dB across the required band, while the minimum noise at the resonant frequency of 26 GHz is 1.7 dB (Fig.4.12). The LNA is stable across the entire band up to cut-off frequency as shown in Fig. 4.13, hence unlikely to oscillate at any frequency. Fig.4.15 shows the linearity of the LNA. The input P_{1dB} correspond to -22.3 dBm. Table 4.3 summarises the results of the designed LNA at a design frequency of 26 GHz.

Table 4.4 shows comparison of the designed K/Ka-Band LNA with recently reported K/Ka-Band LNAs.

4.2.2 5G NR FR2 Receiver Sensitivity Simulation

In order to characterise and analyse the sensitivity response of the reported designed broadband 23-24 GHz pHEMT InGaAs MMIC LNA, a simulation of the

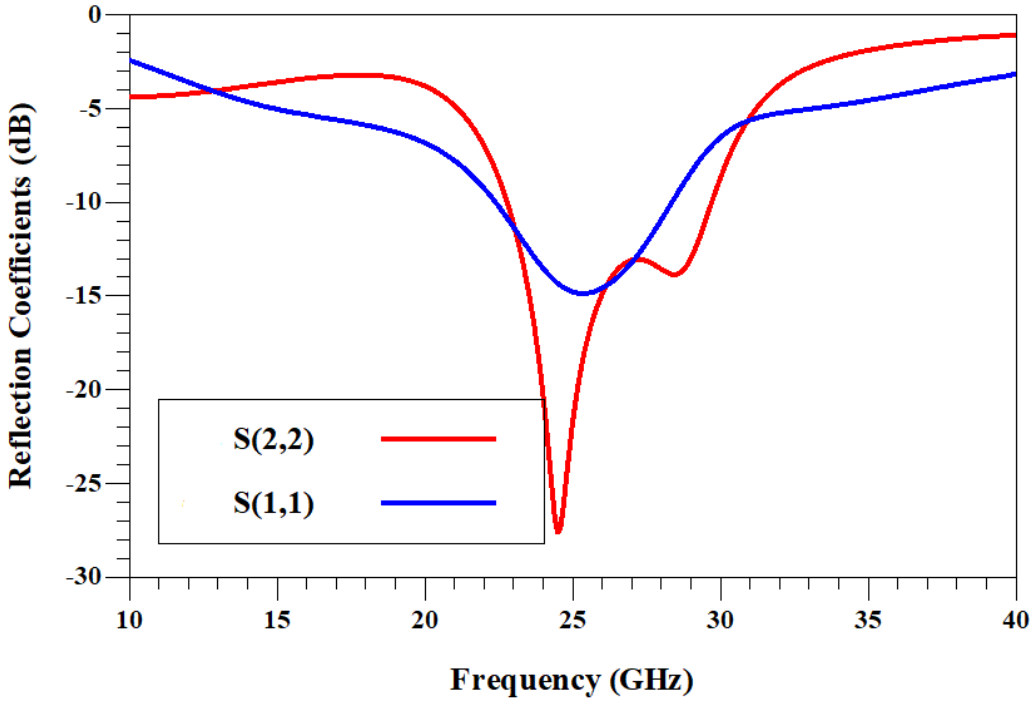

Figure 4.9: Input and Output reflection coefficient of the K/Ka-band MMIC LNA circuit

Table 4.3: K/Ka-Band LNA Requirements and Performance at 25 GHz Design Frequency

Design Parameter	Requirement	Performance
$S_{11}(dB)$	$\leq$ -10	-15
$S_{12}(dB)$	$\leq$ -40	-43
$S_{21}(dB)$	$\geq$ 25	30
$S_{22}(dB)$	$\leq$ -10	-25
NF (dB)	$<$ 2	1.7
K	$>$ 2	2
In-band Ripple (dB)	$\leq$ 3	1

performance metrics for a typical 5G NR FR2 receiver was carried out. The simulation parameters applied in (9) are: CNR = 10 dB; NF = 1.7 dB (from the

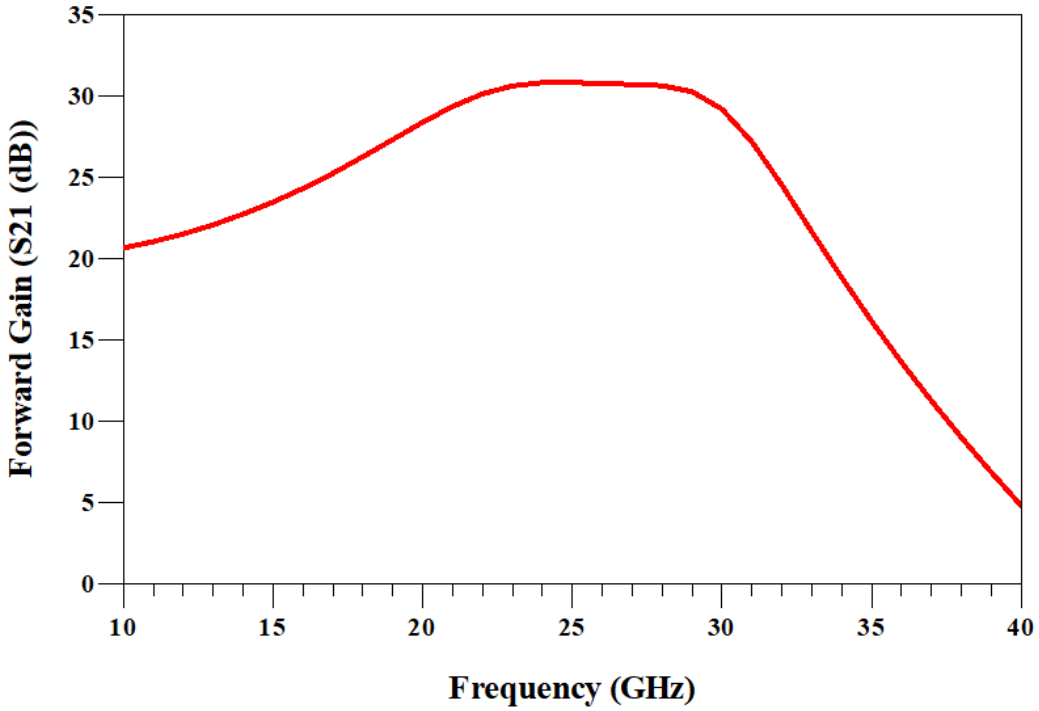

Figure 4.10: Gain of the K/Ka-band MMIC LNA circuit

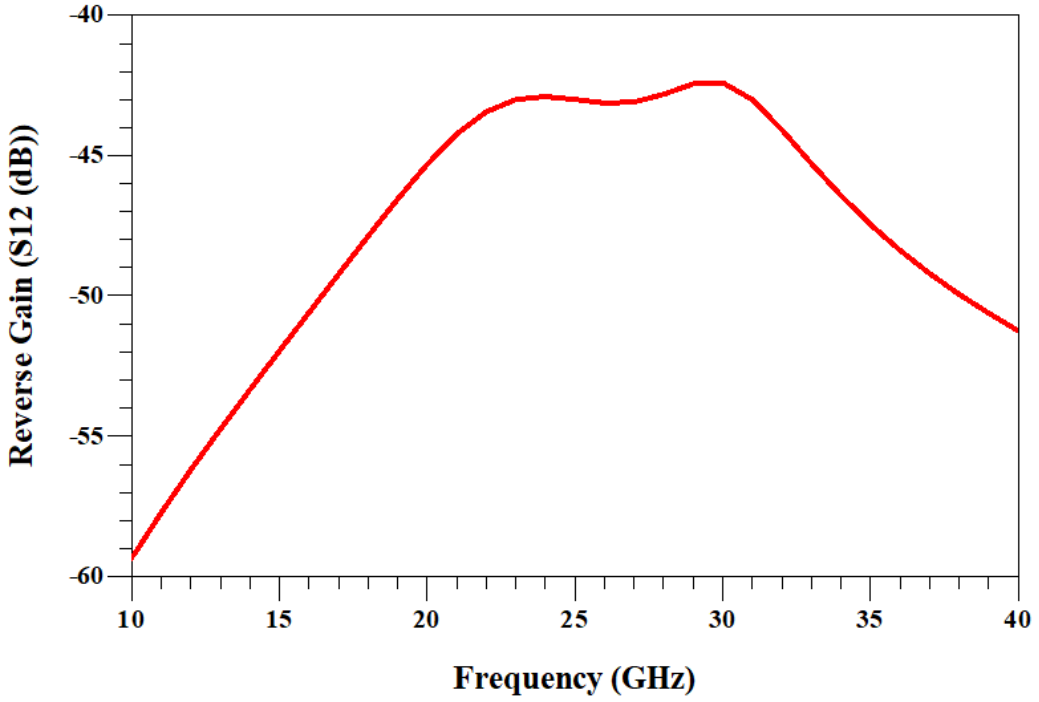

Figure 4.11: Isolation of the K/Ka-band MMIC LNA circuit

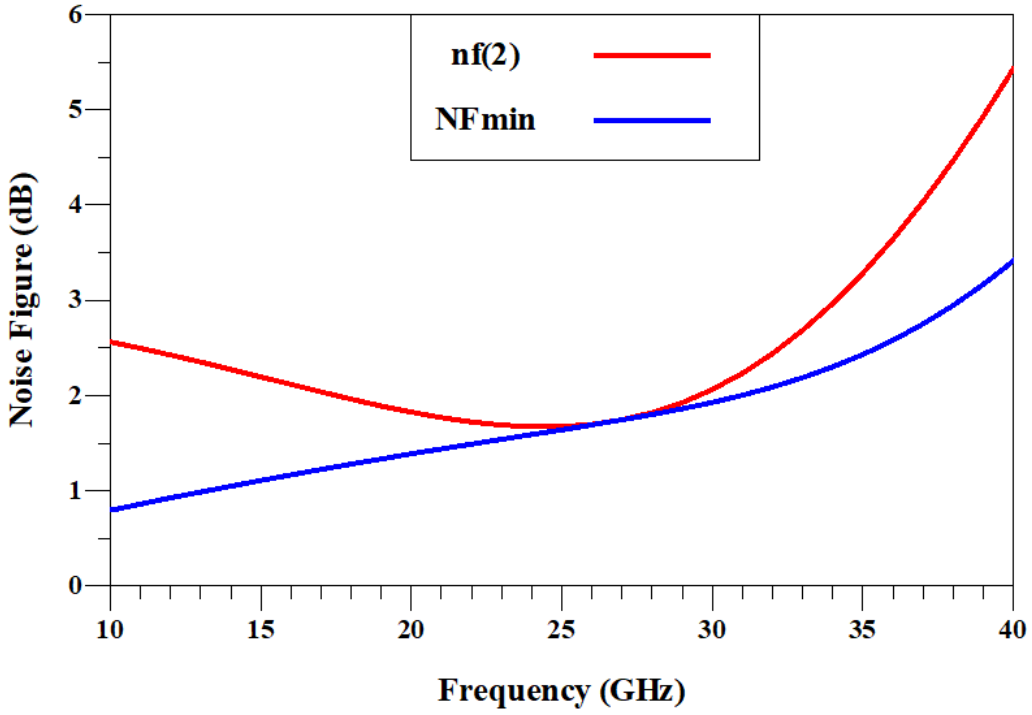

Figure 4.12: Noise Figure of the K/Ka-band MMIC LNA circuit

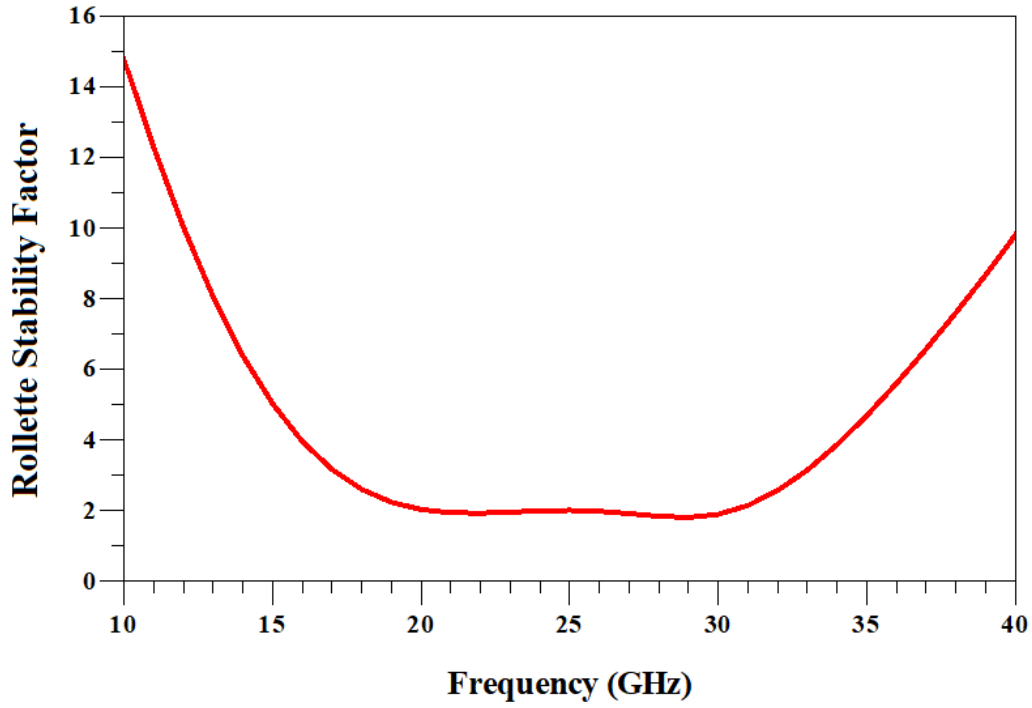

Figure 4.13: Rollette Stability Factor of the K/Ka-band MMIC LNA circuit

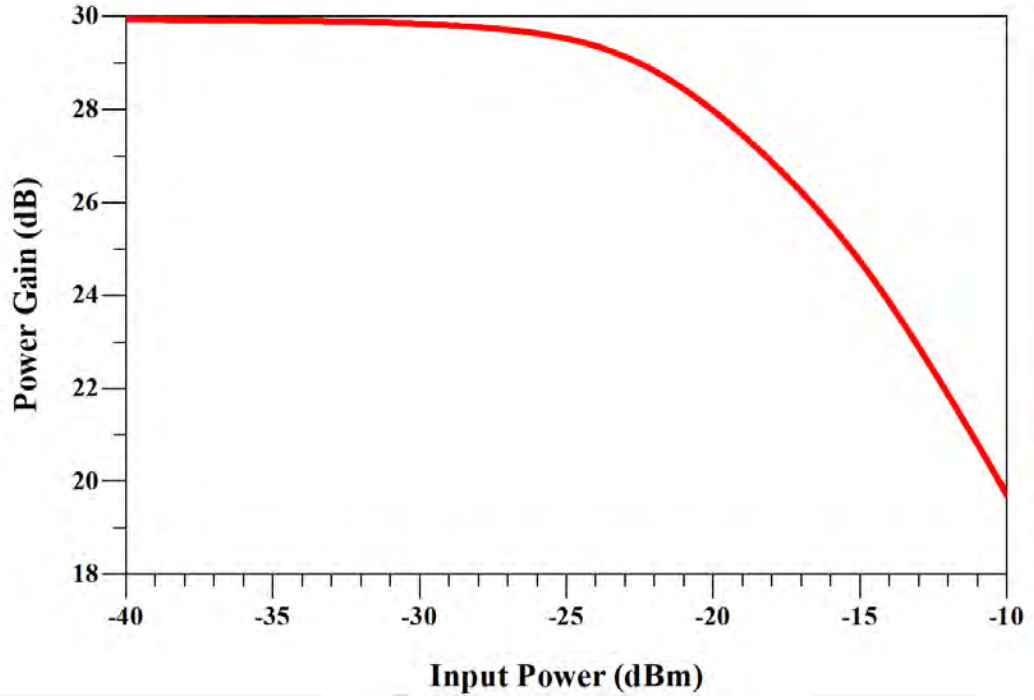

Figure 4.14: Gain Vs Input Power Curve of designed K/Ka-band MMIC LNA

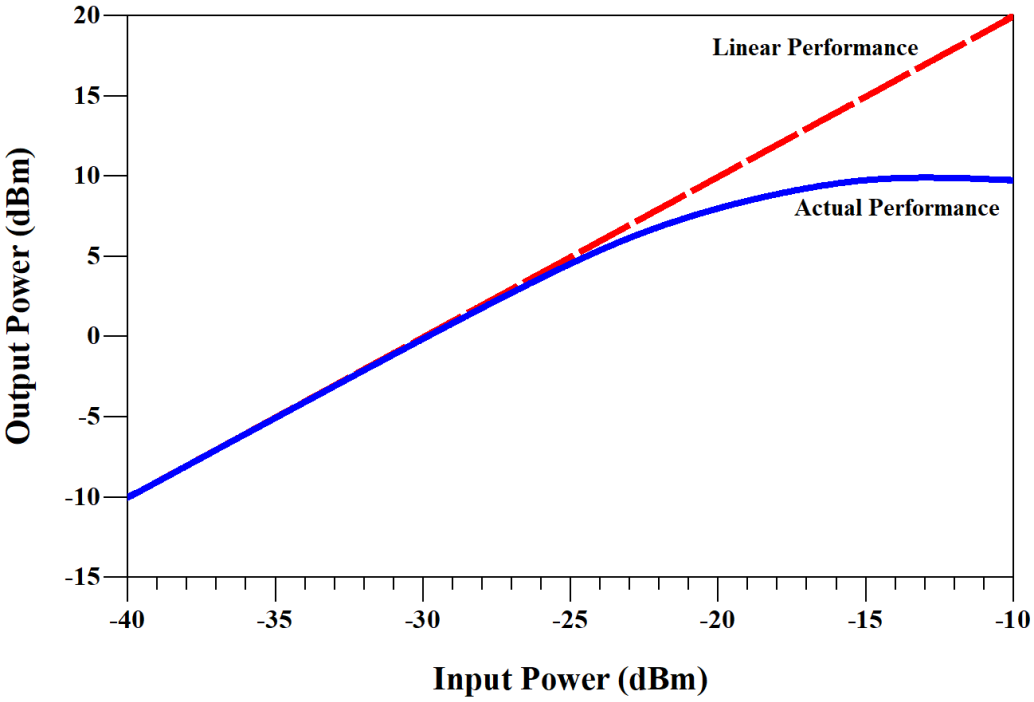

Figure 4.15: Transfer characteristics of designed K/Ka-band MMIC LNA

Table 4.4: Simulation Comparison of Designed LNA at K/Ka-Band Frequencies

Ref.	Process	No. of MMIC Stages	Freq.(GHz)	Gain (dB)	Noise Figure (dB)	Power (mW)
[84]	0.15 µm AlGaAs-InGaAs pHEMT	3	26-33	22.8	1.6	-
[76]	0.1 µm GaAs mHEMT	3	25-34	24.2	3.04	2.8
[77]	0.1 µm InP HEMT	3	16-28	32.3	4.11	3.5
[52]	GaAs pHEMT	3	18-21.6	30.3	1	60
[85]	0.1 µm GaAs pHEMT	3	18-43	21.6	1.8-2.7	140
[86]	0.25 µm SiGe	3	24-34	26.4	3.1-3.5	134
[87]	0.4 µm CMOS	3	26-33	27.1	3.3-4.3	31.4
This Work	0.15 µm InGaAs pHEMT	3	23-28	30.8	1.7	43

presented designed MMIC LNA); and 5G NR FR2 band number: n258. Firstly, the path loss constraints for the receiver was considered for up to the industry-recommended 300 m range for 5G small cells. Fig. 4.16 shows the path-loss response for the 5G NR FR2 band n258 up to 300 m. The upper uplink and downlink bands of the proposed 5G Ka-band frequencies will record at least 20 dB signal attenuation within a 300 m range.

Fig. 4.17 illustrates the 5G NR FR2 receiver sensitivity and noise floor responses over the proposed channel bandwidths of 50 MHz, 100 MHz, 200 MHz and 400 MHz.

Our reported three-stage single-ended MMIC LNA design using the pHEMT process technology utilises the common-source configuration to achieve gain flatness and stability (up to the cut-off frequency of the active semiconductor device) with parallel feedback in stage three. In Fig. 4.18, a 5G NR FR2 receiver sensitivity differential response is presented. The response shows that the lower the 5G

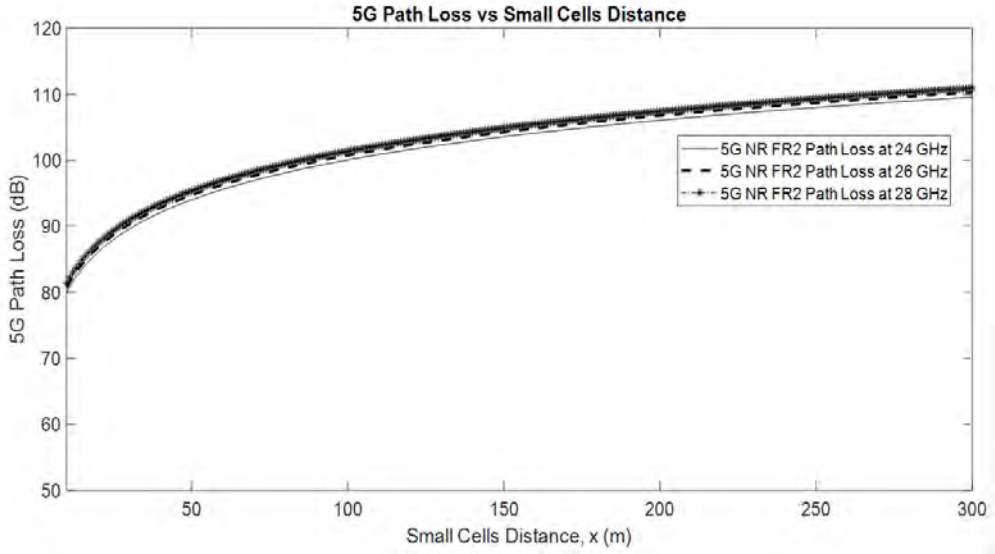

Figure 4.16: 5G NR FR2 Path Loss versus Small Cells Distance

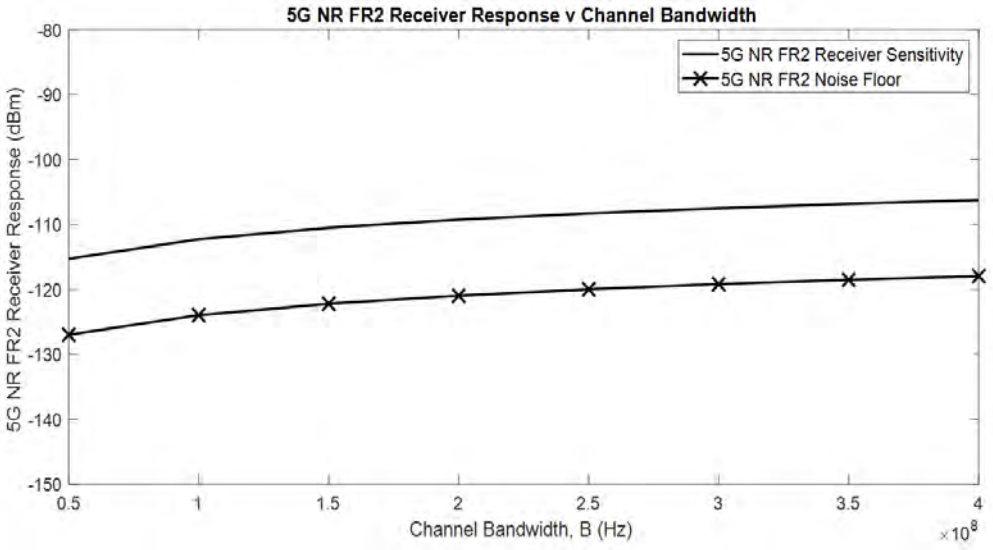

Figure 4.17: 5G NR FR2 Receiver Sensitivity Response

channel bandwidth, the steeper the sensitivity gradient of the pHEMT MMIC LNA device. For the reported design, the 5G n258 band gradient over 50 MHz to 100 MHz is 0.04 µs; while 200 MHz to 400 MHz yields 0.01 µs. Hence, receiver sensitivity reduces with channel bandwidth, but narrowband resolutions imply considerable in-band sensitivity differential swings. This finding further strengthens the need for a switchable wideband receiver to cater for the massive

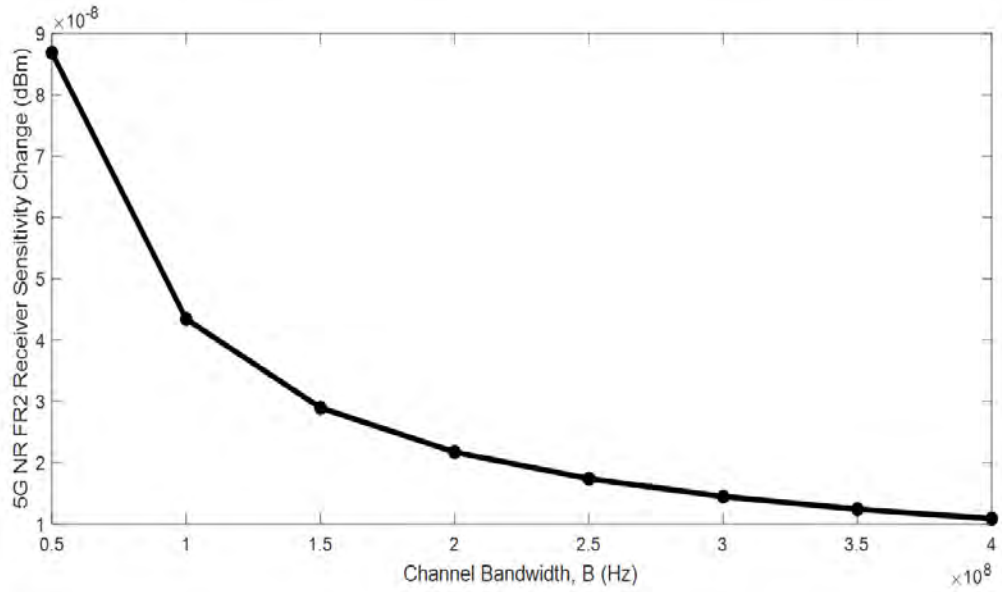

Figure 4.18: 5G NR FR2 Receiver Sensitivity Differential Response

5G UE and base station transceivers operational requirements.

4.2.3 SPDT Result Analysis

The switch is designed to operate at the frequency range of DC - 50 GHz with less than 3dB insertion loss and an input and output return loss less than 10 dB (Fig 4.19) as well as more than 40 dB isolation (Fig 4.20), for X-band and Ka-band frequency applications.

Table 4.5 shows the SPDT Switch Design Requirements and Performance at 10 GHz and 26 GHz frequencies.

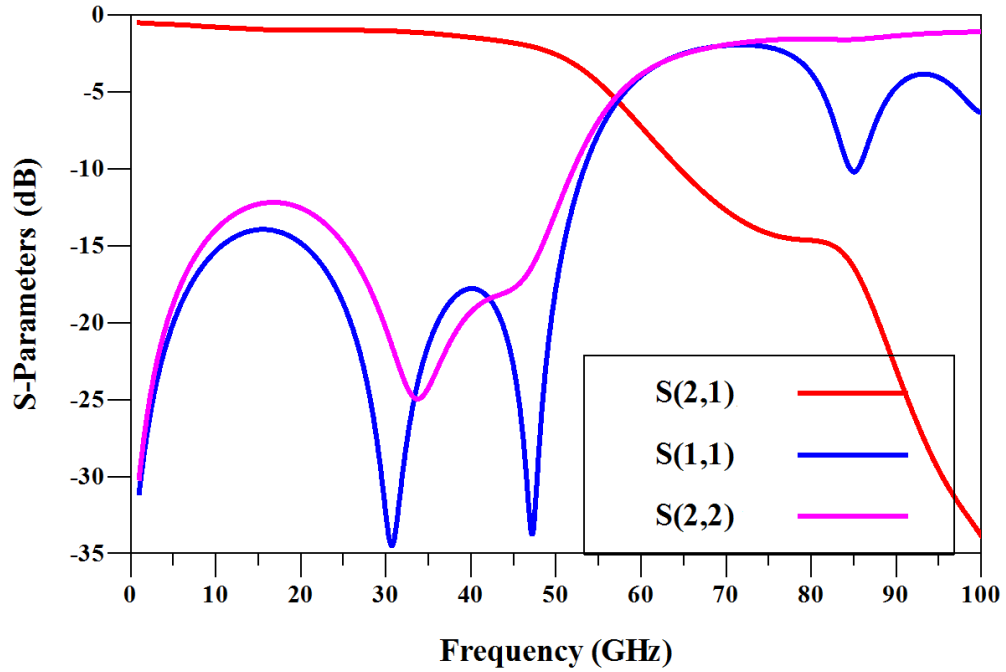

Figure 4.19: Insertion loss (Red), Input (Blue) and Output (Pink) return loss of distributed SPDT Switch

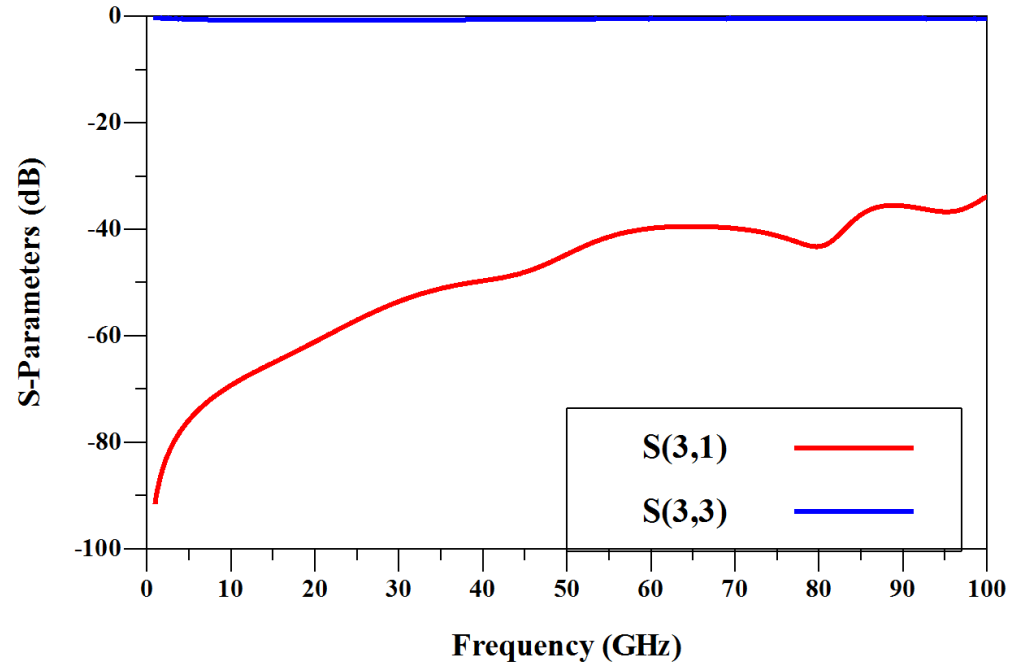

Figure 4.20: Isolation loss of the SPDT Switch

Table 4.5: Wideband SPDT Switch Design Requirements and Performance at 10 GHz and 26 GHz frequencies.

Design Parameter	Requirement	10 GHz	26 GHz
$S_{11}(dB)$	$\leq$ -10	-15	-21
$S_{21}(dB)$	$\geq$ -3	-0.8	-1
$S_{22}(dB)$	$\leq$ -10	-14	-16
$S_{31}(dB)$	$\leq$ -40	-69	-56
$S_{33}(dB)$	$\leq$ -1	-0.8	-0.8

4.3 Switchable Wideband LNA performance with SPDT Integration

Switchable capability is achieved using an integrated single-pole double-throw switch (SPDT) with the designed wideband LNAs (Fig. 3.2). The SPDT switch configures the path through the phase-shifting elements to produce the desired insertion phase shift. The SPDT employs two SPST (single pole single throw) switches as shown in Fig. 3.13 to switch the signals between the X-band and K/Ka-band frequency arms. One of the challenges in designing the reconfigurable network with the SPDT is to ensure the impedance matching for both of its states is optimal to reduce the insertion loss of the circuit. Large resistors are used to bias the source and drain terminals (V1 and V2) of the series switch (Fig. 3.13) to provide less insertion loss. The drain voltages states are shown in Table 4.6.

Table 4.6: Drain voltages states for switchable wideband receiver front-end with SPDT

Band	V_{d2}	V_{d3}	SPDT On-State	Switch Off-state
X-band	0 V	2 V	-1.5 V	0 V
K/Ka-band	2 V	0 V	0 V	-1.5 V

4.3.1 SPDT Integration with X-band ON and K/Ka-band OFF

The simulated gain of the switchable wideband receiver front-end with X-band ON and K/Ka-band OFF is shown in Fig. 4.21. The simulation shows a gain between 23 dB and 27 dB over the frequency range of 8 GHz to 12 GHz at room temperature while the K/Ka-band is switched off.

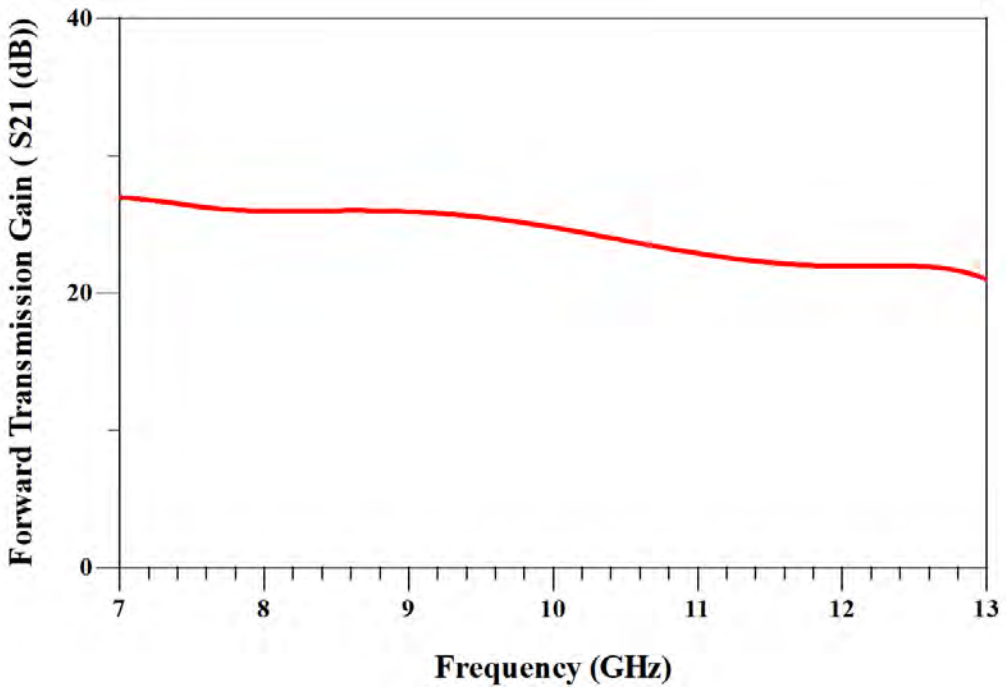

Figure 4.21: Gain performance of the switchable wideband receiver front-end with the X-band arm ON and K/Ka-band OFF

The noise performance of the switchable wideband receiver front-end with X-band ON and K/Ka-band OFF is shown in Fig. 4.22. For the X-band arm, the noise figure is below 10 dB for the band of interest. Since the K/Ka-band arm is off, there is a high resistance to current flow in that arm, which reduces the gain.

From Fig. 4.23, the input and output reflection coefficients are better than -5 dB over the X-band frequency band.

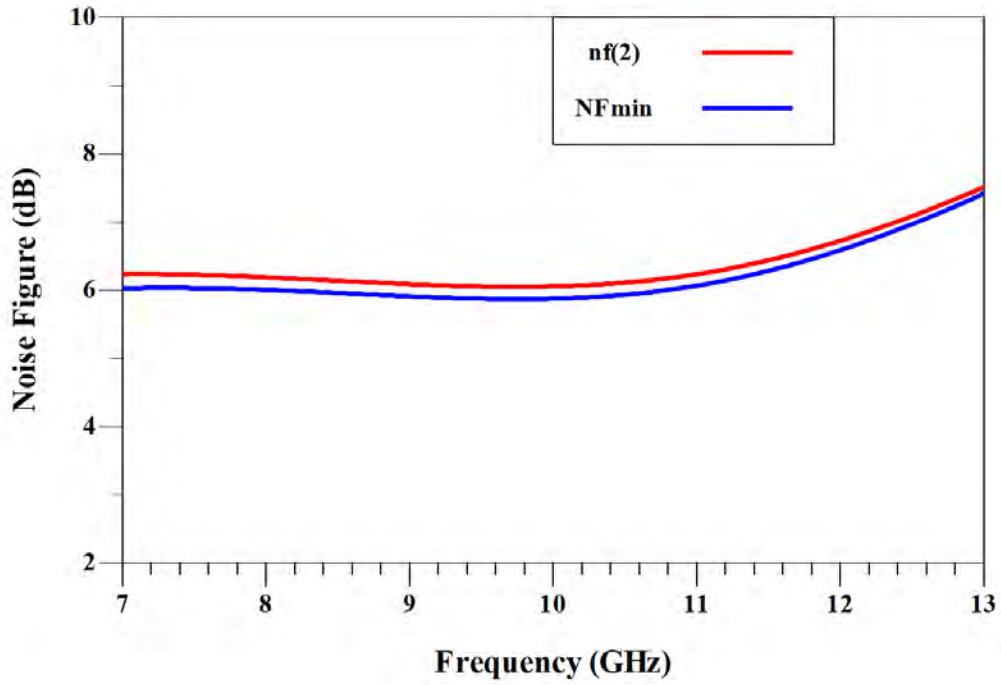

Figure 4.22: Noise performance of the switchable wideband receiver front-end with the X-band arm ON and K/Ka-band OFF

The stability performance of the reconfigurable receiver front-end with the X-band arm ON and K/Ka-band OFF is unconditionally stable across all frequencies as shown in Fig. 4.24.

4.3.2 SPDT Integration with X-band OFF and K/Ka-band ON

The simulated gain of the switchable wideband receiver front-end with X-band OFF and K/Ka-band ON is shown in Fig. 4.25. The simulation shows a gain between 23 dB to 27 dB over the frequency range of 23 GHz to 28 GHz at room temperature while the X-band is switched off.

The noise performance of the switchable wideband receiver front-end with X-band OFF and K/Ka-band ON is shown in Fig. 4.26. For the K/Ka-band arm, the noise figure spans 2.3 dB to 2.6 dB for the band of interest.

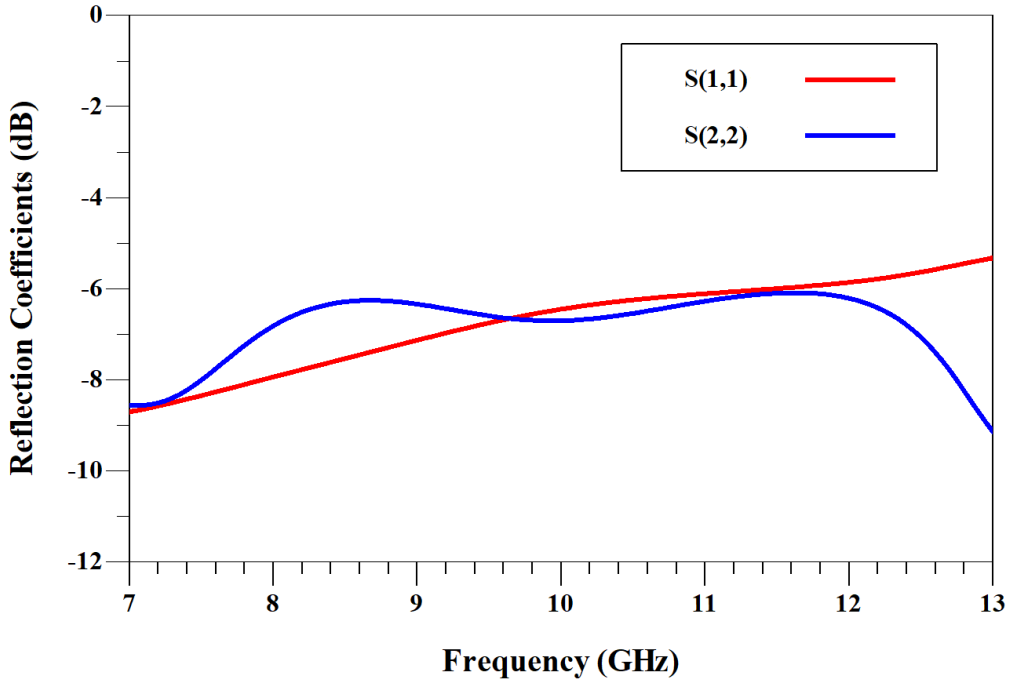

Figure 4.23: Input and output reflection coefficient performance of the switchable wideband receiver front-end with the X-band arm ON and K/Ka-band OFF

From Fig. 4.27, the input and output reflection coefficients are better than -5 dB over the K/Ka-band frequency band.

The stability performance of the switchable wideband receiver front-end with the X-band arm OFF and K/Ka-band ON is unconditionally stable across all frequencies as shown in Fig. 4.28.

4.4 Chapter Summary

This chapter discussed the simulation results for the proposed highly adaptive reconfigurable receiver frontend (HARRF). The responses of the two designed LNAs are analysed individually and after that, the integrated responses are analysed. The stand-alone X-band LNA gives a flat gain of approximately 40 dB across the band of interest while the stand-alone K/Ka-band gives a flat gain

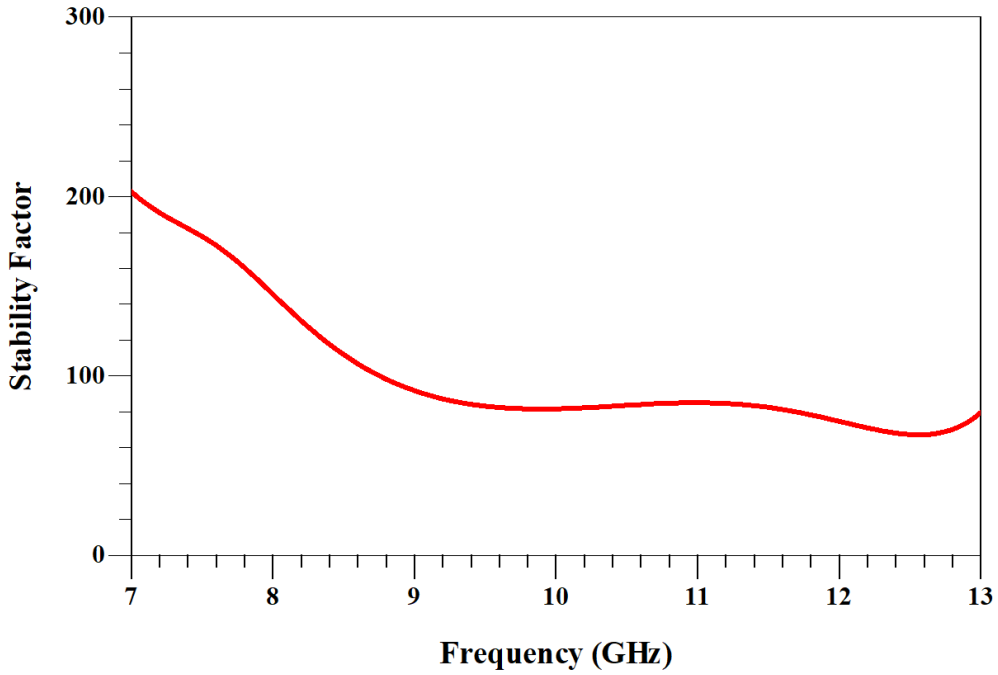

Figure 4.24: Stability performance of the switchable wideband receiver front-end with the X-band arm ON and K/Ka-band OFF

of approximately 30 dB. The integrated architecture (HARRF), gives a gain of 20-28 dB when the X-band is ON and K/Ka-band OFF. A gain of 23 -27 dB is achieved when the X-band arm is OFF and the K/Ka-band arm is ON.

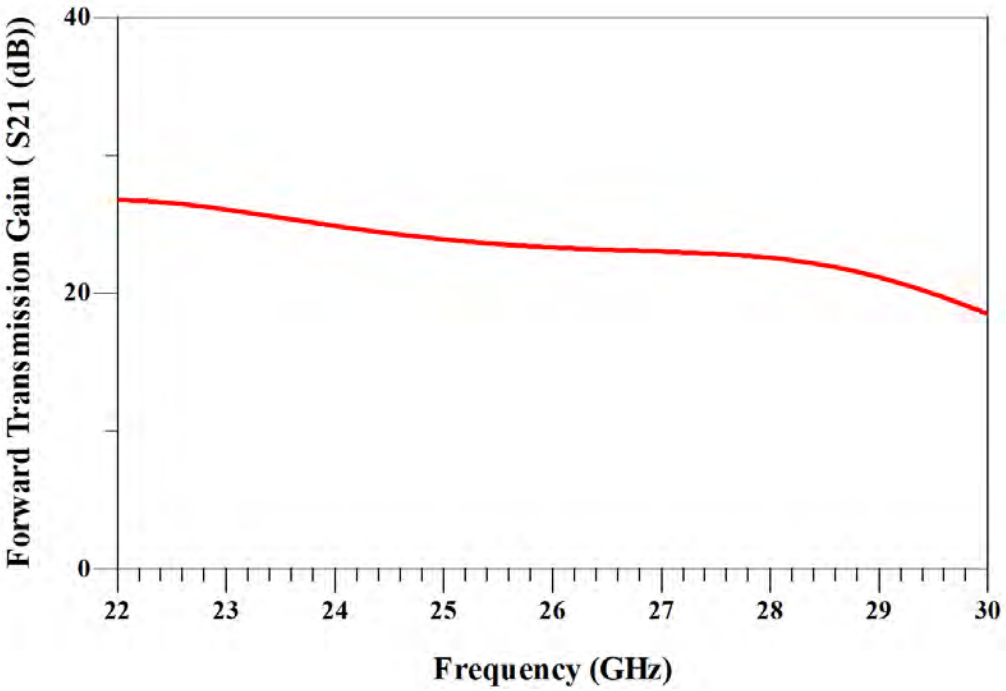

Figure 4.25: Gain performance of the switchable wideband receiver front-end with the X-band arm OFF and K/Ka-band ON

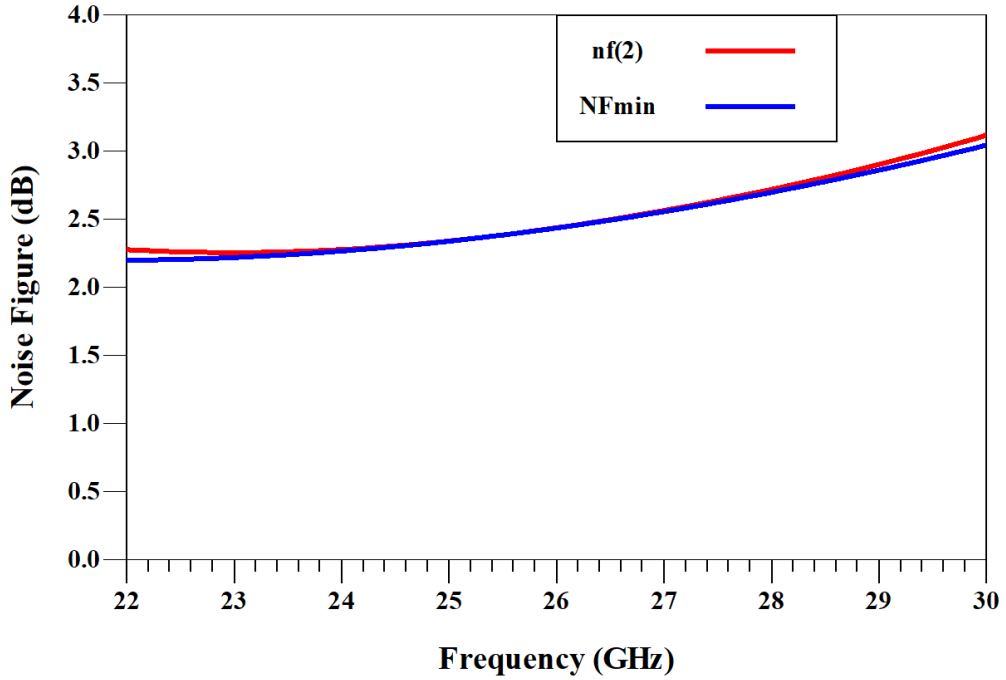

Figure 4.26: Noise performance of the switchable wideband receiver front-end with the X-band arm OFF and K/Ka-band ON

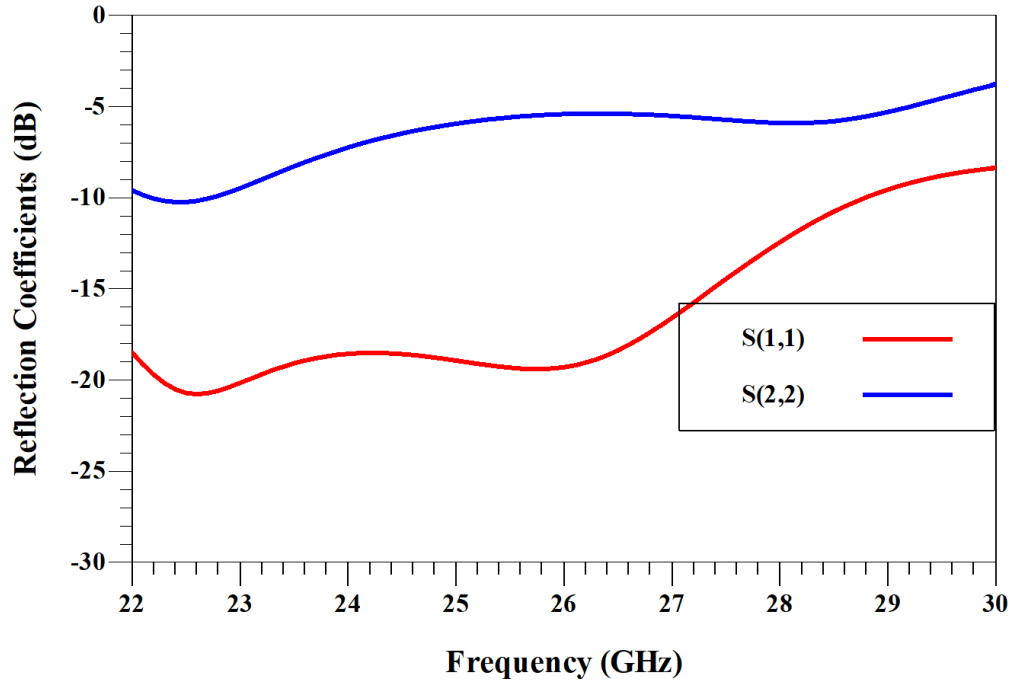

Figure 4.27: Input and output reflection coefficient performance of the switchable wideband receiver front-end with the X-band arm OFF and K/Ka-band ON

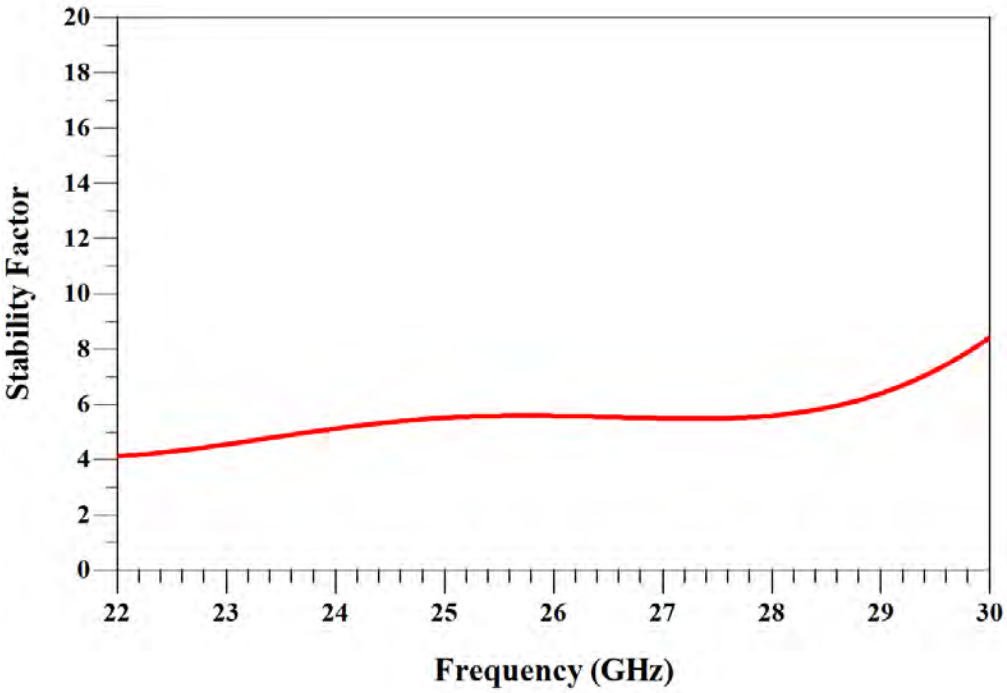

Figure 4.28: Stability performance of the switchable wideband receiver front-end with the X-band arm OFF and K/Ka-band ON

Chapter 5

Conclusions and Future Work

This chapter summarises the main contributions of this thesis exploring the use of a single-pole, double throw RF switch to switch between two designed wideband low noise amplifier over 8-12 GHz range and 23-28 GHz frequency range.

5.1 Summary

This thesis proposes a highly adaptive reconfigurable receiver frontend (HARRF) for use in 5G and satellite application. The main contributions of this research are summarised as follows:

- In chapter 2, the motivation for this research is discussed. **State-of-the-art wideband switchable LNA architectures** is investigated, capturing existing wideband topologies. Existing switchable topologies are outlined and carefully analysed to derive the best architecture and hardware composition for the proposed highly adaptive reconfigurable receiver front-end (HARRF). Frequency specification is carried out for multi-standard applications for X and K/Ka band frequencies. Furthermore, design specification for stand-alone wideband LNAs are carried out for X and K/Ka-band

frequencies. The LNAs are designed using a scalable PL15-10 0.15 µm low noise InGaAs pseudomorphic high electron mobility transistor process technology provided by WIN Semiconductors.

- In chapter 3, a **Design Methodology for HARRF** is proposed for effective and efficient frequency reconfiguration between the X and K/Ka-band. Two LNAs are designed for adaptive hardware switching between the X and K/Ka frequencies bands. The two broadband monolithic microwave integrated circuit (MMIC) are designed using 0.15 µm gate length Indium Gallium Arsenide (InGaAs) pseudomorphic high electron transistor (pHEMT) technology from WIN Semiconductor Corp, Taiwan.

  The three-stage X-band (8-12 GHz) LNA, using the common-source cascaded topology, demonstrates an industry-leading in-band gain response of 40 dB, a noise figure of 1.0 dB and very low power dissipation of 43 mW. For a constant bandwidth receiver, the sensitivity changes by approximately 1.5 dB over the operating satellite signal frequency. Similarly, for a variable bandwidth receiver, the sensitivity changes by approximately 1.5 dB over the channel bandwidth. Moreover, the sensitivity margin of the designed LNA is 40 dB, and this holds a great promise for real-time component-level reconfiguration applications.

  The designed three-stage K/Ka-band (23-28 GHz) LNA demonstrates an industry-leading flat gain response of 30 dB, a noise figure of 1.70 dB and a very low power dissipation of 43 mW. The differential sensitivity response spans 0.01 to 0.04 dBm/Hz over the upper and lower ends of the channel bandwidths of the 5G New Release frequency range n258 band (24.25-27.58 GHz). The designed LNA is suitable for real-time component-level reconfiguration applications. These applications include dynamic spectrum access, regenerative wireless transponder-transceiver technologies support, active spectrum resource usage, distributed sensing over a multi-

standards wideband spectrum, and massive and complex time-varying spectrum datasets/features.

- A **Single pole double throw switch** for broadband application is designed to operate at the frequency range of DC-50 GHz. The device exhibited a less than 3 dB insertion loss and more than 40 dB isolation. The SPDT switch is designed with wideband capabilities for X-band and K/Ka-band frequency range. This designed switch forms the switching arms between the two designed LNAs for X and K/Ka-band applications.

- A **Highly Adaptive Reconfigurable Receiver Front-end (HARRF)** for broadband application is achieved by integrating the SPDT with the two LNAs. A gain of 25 dB is achieved at the centre frequency of 9.8 GHz when the X-band arm is turned on, and the K/Ka-band is turned off. A gain of about 23 dB is achieved at 25.4 GHz when the K/Ka-band arm is turned on and the X-band arm is off.

5.2 Limitations and Future Work

The limitations faced during the research work were:

- **Access to fabrication services**: Due to the unavailability of lab equipment for fabrication and restrictions due to COVID, this research findings are solely simulation based compared with known industry standard literatures. Thus, the designed HARRF and the LNAs circuits could not be fabricated to verify the proposed wideband switchable receiver frontend concept.

- **Switchable transmitter frontend design**: A switchable wideband receiver frontend has been the focus of this thesis. An extension of this work

will be to consider the transmitter end design, response and overall performance of the transceiver system.

- **Process technology used**: This thesis was carried using a 0.15 µm gate length Indium Gallium Arsenide (InGaAs) pseudomorphic high electron transistor (pHEMT) technology. Exploring other available transistor technologies for comparative analysis with the designed switchable wideband receiver frontend is another research future work. This will lead to developing improved FET models with minimal parasitic effects for the switchable wideband receiver frontend. Furthermore, mathematical modelling of matching network and noise analysis of HARRF can be derived.

Bibliography

[1] A. Alhamed, O. Kazan, G. Gultepe, and G. M. Rebeiz, "A Multi-band/Multistandard 15-57 GHz Receive Phased-Array Module Based on 4 x 1 Beamformer IC and Supporting 5G NR FR2 Operation," *IEEE Transactions on Microwave Theory and Techniques*, pp. 1–1, 2022.

[2] V. Bhagavatula, "Exploring Multimode Cellular Transceiver Design: A Short Tutorial," *IEEE Solid-State Circuits Magazine*, vol. 13, no. 1, pp. 35–47, 2021.

[3] M. Uko and S. Ekpo, "8-12 GHz pHEMT MMIC Low-Noise Amplifier for 5G and Fiber-Integrated Satellite Applications," *International Review of Aerospace Engineering (IREASE)*, vol. 13, no. 3, p. 99, 2020.

[4] Y. Kyung, S. Park, and J. Park, "SDN/NFV-based scalable mobile service integration for gradual network evolution," *Journal of Communications and Networks*, vol. 19, no. 6, pp. 569–576, 2017.

[5] H. Campanella, Y. Qian, C. O. Romero, J. S. Wong, J. Giner, and R. Kumar, "Monolithic Multiband MEMS RF Front-End Module for 5G Mobile," *Journal of Microelectromechanical Systems*, vol. 30, no. 1, pp. 72–80, 2021.

[6] L. Nadeem, M. A. Azam, Y. Amin, M. A. Al-Ghamdi, K. K. Chai, M. F. N. Khan, and M. A. Khan, "Integration of D2D, Network Slicing, and MEC

in 5G Cellular Networks: Survey and Challenges," *IEEE Access*, vol. 9, pp. 37590–37612, 2021.

[7] N. Kumar, M. Rawat, and K. Rawat, "Software-Defined Radio Transceiver Design Using FPGA-Based System-on-Chip Embedded Platform With Adaptive Digital Predistortion," *IEEE Access*, vol. 8, pp. 214882–214893, 2020.

[8] A. A. Nawaz, J. D. Albrecht, and A. Çagri Ulusoy, "A 28-/60-ghz band-switchable bidirectional amplifier for reconfigurable mm-wave transceivers," *IEEE Transactions on Microwave Theory and Techniques*, vol. 68, no. 7, pp. 3197–3205, 2020.

[9] Cisco, "Cisco Annual Internet Report - Cisco Annual Internet Report (2018-2023) White Paper," 2022. https://www.cisco.com/c/en/us/solutions/collateral/executive-perspectives/annual-internet-report/white-paper-c11-741490.html.

[10] T. S. Rappaport, Y. Xing, G. R. MacCartney, A. F. Molisch, E. Mellios, and J. Zhang, "Overview of Millimeter Wave Communications for Fifth-Generation (5G) Wireless Networks—With a Focus on Propagation Models," *IEEE Transactions on Antennas and Propagation*, vol. 65, no. 12, pp. 6213–6230, 2017.

[11] J. Choi, D. Choi, J. Lee, W. Hwang, and W. Hong, "Adaptive 5G Architecture for a mmWave Antenna Front-End Package Consisting of Tunable Matching Network and Surface-Mount Technology," *IEEE Transactions on Components, Packaging and Manufacturing Technology*, vol. 10, no. 12, pp. 2037–2046, 2020.

[12] I. Leyva-Mayorga, B. Soret, M. Roper, D. Wubben, B. Matthiesen, A. Dekorsy, and P. Popovski, "LEO Small-Satellite Constellations for 5G and

Beyond-5G Communications," *IEEE Access*, vol. 8, pp. 184955–184964, 2020.

[13] S. C. Ekpo and D. George, "Impact of Noise Figure on a Satellite Link Performance," *IEEE Communications Letters*, vol. 15, no. 9, pp. 977–979, 2011.

[14] S. K. Sharma, I. Woungang, A. Anpalagan, and S. Chatzinotas, "Toward Tactile Internet in Beyond 5G Era: Recent Advances, Current Issues, and Future Directions," *IEEE Access*, vol. 8, pp. 56948–56991, 2020.

[15] S. C. Ekpo and D. George, "A System Engineering Analysis of Highly Adaptive Small Satellites," *IEEE Systems Journal*, vol. 7, no. 4, pp. 642–648, 2013.

[16] S. Ekpo and D. George, "4-8 GHz LNA design for a Highly Adaptive Small Satellite Transponder using InGaAs pHEMT Technology," in *2010 IEEE 11th Annual Wireless and Microwave Technology Conference (WAMICON)*, pp. 1–4, April 2010.

[17] S. C. Ekpo, "Parametric System Engineering Analysis of Capability-Based Small Satellite Missions," *IEEE Systems Journal*, vol. 13, no. 3, pp. 3546–3555, 2019.

[18] F. Boccardi, R. W. Heath, A. Lozano, T. L. Marzetta, and P. Popovski, "Five disruptive technology directions for 5G," *IEEE Communications Magazine*, vol. 52, pp. 74–80, February 2014.

[19] R. K. Saha, "Spectrum Sharing in Satellite-Mobile Multisystem Using 3D In-Building Small Cells for High Spectral and Energy Efficiencies in 5G and Beyond Era," *IEEE Access*, vol. 7, pp. 43846–43868, 2019.

[20] U. Paul, J. Liu, S. Troia, O. Falowo, and G. Maier, "Traffic-profile and machine learning based regional data center design and operation for 5G

network," *Journal of Communications and Networks*, vol. 21, no. 6, pp. 569–583, 2019.

[21] S. Seth, D. H. Kwon, S. Venugopalan, S. W. Son, Y. Zuo, V. Bhagavatula, J. Lim, D. Oh, and T. B. Cho, "A Dynamically Biased Multiband 2G/3G/4G Cellular Transmitter in 28 nm CMOS," *IEEE Journal of Solid-State Circuits*, vol. 51, no. 5, pp. 1096–1108, 2016.

[22] H. Darabi, A. Mirzaei, and M. Mikhemar, "Highly Integrated and Tunable RF Front Ends for Reconfigurable Multiband Transceivers: A Tutorial," *IEEE Transactions on Circuits and Systems I: Regular Papers*, vol. 58, pp. 2038–2050, Sept 2011.

[23] F. Laghezza, F. Scotti, P. Ghelfi, and A. Bogoni, "Photonics-Assisted Multiband RF Transceiver for Wireless Communications," *Journal of Lightwave Technology*, vol. 32, pp. 2896–2904, Aug 2014.

[24] R. M. Borges, T. N. Rodovalho, and A. C. S. Junior, "Reconfigurable multiband radio-frequency transceiver based on photonics technology for future optical wireless communications," *IET Optoelectronics*, vol. 9, no. 5, pp. 257–262, 2015.

[25] Y. Huang, W. Li, S. Hu, R. Xie, X. Li, J. Fu, Y. Sun, Y. Pan, H. Chen, C. Jiang, J. Liu, Q. Chen, D. Qiu, Y. Qin, Z. Hong, and X. Zeng, "A High-Linearity WCDMA/GSM Reconfigurable Transceiver in 0.13-μmCMOS," *IEEE Transactions on Microwave Theory and Techniques*, vol. 61, pp. 204–217, Jan 2013.

[26] J. Li, W. Chen, F. Huang, and Z. Feng, "Multiband and Multimode Concurrent PA With Novel Intermodulation Tuning Network for Linearity Improvement," *IEEE Microwave and Wireless Components Letters*, vol. 28, pp. 248–250, March 2018.

[27] H. Cho, C. Lai, T. K. Shih, and H. Chao, "Integration of SDR and SDN for 5G," *IEEE Access*, vol. 2, pp. 1196–1204, 2014.

[28] B. A. A. Nunes, M. Mendonca, X. Nguyen, K. Obraczka, and T. Turletti, "A Survey of Software-Defined Networking: Past, Present, and Future of Programmable Networks," *IEEE Communications Surveys Tutorials*, vol. 16, pp. 1617–1634, Third 2014.

[29] S. K. Tayyaba and M. A. Shah, "5G cellular network integration with SDN: Challenges, Issues and Beyond," in *2017 International Conference on Communication, Computing and Digital Systems (C-CODE)*, pp. 48–53, March 2017.

[30] P. Bouca, R. Figueiredo, J. N. Matos, P. M. Vilarinho, and N. B. Carvalho, "Reconfigurable three functional dimension single and dual-band sdr frontends using thin film bst-based varactors," *IEEE Access*, vol. 10, pp. 4125–4136, 2022.

[31] Y. Sun, B. Chi, and H. Zhang, "Guest Editorial for the Special Issue on Software-Defined Radio Transceivers and Circuits for 5G Wireless Communications," *IEEE Transactions on Circuits and Systems II: Express Briefs*, vol. 63, pp. 1–3, Jan 2016.

[32] E. González-Rodríguez, H. Maune, L. Shen, I. A. Shah, D. Dahlhaus, K. Hofmann, and R. Jakoby, "Reconfigurable Radio Frontends for Cooperative Sensor Networks: Tasks and Challenges," in *2013 IEEE 14th Workshop on Signal Processing Advances in Wireless Communications (SPAWC)*, pp. 515–519, June 2013.

[33] G. Gielen and E. Goris, "Reconfigurable Front-end Architectures and A/D Converters for Flexible Wireless Transceivers for 4G Radios," in *2005 IEEE*

7th CAS Symposium on Emerging Technologies: Circuits and Systems for 4G Mobile Wireless Communications, pp. 13–18, June 2005.

[34] J. Browne, "What's the Difference Between GaN and GaAs?." https://www.mwrf.com/materials/what-s-difference-between-gan-and-gaas.

[35] K. J. Chen, O. Häberlen, A. Lidow, C. l. Tsai, T. Ueda, Y. Uemoto, and Y. Wu, "GaN-on-Si Power Technology: Devices and Applications," *IEEE Transactions on Electron Devices*, vol. 64, pp. 779–795, March 2017.

[36] G. Tang, A. M. H. Kwan, R. K. Y. Wong, J. Lei, R. Y. Su, F. W. Yao, Y. M. Lin, J. L. Yu, T. Tsai, H. C. Tuan, A. Kalnitsky, and K. J. Chen, "Digital Integrated Circuits on an E-Mode GaN Power HEMT Platform," *IEEE Electron Device Letters*, vol. 38, pp. 1282–1285, Sept 2017.

[37] J. Zhu, L. Chen, J. Jiang, X. Lu, L. Yang, B. Hou, M. Liao, Y. Zhou, X. Ma, and Y. Hao, "Ferroelectric Gate AlGaN/GaN E-Mode HEMTs With High Transport and Sub-Threshold Performance," *IEEE Electron Device Letters*, vol. 39, pp. 79–82, Jan 2018.

[38] S. Mondal and J. Paramesh, "A Reconfigurable 28-/37-GHz MMSE-Adaptive Hybrid-Beamforming Receiver for Carrier Aggregation and Multi-Standard MIMO Communication," *IEEE Journal of Solid-State Circuits*, vol. 54, pp. 1391–1406, May 2019.

[39] A. Perez, A. Rodriguez, A. Otero, D. G. Arjona, A. Jimenez-Peralo, M. A. Verdugo, and E. De La Torre, "Run-Time Reconfigurable MPSoC-Based On-Board Processor for Vision-Based Space Navigation," *IEEE Access*, vol. 8, pp. 59891–59905, 2020.

[40] B. Ghassemiparvin and N. Ghalichechian, "Reconfigurable antennas: quantifying payoffs for pattern, frequency, and polarisation reconfiguration," *IET Microwaves, Antennas Propagation*, vol. 14, no. 3, pp. 149–153, 2020.

[41] S. C. Ekpo, B. Adebisi, and A. Wells, "Regulated-Element Frost Beamformer for Vehicular Multimedia Sound Enhancement and Noise Reduction Applications," *IEEE Access*, vol. 5, pp. 27254–27262, 2017.

[42] R. K. Saha, "Millimeter-Wave Spectrum Utilization Improvement in Multi-Operator Networks: A Framework Using the Equal Likelihood Criterion," *IEEE Access*, vol. 9, pp. 72980–72999, 2021.

[43] I. Otung, *Communication engineering principles*. John Wiley & Sons, 2021.

[44] M. Lauridsen, P. Mogensen, and T. B. Sorensen, "Estimation of a 10 Gb/s 5G Receiver's Performance and Power Evolution Towards 2030," in *2015 IEEE 82nd Vehicular Technology Conference (VTC2015-Fall)*, pp. 1–5, Sept 2015.

[45] S. Rostami, K. Heiska, O. Puchko, K. Leppanen, and M. Valkama, "Robust Pre-Grant Signaling for Energy-Efficient 5G and beyond Mobile Devices," in *2018 IEEE International Conference on Communications (ICC)*, pp. 1–6, May 2018.

[46] S. Wu, Y. Wang, M. Al-Imari, and M. Nekovee, "Frequency and Quadrature Amplitude Modulation for 5G networks," in *2016 European Conference on Networks and Communications (EuCNC)*, pp. 1–5, June 2016.

[47] E. Ayanoglu, "5G Today: Modulation Technique Alternatives," in *2016 International Conference on Computing, Networking and Communications (ICNC)*, pp. 1–5, Feb 2016.

[48] H. Zhang, A. Wen, W. Zhang, W. Zhang, W. Zhai, and Z. Tu, "A Novel Spectral-Efficient Coherent Radio-Over-Fiber Link With Linear Digital-Phase Demodulation," *IEEE Photonics Journal*, vol. 12, pp. 1–8, Feb 2020.

[49] S. Gao, X. Cheng, and L. Yang, "Spatial Multiplexing With Limited RF Chains: Generalized Beamspace Modulation (GBM) for mmWave Massive MIMO," *IEEE Journal on Selected Areas in Communications*, vol. 37, pp. 2029–2039, Sep. 2019.

[50] H. S. Hussein, M. Elsayed, U. S. Mohamed, H. Esmaiel, and E. M. Mohamed, "Spectral Efficient Spatial Modulation Techniques," *IEEE Access*, vol. 7, pp. 1454–1469, 2019.

[51] T. Das, "Practical Considerations for Low Noise Amplifier Design," *Freescale Semiconductor*, 2013.

[52] S. Ekpo, R. Kharel, and M. Uko, "A Broadband LNA Design in Common-Source Configuration for Reconfigurable Multi-standards Multi-bands Communications," in *2018 ARMMS RF and Microwave Conference*, pp. 1–10, April 2018.

[53] F. Akbar, M. Atarodi, and S. Saeedi, "Design method for a Reconfigurable CMOS LNA with Input Tuning and Active Balun," *AEU-International Journal of Electronics and Communications*, vol. 69, no. 1, pp. 424–431, 2015.

[54] A. C. Ulusoy, M. Kaynak, T. Purtova, B. Tillack, and H. Schumacher, "A 60 to 77 GHz Switchable LNA in an RF-MEMS Embedded BiCMOS Technology," *IEEE Microwave and Wireless Components Letters*, vol. 22, pp. 430–432, Aug 2012.

[55] A. C. Ulusoy, M. Kaynak, T. Purtova, B. Tillack, and H. Schumacher, "24 to 79 GHz frequency Band Reconfigurable LNA," *Electronics Letters*, vol. 48, pp. 1598–1600, December 2012.

[56] M. D. Souza, A. Mariano, and T. Taris, "Reconfigurable Inductorless Wideband CMOS LNA for Wireless Communications," *IEEE Transactions on Circuits and Systems I: Regular Papers*, vol. 64, pp. 675–685, March 2017.

[57] A. R. A. Kumar, A. Dutta, and B. D. Sahoo, "A Low-Power Reconfigurable Narrowband/Wideband LNA for Cognitive Radio-Wireless Sensor Network," *IEEE Transactions on Very Large Scale Integration (VLSI) Systems*, vol. 28, pp. 212–223, Jan 2020.

[58] A. A. Nawaz, J. D. Albrecht, and A. Cagri Ulusoy, "A Ka/V Band-Switchable LNA With 2.8/3.4 dB Noise Figure," *IEEE Microwave and Wireless Components Letters*, vol. 29, pp. 662–664, Oct 2019.

[59] J. Heredia, M. Ribó, L. Pradell, S. T. Wipf, A. Göritz, M. Wietstruck, C. Wipf, and M. Kaynak, "A 125–143-GHz Frequency-Reconfigurable BiCMOS Compact LNA Using a Single RF-MEMS Switch," *IEEE Microwave and Wireless Components Letters*, vol. 29, pp. 339–341, May 2019.

[60] K. Kwon, S. Kim, and K. Y. Son, "A Hybrid Transformer-Based CMOS Duplexer With a Single-Ended Notch-Filtered LNA for Highly Integrated Tunable RF Front-Ends," *IEEE Microwave and Wireless Components Letters*, vol. 28, pp. 1032–1034, Nov 2018.

[61] R. Singh, G. Slovin, M. Xu, T. E. Schlesinger, J. A. Bain, and J. Paramesh, "A Reconfigurable Dual-Frequency Narrowband CMOS LNA Using Phase-Change RF Switches," *IEEE Transactions on Microwave Theory and Techniques*, vol. 65, pp. 4689–4702, Nov 2017.

[62] L. Boero, R. Bruschi, F. Davoli, M. Marchese, and F. Patrone, "Satellite Networking Integration in the 5G Ecosystem: Research Trends and Open Challenges," *IEEE Network*, vol. 32, pp. 9–15, September 2018.

[63] Y. Xu, G. Wang, S. Wei, E. Blasch, K. Pham, and G. Chen, "High-throughput, Cyber-Secure Multiuser Superposition Covert Avionics System," *IEEE Aerospace and Electronic Systems Magazine*, vol. 33, pp. 4–15, February 2018.

[64] L. Bai, L. Zhu, X. Zhang, W. Zhang, and Q. Yu, "Multi-Satellite Relay Transmission in 5G: Concepts, Techniques, and Challenges," *IEEE Network*, vol. 32, pp. 38–44, September 2018.

[65] J. Lin, "Synchronization Requirements for 5G: An Overview of Standards and Specifications for Cellular Networks," *IEEE Vehicular Technology Magazine*, vol. 13, pp. 91–99, Sept 2018.

[66] S. Cioni, R. D. Gaudenzi, O. D. R. Herrero, and N. Girault, "On the Satellite Role in the Era of 5G Massive Machine Type Communications," *IEEE Network*, vol. 32, pp. 54–61, September 2018.

[67] S. C. Ekpo and D. George, "Impact of Noise Figure on a Satellite Link Performance," *IEEE Communications Letters*, vol. 15, pp. 977–979, September 2011.

[68] A. R. A. Kumar, A. Dutta, and B. D. Sahoo, "A low-power reconfigurable narrowband/wideband lna for cognitive radio-wireless sensor network," *IEEE Transactions on Very Large Scale Integration (VLSI) Systems*, vol. 28, no. 1, pp. 212–223, 2020.

[69] K. Kaneko, H. Nishiyama, N. Kato, A. Miura, and M. Toyoshima, "Construction of a Flexibility Analysis Model for Flexible High-Throughput Satellite Communication Systems With a Digital Channelizer," *IEEE Transactions on Vehicular Technology*, vol. 67, pp. 2097–2107, March 2018.

[70] H. Fenech, S. Amos, A. Tomatis, and V. Soumpholphakdy, "High throughput satellite systems: An analytical approach," *IEEE Transactions on Aerospace and Electronic Systems*, vol. 51, pp. 192–202, January 2015.

[71] S. Bhaumik and D. Kettle, "Broadband X-band low noise amplifier based on 70 nm GaAs metamorphic high electron mobility transistor technology

for deep space and satellite communication networks and oscillation issues," *IET Microwaves, Antennas Propagation*, vol. 4, pp. 1208–1215, Sep. 2010.

[72] M. R. Nikbakhsh, E. Abiri, H. Ghasemian, and M. R. Salehi, "Two-stage current-reused variable-gain low-noise amplifier for X-band receivers in 65 nm complementary metal oxide semiconductor technology," *IET Circuits, Devices Systems*, vol. 12, no. 5, pp. 630–637, 2018.

[73] M. Davulcu, C. Caliskan, I. Kalyoncu, and Y. Gurbuz, "An X-Band SiGe BiCMOS Triple-Cascode LNA With Boosted Gain and P1dB," *IEEE Trans. Circuits Syst., II, Exp. Briefs*, vol. 65, pp. 994–998, Aug 2018.

[74] H. Nam, V.-V. Nguyen, V.-S. Trinh, J.-M. Song, B.-H. Lee, and J.-D. Park, "A Full X-Band Phased-Array Transmit/Receive Module Chip in 65-nm CMOS Technology," *IEEE Access*, vol. 8, pp. 76182–76192, 2020.

[75] A. çağlar and M. B. Yelten, "A 180-nm X-Band Cryogenic CMOS LNA," *IEEE Microwave and Wireless Components Letters*, vol. 30, no. 4, pp. 395–398, 2020.

[76] B. A. Abelan, M. Seelmann-Eggebert, D. Bruch, A. Leuther, H. Massler, B. Baldischweiler, M. Schlechtweg, J. D. Gallego-Puyol, I. Lopez-Fernandez, C. Diez-Gonzalez, I. Malo-Gomez, E. Villa, and E. Artal, "4-12 and 25-34 GHz Cryogenic mHEMT MMIC Low-Noise Amplifiers," *IEEE Transactions on Microwave Theory and Techniques*, vol. 60, pp. 4080–4088, Dec 2012.

[77] E. Cha, N. Wadefalk, P. Nilsson, J. Schleeh, G. Moschetti, A. Pourkabirian, S. Tuzi, and J. Grahn, "0.3-14 and 16-28 GHz Wide-Bandwidth Cryogenic MMIC Low-Noise Amplifiers," *IEEE Transactions on Microwave Theory and Techniques*, vol. 66, pp. 4860–4869, Nov 2018.

[78] T. R. LaRocca, K. Thai, R. Snyder, R. Jai, D. Kultran, O. Fordham, B. Y.-C. Wu, Y. Yang, M. K. Watanabe, P. Rodgers, D. Lam, E. B.

Nakamura, N. Daftari, and F. Kamgar, "Secure Satellite Communication Digital IF CMOS ¡inline-formula¿ ¡tex-math notation="LaTeX"¿Q ¡/tex-math¿¡/inline-formula¿-Band Transmitter and ¡inline-formula¿ ¡tex-math notation="LaTeX"¿K ¡/tex-math¿¡/inline-formula¿-Band Receiver," *IEEE Journal of Solid-State Circuits*, vol. 54, no. 5, pp. 1329–1338, 2019.

[79] F. Tabarani, L. Boccia, T. Purtova, A. Shamsafar, H. Schumacher, and G. Amendola, "0.25-¡inline-formula¿ ¡tex-math notation="LaTeX"¿μm ¡/tex-math¿¡/inline-formula¿ BiCMOS System-on-Chip for K-/Ka-Band Satellite Communication Transmit–Receive Active Phased Arrays," *IEEE Transactions on Microwave Theory and Techniques*, vol. 66, no. 5, pp. 2325–2339, 2018.

[80] J. Pang, Z. Li, R. Kubozoe, X. Luo, R. Wu, Y. Wang, D. You, A. A. Fadila, R. Saengchan, T. Nakamura, J. Alvin, D. Matsumoto, B. Liu, A. T. Narayanan, J. Qiu, H. Liu, Z. Sun, H. Huang, K. K. Tokgoz, K. Motoi, N. Oshima, S. Hori, K. Kunihiro, T. Kaneko, A. Shirane, and K. Okada, "A 28-GHz CMOS Phased-Array Beamformer Utilizing Neutralized Bi-Directional Technique Supporting Dual-Polarized MIMO for 5G NR," *IEEE Journal of Solid-State Circuits*, vol. 55, no. 9, pp. 2371–2386, 2020.

[81] H.-T. Kim, B.-S. Park, S.-S. Song, T.-S. Moon, S.-H. Kim, J.-M. Kim, J.-Y. Chang, and Y.-C. Ho, "A 28-GHz CMOS Direct Conversion Transceiver With Packaged ¡inline-formula¿ ¡tex-math notation="LaTeX"¿2×4 ¡/tex-math¿¡/inline-formula¿ Antenna Array for 5G Cellular System," *IEEE Journal of Solid-State Circuits*, vol. 53, no. 5, pp. 1245–1259, 2018.

[82] B. Sadhu, Y. Tousi, J. Hallin, S. Sahl, S. K. Reynolds, O. Renström, K. Sjogren, O. Haapalahti, N. Mazor, B. Bokinge, G. Weibull, H. Bengtsson, A. Carlinger, E. Westesson, J.-E. Thillberg, L. Rexberg, M. Yeck, X. Gu, M. Ferriss, D. Liu, D. Friedman, and A. Valdes-Garcia, "A 28-GHz 32-

Element TRX Phased-Array IC With Concurrent Dual-Polarized Operation and Orthogonal Phase and Gain Control for 5G Communications," *IEEE Journal of Solid-State Circuits*, vol. 52, no. 12, pp. 3373–3391, 2017.

[83] Y. Wang, D. You, X. Fu, T. Nakamura, A. A. Fadila, T. Someya, A. Kawaguchi, J. Qiu, J. Pang, K. Yanagisawa, B. Liu, Y. Zhang, H. Zhang, R. Wu, S. Masaki, D. Yamazaki, A. Shirane, and K. Okada, "A ¡italic¿Ka¡/italic¿-Band SATCOM Transceiver in 65-nm CMOS With High-Linearity TX and Dual-Channel Wide-Dynamic-Range RX for Terrestrial Terminal," *IEEE Journal of Solid-State Circuits*, vol. 57, no. 2, pp. 356–370, 2022.

[84] H. Uchida, S. Takatsu, K. Nakahara, T. Katoh, Y. Itoh, R. Imai, M. Yamamoto, and N. Kadowaki, "Ka-band multistage mmic low-noise amplifier using source inductors with different values for each stage," *IEEE Microwave and Guided Wave Letters*, vol. 9, pp. 71–72, Feb 1999.

[85] G. Nikandish, A. Yousefi, and M. Kalantari, "A broadband multistage lna with bandwidth and linearity enhancement," *IEEE Microwave and Wireless Components Letters*, vol. 26, pp. 834–836, Oct 2016.

[86] Q. Ma, D. M. W. Leenaerts, and P. G. M. Baltus, "Silicon-Based True-Time-Delay Phased-Array Front-Ends at Ka-Band," *IEEE Transactions on Microwave Theory and Techniques*, vol. 63, pp. 2942–2952, Sep. 2015.

[87] M. Elkholy, S. Shakib, J. Dunworth, V. Aparin, and K. Entesari, "A Wideband Variable Gain LNA With High OIP3 for 5G Using 40-nm Bulk CMOS," *IEEE Microwave and Wireless Components Letters*, vol. 28, pp. 64–66, Jan 2018.

[88] A. Kumari and D. Bhatt, "Advanced system analysis and survey on the gps receiver front end," *IEEE Access*, vol. 10, pp. 24611–24626, 2022.

[89] Y. Huo, X. Dong, W. Xu, and M. Yuen, "Enabling Multi-Functional 5G and Beyond User Equipment: A Survey and Tutorial," *IEEE Access*, vol. 7, pp. 116975–117008, 2019.

[90] S. C. Ekpo, "Thermal Subsystem Operational Times Analysis for Ubiquitous Small Satellites Relay in LEO," *International Review of Aerospace Engineering (IREASE)*, vol. 11, p. 48, 04 2018.